FORSCHUNGSZENTRUM ROSSENDORF

Torsten Müller

Ion Beam Synthesis of Ge Nanowires

revised version, Dresden 18.12.2000

Ion Beam Synthesis of Ge Nanowires

Diplomarbeit
zur Erlangung des akademischen Grades
Diplom - Physiker
vorgelegt von

Torsten Müller

geboren am 1.3.1976 in Dresden

Institut für Ionenstrahlphysik und Materialforschung,
Forschungszentrum Rossendorf
Fachrichtung Physik
Fakultät Mathematik und Naturwissenschaften
der Technischen Universität Dresden
2000

1. Gutachter (referee): Prof. Dr. Wolfhard Möller
Technische Universität Dresden

2. Gutachter (referee): Prof. Harry A. Atwater, PhD
California Institute of Technology

Datum des Einreichens der Arbeit (submitted) : 30.11.2000

Abstract

The formation of Ge nanowires in V-grooves has been studied experimentally as well as theoretically. As substrate oxide covered Si V-grooves were used formed by anisotropic etching of (001)Si wafers and subsequent oxidation of their surface. Implantation of 1×10^{17} $\mathrm{Ge^{+}cm^{-2}}$ at 70 keV was carried out into the oxide layer covering the V-grooves. Ion irradiation induces shape changes of the V-grooves, which are captured in a novel continuum model of surface evolution. It describes theoretically the effects of sputtering, redeposition of sputtered atoms, and swelling. Thereby, the time evolution of the target surface is determined by a nonlinear integro-differential equation, which was solved numerically for the V-groove geometry. A very good agreement is achieved for the predicted surface shape and the shape observed in XTEM images. Surprisingly, the model predicts material (Si, O, Ge) transport into the V-groove bottom which also suggests an Ge accumulation there proven by STEM-EDX investigations. In this Ge rich bottom region, subsequent annealing in N_2 atmosphere results in the formation of a nanowire by coalescence of Ge precipitates shown by XTEM images. The process of phase separation during the nanowire growth was studied by means of kinetic 3D lattice Monte-Carlo simulations. These simulations also indicate the disintegration of continuous wires into droplets mediated by thermal fluctuations. Energy considerations have identified a fragmentation threshold and a lower boundary for the droplet radii which were confirmed by the Monte Carlo simulation. The here given results indicate the possibility of achieving nanowires being several nanometers wide by further growth optimizations as well as chains of equally spaced clusters with nearly uniform diameter.

Zusammenfassung

In dieser Arbeit wird die Synthese von Ge Nanodrähten in V-Gräben sowohl experimentell als auch theoretisch untersucht. Als Substrat dienen dabei Oxid bedeckte Si V-Gräben die durch anisotropes Ätzen von (001)Si Wafern und anschließender Oxidation hergestellt werden. In diese Oxidschicht werden Ge Ionen mit 70 keV bis zu einer Dosis von 1×10^{17} $Ge^{+}cm^{-2}$ implantiert. Die durch die Implantation hervorgerufenen Veränderungen der Waferoberfläche werden in einem hier neu entwickelten Modell beschrieben. Es erfaßt die Zerstäubung und die Redeposition von zerstäubten Atomen in einer allgemeinen Kontinuumsbeschreibung. Die zeitliche Entwicklung der Oberfläche wird dabei durch eine Bewegungsgleichung in Form einer Integro-Differentialgleichung beschrieben. Der Vergleich der numerischen Lösung des Modells für den V-Graben mit XTEM Aufnahmen implantierter Proben liefert eine sehr gute Übereinstimmung der Oberflächen. Das Modell zeigt, daß zerstäubtes Material (Si, 0, Ge) in der Spitze des V-Grabens deponiert wird und dort zu einer unerwarteten Anreicherung von Ge führt, was STEM-EDX Untersuchungen bestätigen. Die sich der Implantation anschließende Temperung führt zu einer Drahtbildung in der Spitze des V-Grabens während sich in den Seitenwänden nur isolierte Nanocluster bilden. Der Prozeß der Phasenseparation während des Temperns wird durch kinetische Monte Carlo Simulationen beschrieben. Die Simulationen zeigen außerdem eine Tendenz des Zerfalls bereits gebildeter Nanodrähte auf, da diese nur metastabil sind und durch thermische Fluktuationen in isolierte Cluster zerfallen können. Energetische Betrachtungen liefern sowohl eine Zerfallsschwelle als auch eine Untergrenze für die Größe der durch den Zerfall erhaltenen Cluster. Die Ergebnisse der Monte Carlo Simulationen stimmen damit überein. Die hier gewonnenen Resultate bestätigen den vorgeschlagenen Weg zur Synthese von Ge Nanodrähten. Mit weiteren Optimierungen der Wachstumsparameter sollte die Herstellung von Nanodrähten mit einigen Nanometern Durchmesser möglich sein. Zusätzlich erlaubt der kontrollierte Zerfall von Nanodrähten die Synthese von Cluster-Ketten.

Contents

Abbreviations

Often repeated expressions or lengthly technical description will be abbreviated. For the clearness of this work it has been tried to suppress acronyms wherever this is possible.

AFM	Atomic Force Microscopy
BH	Bradley-Harper
CMOS	Complementary Metal Oxide Semiconductor
CNT	Classical Nucleation Theory
dpa	displacements per atom
DOS	Density of states
EDX	Energy Dispersive X-Ray Analysis
fcc	face-centered cubic
GT	Gibbs-Thomson
IBS	ion beam synthesis
LSW	Lifschitz, Slyozov, Wagner
KLMC	Kinetic Lattice Monte Carlo
KPZ	Kardar-Parisi-Zhang
KS	Kuramoto-Sivashinsky
MC	Monte Carlo
MCS	Monte Carlo steps
NRA	Nuclear Reaction Analysis
QD	Quantum Dot (localized electrons)
OMCVD	Organometallic Chemical Vapor Deposition
QW	Quantum Well (2D electron gas)
QWR	Quantum Wire (1D electron gas)
SBE	surface binding energy
STM	Scanning Tunneling Microscope
TEM	Transmission Electron Microscopy
XTEM	Cross Sectional Transmission Electron Microscopy

Chapter 1

Introduction

1.1 Motivation - Ion Beam Synthesis

Low dimensional semiconductor structures have attracted much attention in the past. Electrons confined in one or more dimensions bestows traditional semiconductors materials new possibilities and give rise to concentrated energy states in quantum wells (QWs), quantum wires (QWRs), and quantum dots (QDs). Moreover, the carrier density of states (DOS) near the band edge changes with reduced dimensionality from a square root shape for the bulk semiconductors over a constant DOS for QWs to a reciprocal shape for QWRs. The DOS for QDs is singular, the electrons are localized within the dots on discrete, sharp energy levels. For an introduction to low dimensional semiconductor physics refer to [Dav98].

A huge variety of new physical phenomena have been discovered since the first structures have been synthesized, e.g. fractional quantum hall effect and conductance quantum. Additional possibilities for novel application have risen, e.g. low threshold QWR lasers, non-volatile memories, and single electron transistors, which may further revolutionize semiconductor physics.

Nanostructures open new possibilities even for traditional fields as the classical electrodynamics. As shown recently, electromagnetic waves can be guided along regular chains of nanoclusters embedded in dielectric material and can be bound around edges below the classical diffraction limit [BHA00].

However, the variety of promising applications is faced by the limited amount of tools for the precise synthesis of the desired structures. In principle it should be possible to arrange single atoms (Richard P. Feynman “There’s plenty of room at the bottom” [Fey60]):

> The principles of physics, as far as I can see, do not speak against the possibility to maneuvering things atom by atom. It’s not an attempt to violate any laws; it is something, in principle, that can be done; but, in practice, it has not been done because we are to big.

We’ve got smaller in the last years. Single atoms can be maneuvered now by scanning probe techniques [Avo93]. Nevertheless, this is no suitable method for large-scale mass production. Alternatively, several self-organization phenomena arising can be understood as a chance for the indirect synthesis of nanostructures. The amount of published contributions on these topics is currently exploding and the main task despite the pure understanding is to tame self-organization. The questions is, how

can these sensible processes be integrated into regular semiconductor setups using standard CMOS technology.
Beside other techniques ion beam synthesis (IBS) is one method facilitating self-organization phenomena. It uses ion implantation[1] at higher fluences as a clean and well controlled tool for the synthesis of second phase nanostructures in a range of different host matrices. It naturally extends the almost classical application of ion implantation from simple semiconductor doping to the fabrication of super-saturated solid solutions of implanted impurity atoms. These far-from-equilibrium states relaxes then by phase separation at elevated temperatures. Nearly spherical precipitates are formed reported as nanocluster, nanocrystals, or QDs [WBW+97].
IBS can be even taken a step further. Using highest implantation fluences second phase domains start to coalesce and form extended structures. E.g. continuous buried layers are achieved by ion implantation into flat targets. On the other side the target don't have to be flat and unstructured. For IBS, much more possibilities arise from implantation into pre-structured targets.
Such an approach will be presented in this work for the synthesis of Ge nanowires embedded in SiO_2.

1.2 The V-Groove Principle - Outline

Ge nanowires are synthesized by high fluence Ge^+ implantation into oxide covered Si V-grooves, for the scheme of synthesis see figure 1.1. These grooves have been formed by anisotropic etching of (001)Si wafers and subsequent oxidation. Then the high fluence Ge^+ implantation into the oxidized V-grooves leads to a tailored profile of Ge atoms embedded in the oxide layer which is the key for the Ge nanowire synthesis.
Assume the chosen ion fluence is just sufficient to achieve a continuous buried Ge layer at plane surfaces. In the slanted V-groove sidewalls instead the number of ions per unit area is lower than at the plane wafer surface. This reduced Ge concentration will be too low to allow an efficient coalescence of precipitates, which is the crucial process for the layer formation. However, at the V-groove bottom the concentration is expected to be high enough to allow coalescence, since the bottom can be considered as a small plane area. Consequently, thin Ge nanowires will form in the V-groove bottom by phase separation from the initial Ge supersaturation achieved by ion implantation. Moreover, even at the edges of the V-groove continuous wires could be possibly formed, which then connect the nanowire in the V-groove bottom with the buried Ge layer at the plane wafer surfaces. As shown in figure 1.1 this could be used for electrical contact pads. However, the main focus in this work will be laid on the synthesis of the nanowires buried in the V-groove bottom, not on their electrical properties.
This work presents experimental as well as theoretical studies concerning the nanowire growth in in oxidized Si V-grooves. The different states of sample preparation, implantation and subsequent annealing have been documented by Cross Sectional Transmission Electron Microscopy (XTEM) images (chapter 2).

---

[1] See [NMH96] for an introduction to ion-solid interactions.

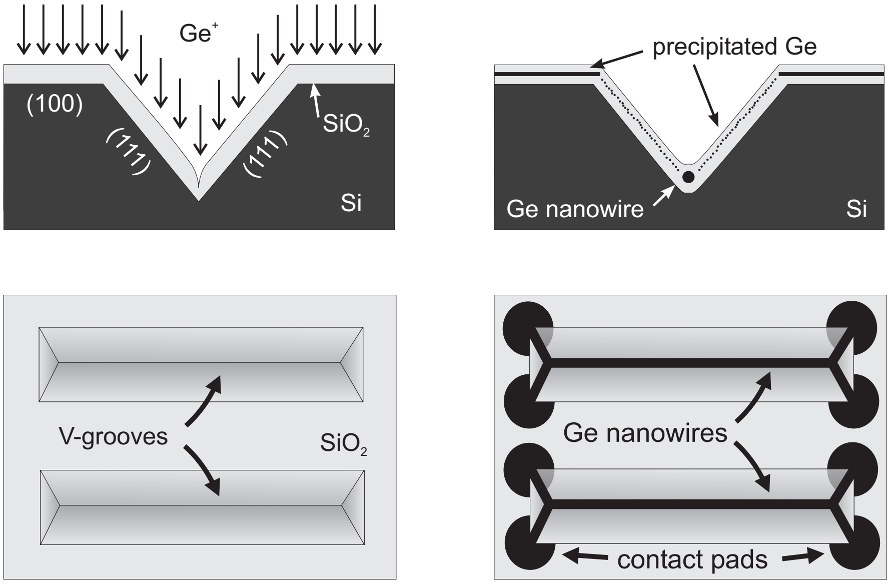

(a) Ge$^+$ implantation

(b) after annealing

Figure 1.1: Scheme of ion beam synthesis of buried Ge nanowires in the bottom of oxidized silicon V-grooves. (a) Ge$^+$ will be implanted at high fluence into SiO$_2$ covered silicon V-grooves and (b) the sample will be subsequently annealed in an inert ambient. The nanowire forms by precipitation and coalescence in the V-groove bottom, while at the sidewalls only Ge nanoclusters are formed.

The surface shape changes taking place during ion irradiation are theoretically captured in a continuum framework (chapter 3). Therefore a novel model including the effects of sputtering, swelling and redeposition of sputtered atoms has been developed [MHS00]. The presented treatment differs thereby substantially from other theories of sputter-induced surface evolutions [BH88, KPZ86]. By considering high inclination angles in the specific V-groove geometry, small gradient expansions can not be applied. The derived formulation will be applied to the V-grooves under ion irradiation and a direct comparison to XTEM images will be given, which show a very good agreement between theory and experiment. Sputtering and redeposition lead to an unexpected material transport into the V-groove bottom. An effective Ge accumulation there is predicted and is proven by Scanning Transmission Electron Microscopy - Energy Dispersive X-Ray Analysis (STEM-EDX).

Complementary to the experiments the growth of the nanowire is studied theoretically by means of kinetic 3D lattice Monte Carlo (KLMC) simulations (chapter 4). The simulations provide a more solid understanding of phase separation phenomena since they could serves as an unique tool to check ideas in an clean environment without any conflicting side effects. Applied to the nanowire growth additional knowledge about influencing parameters is gained without immense experimental effort.

Moreover, the stability of continuous nanowires is discussed in chapter 5. In general wires are energetically metastable and can be fragmented by thermal fluctuations into isolated droplets. Energy considerations have lead to the derivation of a fragmentation threshold. Further the direct fragmentation under subsequent ion irradiation is predicted. On the other hand, a lower bound for the radii of droplets produced by the fragmentation has been identified. Additional KLMC simulations confirm the spontaneous wire disintegration for very thin wires and the observed droplets radii agree nicely with the predicted one.

1.3 Other Approaches to a Nanowire Synthesis

Thin wires are no absolutely new subject in physics. Nano- or quantum wires have been produced by a number of different techniques. The most prominent examples are carbon nanotubes first synthesized by the Smalley group [HZO+87]. Carbon nanotubes obey several millimeters length and diameters in the order of few nanometer. They are fabricated by laser ablation of graphite and are extracted from the produced sooth. Dependent on their chirality the nanotubes are either metallic or semiconducting. Electrical measurements have been performed on single tubes by using the Scanning Tunneling Microscope (STM).

This principle of wire synthesis have later been extended to other material than carbon. Similar to carbon nanotubes Ge nanowires were fabricated by laser ablation [ZTW+00] but obeys with 100 nm a much larger diameter. Silicon nanowires were formed form a heated Si-SiO_2 mix on iron-patterned Si substrates [GSRW00, GDC+00]. On the other hand carbon nanotubes can be filled by several conducting materials [THS+98]. Nevertheless, these free standing wires can not be easily integrated in electronic devices.

A more direct approach to silicon nanowires is the synthesis by standard photolithographic techniques, see e.g. [TNA+98]. The wires are etched from silicon wafers but obey a much to large diameter, which can be partially overcome by electron beam lithography [NNK+95]. Diameter of 50 nm are possible which are further shrunk by thermal oxidation [KBA99] due to a self limiting effect. The self-limiting oxidation has also been used with photolithographic patterned substrates [LSW+95]. However, these attempt are tightly bound to very sensible processes needed for the synthesis as the limited oxidation. Additionally, e-beam lithography is still not commonly applied in the semiconductor industry.

To achieve a QWRs it is not always needed to fabricate electrically isolated nanowires. It is just sufficient to have a quantum well which is bent or has a linear region with higher QW thickness. Due to the lowered energy states in such regions electrons are confined two dimensionally at low temperatures.

One of these methods is the cleaved edge overgrowth. QW are cleaved and subsequently overgrown at their edge by a second QW. The resulting T-shape structure of QW's provides indeed a QWR at the intersection of both QWs. This concept is usually realized by GaAs/AlGaAs heterostructures. However, a bent QW can also be achieved by organometallic chemical vapor deposition (OMCVD) of AlGaAs on V-grooved GaAs substrates [GRBK95, BRGK97, KLK+97]. The deposited layer is considerably thicker at the V-groove bottom, thus a QWR as lowest energy state is formed there. Also other substrate systems are possible, e.g. InGaAs QWR's on

InP V-grooves [SBW$^+$99] or SiGe QWR's on Si V-grooves [HDL$^+$95, HVDL95]. One major advantage of this method is that the QWR's can be easily stacked as needed for high output laser devices. Unfortunately, these approaches differ considerably in used techniques and substrate materials from the commonly used CMOS technology. Another set of methods facilitates self-organization phenomena on surfaces. Various "self-assembly" techniques, in which structures form spontaneously under kinetic or thermodynamic control, have been used to grow wire like structure directly on a semiconductor surface. The methods include the decoration of step edges [YKF$^+$97, RSD$^+$00] and submonolayer epitaxial deposition of elements with a large anisotropic lattice mismatch [COMR$^+$00].

In view of IBS, the most interesting method have been recently demonstrated by O^+ implantation into Si V-grooves [ISF98, ISF99]. A discontinuous Si layer is formed which is isolated by SiO_2 from the bulk material. This layer consists of the QWR at the V-groove bottom and two (111) crystal slabs in the sidewalls. However these methods appears to rely strongly on sensitive self-organization phenomena during OSTWALD ripening, which allows no precise process control.

Therefore, the more direct way of IBS of nanowires using V-grooves is proposed here.

Chapter 2

Experimental

Silicon is the semiconductor material with the highest technological impact. Together with its high availability it provides a high-quality oxide. Thermal silicon oxides combine enormous thermal stability with a low amount of defect associated states even at the SiO_2/Si interface. These properties are also advantageous for a nanowire synthesis based on silicon technology. In the present case the wire will be formed in SiO_2 by ion implantation into structured 3 ” (001)Si wafers.

2.1 V-groove Preparation

The Si wafers were cleaned in $H_2O_2 + H_2SO_4$ at elevated temperature and subsequently oxidized in dry O_2 at 1000 °C resulting in a 100 nm thick SiO_2 layer. Further, this layer was photolithographically patterned opening rectangular windows of $2 \dots 12$ µm × 5 mm size, which are aligned to the [110] direction of the (001)Si wafer. The spacing between these windows was $2 \dots 6$ µm. In these rectangles the SiO_2 was removed during an etching step with buffered HF solution. The rectangular openings define the position of the V-grooves, which were prepared by subsequent etching, which is carried out in 30% KOH at 80 °C. The used etch solution is highly selective against Si/SiO_2 with an etch ratio of 380 : 1 at the given temperature and concentration. Moreover, the etch velocity depends on the orientation of the Si surface. (100) surfaces are etched faster than the more stable (111)Si surfaces, the etch ratio between both is 34.5. This leads to an initially fast etching of the opened Si rectangles, while (111) facets starts to form at the edges of the V-groove. Since the evolving (111) facets are much more stable than the (001) surfaces, the etching stops if the (111)Si V-groove sidewalls touch each other at the bottom. This self-adjusting process results in atomically smooth (111) sidewalls with an angle of 54.7 ° to the plane wafer surface. Finally, the remaining protective oxide is removed by buffered HF to get free, unoxidized Si V-grooves, as shown by the

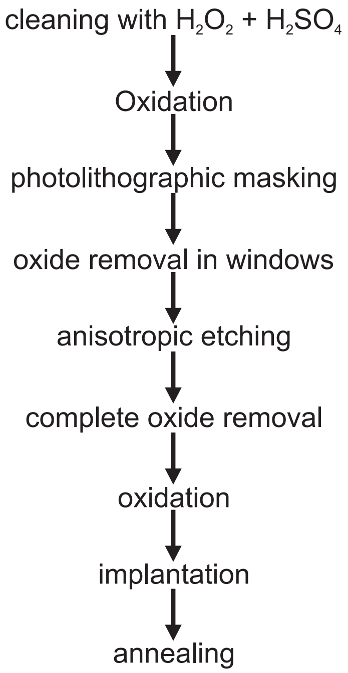

Figure 2.1: Experimental procedure for the synthesis of nanowires

XTEM image in figure 2.2.

However, to assure a high accuracy of the orientation of the lithographic mask to the [110] direction of the Si wafer, special arrangement procedures have to be used. Otherwise, the mismatch between mask and [110] surface orientation leads to periodical interruptions of the V-groove by a slight horizontal displacement. In this staircase-like structure the spacing between the kinks is expected to be proportional to the cotangent of the angle of misalignment. The better the alignment is, the longer is the uninterrupted V-groove, which becomes very important if long completely continuous nanowires are of interest. Especially, possible electronic devices would suffer extremely from mask misalignment. In the worst case current transport along the wire is interrupted. By chance, these kinks can also be seen in the XTEM pictures (figure 2.3(b)) if the cross section goes directly through the kink.

After etching, the Si V-grooves were oxidized in dry O_2 at 1000 °C covering the (001)Si and (111)Si surfaces with a 200 nm and (220 nm) thick oxide layer, respectively. The faster oxidation of (111) surfaces also explains partially the sharp depression of the SiO_2 surface at the V-groove bottom, shown in figure 2.3(a). It will induce a swelling of the oxide layer by a factor of 2.2 which is stronger at the V-groove sidewalls. Thus, the swelling constricts the V-groove in all points but the very bottom of the V-groove. Additionally, the oxidation is curvature dependent. The oxidation speed is decreased for the concave Si surface at the V-groove bottom compared to a flat interface, which enhances the tendency towards a sharp depression.

2.2 Ion Implantation and Thermal Treatment

Following the aim to synthesize semiconducting nanowires with standard CMOS compatible technologies silicon should be implanted into the SiO_2 covered Si V-grooves. Instead Germanium was used here, since it provides similar electronic properties at a higher atomic mass. But most important, nanoclusters and nanowires containing Ge provide much better Z-contrast in TEM images, Si would be almost undistinguishable to SiO_2.

The Ge^+ implantation was carried out using the Rossendorf 500 keV high voltage implanter with 70 keV energy, which gives a projected ion range in the order of 50 nm. At this comparably low energy the risk of interactions of the Ge during subsequent annealing with the Si/SiO_2 interface is small, since the SiO_2 thickness is large compared to the projected range. The implantation fluence was chosen to be 1×10^{17} cm^{-2}, which should imply a Ge peak concentration of 30 % near the percolation threshold.

After implantation, the samples were cleaned and subsequently annealed in N_2 ambient (purity 5.0) at 950 °C for 10 minutes. Different annealing times and temperatures have been tried, but the above stated parameters seems to be the best ones tested till now. Additionally, the standard handling procedure of the furnace was altered. Usually, the furnace is heated up to the annealing temperature and the sample is then transferred with a rod into the hot furnace. Thereby, the hot annealing ambient mixes with the room atmosphere and introduces oxygen and moisture into the furnace. This could lead to an oxidation of the small amount of the implanted

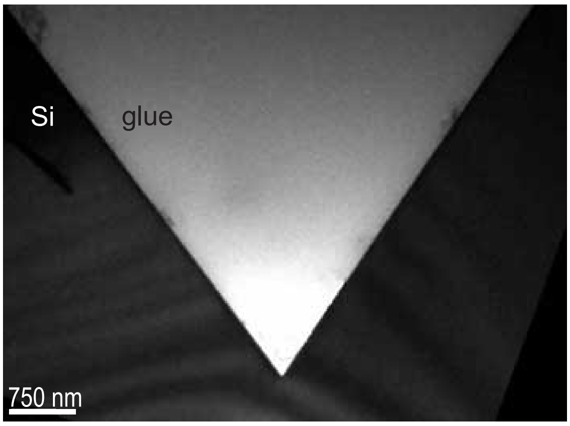

Figure 2.2: XTEM image of a Si V-groove prepared by anisotropic etching with KOH. The V-groove sidewalls are (111)Si facets and include an angle of 70.5 °.

Ge (see also next section). To omit the oxidation, the samples were transferred into the cold furnace and heated up under N_2 atmosphere. As the sample reaches the critical temperature for the oxidation introduced oxygen and moisture has already been purged.

2.3 TEM Studies

Most of the analytical work has been performed with the TEM. The aimed size of the nanowire is to small for any other technique except the TEM and the atomic force microscope (AFM)[1]. However, the nanowire is buried in SiO_2 and is therefore not easily accessible by surface imaging techniques like the AFM.
A Phillips CM 300 has been used to obtain the TEM images and the 2D STEM-EDX mapping of Ge. Cross section specimen for the XTEM were prepared by the standard technique. Samples (4×5 mm) were glued (M-Bond) face-to-face together and cross-sections were sliced. These pieces were ground, polished on both sides and dimpled by a dimple-grinder. Finally, the sample was further thinned by an Ar ion mill under a small angle till a small hole appeared in the middle of the sample. Around this region the sample was thin enough to allow electrons to transmit.
XTEM images were taken from different stages of preparation. Shown in figure 2.2 is an as-etched sample with sharp, precise (111) V-groove sidewalls. Images of as-oxidized V-grooves are shown in figure 2.3. The faster oxidation speed for the (111)Si surface compared to the (001)Si surface has lead to to a stronger swelling of the V-groove sidewalls. The result was a sharp surface depression, as visible in figure 2.3(a).
A cross-section of an as-implanted sample is shown in figure 2.4. Here, the sharp surface depression has vanished during the implantation. Material was eroded from the SiO_2 surfaces of the V-groove sidewalls and, surprisingly, has been effectively

---

[1] In principle a nanowire of more than 30 nm diameter can be also imaged by Scanning Electron Microscopy (SEM) but surrounding nanocluster of less than 10 nm can not.

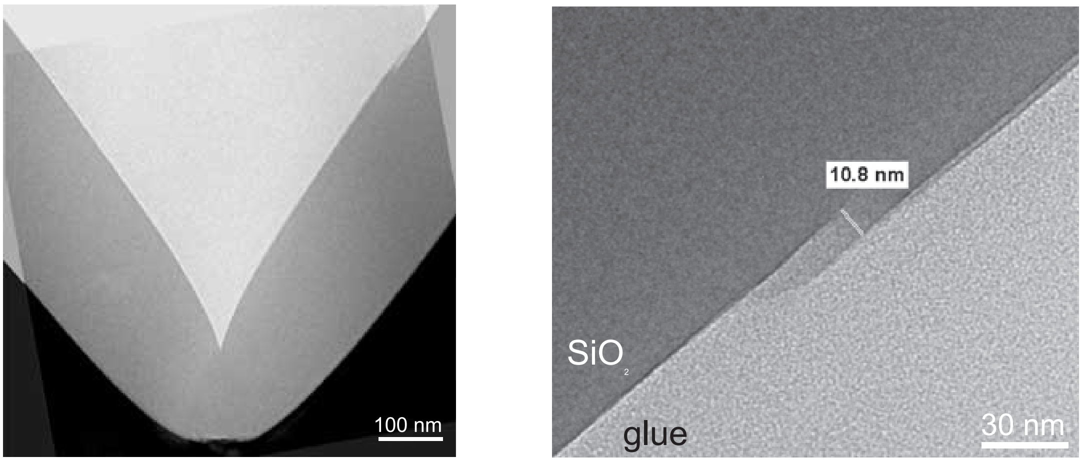

(a) bottom of an as-oxidized V-groove

(b) cross-section through a kink

Figure 2.3: XTEM images of an as-oxidized V-groove. Shown are (a) the V-groove bottom with the sharp surface depression and (b) a displacement of the SiO_2 surface caused by a kink in the V-groove. This displacement of the V-groove results from a slight misalignment of the lithographic mask to the [110] direction of the Si wafer.

transported into the V-groove bottom. Since these processes are essential for the nanowire growth they will by addressed in detail in chapter 3. Even more, during the erosion implanted Ge was redistributed and accumulated at the V-groove bottom. This is qualitatively explained in chapter 3.5 and experimentally proven by a 2D Ge STEM-EDX mapping of a cross-section of an as-implanted sample, shown in figure 2.5. Due to a slight wedge in the specimen, the concentration profile is asymmetric with respect to the center of the V-groove. The left side is thicker than the right one resulting in an increased X-ray yield there. Both, the Ge concentration ($\sim 30\%$) and the total amount of Ge are much higher in the V-groove bottom than in the sidewalls. The total amount of Ge is estimated from the projection of the concentration profile onto the horizontal axis, which is shown as a solid curve in figure 2.5. It is absolutely necessary to gain a solid understanding of these redistributions during the Ge^+ irradiation to control the nanowire growth.
Finally, cross-sections of an annealed sample are shown in figure 2.6. Ge clusters buried in the SiO_2 are present in the V-groove bottom and the sidewalls. Thereby, the dark dot in the bottom is expected to be a cross-section of a nanowire with 35 nm diameter. Several XTEM images have shown always the large black dot with identical diameter in the V-groove bottom, which is at least a strong indication for a continuous nanowire.
Additionally, the oxide region in figure 2.6 close to the surface (first 20 nm) appears brighter, which could have been caused by Ge oxidation during the annealing. Due to the influence of an oxidant Ge can react to GeO_x, which has a lower z-contrast in the TEM image. Possible oxidant sources are

atmospheric humidity: Ion implantation destroys the well formed SiO_2 network

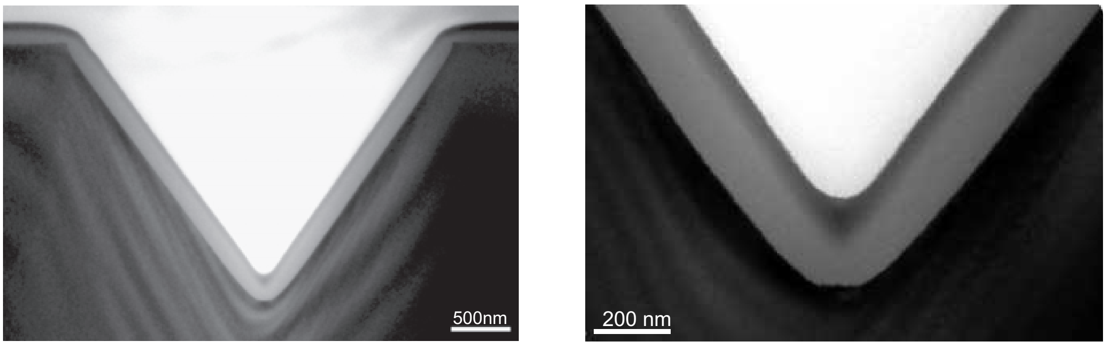

(a) overview of an as-implanted V-groove (b) bottom of an as-implanted V-groove

Figure 2.4: XTEM images of an as-implanted V-groove. Shown are (a) an overview of the V-groove and (b) the bottom region. The samples were implanted with 1×10^{17} $Ge^{+}cm^{-2}$ at 70 keV. An estimation of the Ge distribution is given by the dark shadow visible close to the SiO_2 surface.

leaving many dangling bonds. At low ion energy even the surface near region is heavily damaged. Consequently, the surface is highly reactive after the implantation and instantaneously captures moisture from the air. An excess of hydrogen has been proven by nuclear resonance analysis with MeV N^{+} ions [SG00] indicating the presence of moisture in the damaged oxide.

wet cleaning: The content of moisture in the SiO_2 is further increased by a wet cleaning step after ion implantation. Although, it seems to play only a minor role. Most of the free dangling bonds have already been saturated by the air humidity. Thus, the amount of hydrogen in the oxide layer is only slightly increased [SG00].

furnace handling: The furnace is usually run with inert gas excluding oxidants from the room air. Nevertheless, during the sample transfer the furnace is opened and the samples are inserted with a rod into hot zone. Together with the sample room air enters the furnace and incorporates oxidants. Although the furnace is steadily purged by nitrogen the oxidant could still have enough time to react in the hot region of the furnace with the samples. The way, which has been chosen to overcome this problem, is to transfer the samples in the cold furnace, purge and heat afterwards. When critical temperatures for oxidation are reached oxidants have already been purged.

inert gas: The last source of oxidants leading is the annealing atmosphere itself. The used N_2 has a purity of 5.0 and contains an amount of 3 ppm moisture, which is sufficient for a slow oxidation of the small amount of the implanted Ge. The complex interplay between the clustering of Ge and the oxidation is described elsewhere [OSH00, BHSO00]. Additionally, the oxidation could change the Ge concentration profile [HSM+99]. This source of moisture can be eliminated by annealing under vacuum conditions, which are not available at present.

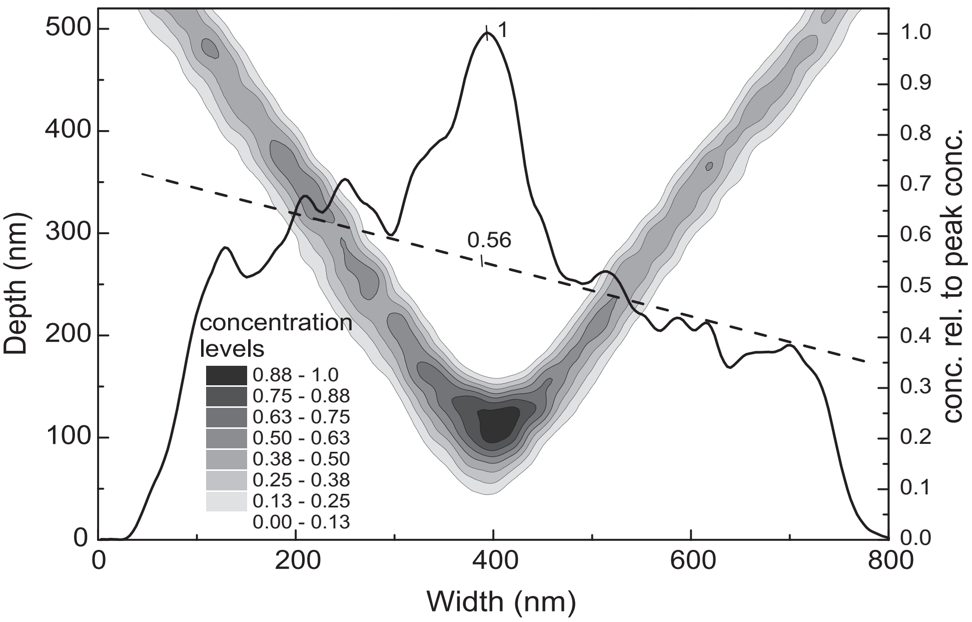

Figure 2.5: STEM-EDX Ge mapping on a cross-section of an as-implanted sample. The grayscale corresponds to the Ge concentration relative to the maximum concentration of 30 % in the V-groove bottom. The solid curve shown is the projection of the Ge concentration onto the horizontal axis. The average Ge content in the sidewalls is shown by a dashed line, which discriminates the Ge enriched bottom from the sidewalls.

Consequently, tiny amounts of oxidants play a major role for the synthesis of thin nanowires made from elemental Ge. Some amount of the Ge is consumed during the oxidation process but prevents a larger influence on the nanowire formation. This also explains the large ion fluence used for the nanowire formation. Lower Ge concentration achieved by lower ion fluences have not lead to a wire formation. Generally speaking, the optimization of the nanowire growth is tightly bound to the reduction of oxidants.

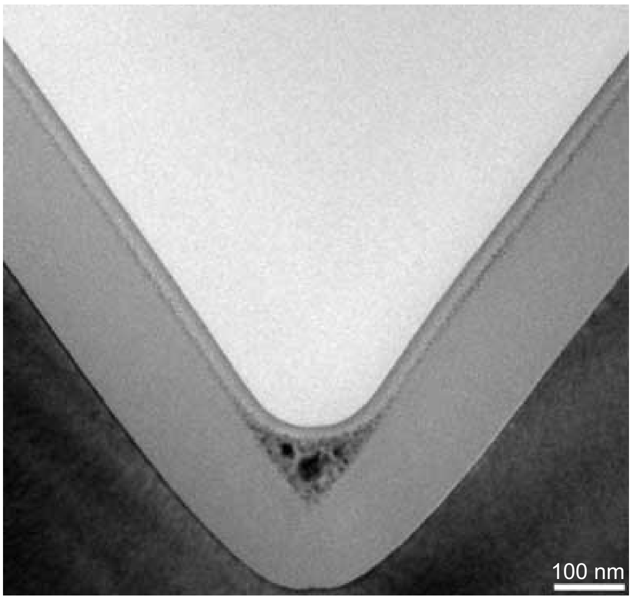

(a) overview of an annealed V-groove

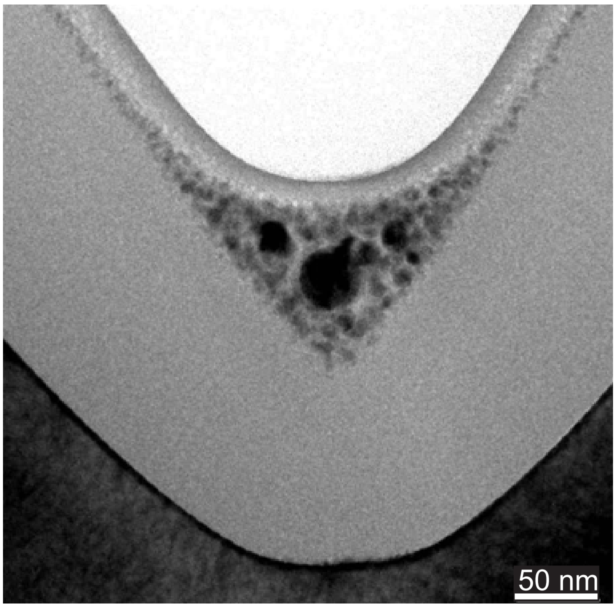

(b) bottom of an annealed V-groove

Figure 2.6: XTEM images of an Ge implanted and annealed V-groove. Shown are (a) an overview and (b) the bottom region of the V-groove. The sample was annealed in N_2 at 950 °C for 10 minutes, thereby it has been transferred into the cold furnace to minimize the intake of oxidants from air. The large black dot in the V-groove bottom is the cross-section of the expected Ge nanowire with a diameter of 35 nm.

Chapter 3

A Model of Surface Evolution under Ion Irradiation

The growth of a Ge nanowire in the V-groove bottom will be largely affected by the spatial distribution of the implanted Ge atoms. Thereby, the maximum concentration and the broadness of the concentration profile may decide whether a wire is formed during subsequent annealing. Furthermore, the Ge depth profile in the SiO_2 differs considerably from the Gaussian shape usually observed for ion implantation into flat targets.

Thus, the main subject of this chapter is to clarify the impurity atom distribution within the oxide covered V-grooves. Ion implantation itself would lead to a more or less Gaussian depth distribution of Ge atoms. But the energetic ion bombardment also erodes the surface by sputtering of target atoms. Eventually these atoms may escape, but on curved target a certain fraction is redeposited on other parts of surface. This additional erosion and deposition process taking place during the irradiation will mainly change the surface shape. On the other hand, the surface is the reference point for the slowing down of the incident ions in the target. Changing the position of the surface will always affect the resulting profile of the implanted atoms. These two problems appear to be highly entangled and can not be solved easily. The way presented here discusses first the erosion and deposition during ion irradiation and thus the change of the surface. For this reason a novel analytical continuum model is developed. The evolution of an arbitrary surface under ion irradiation is predicted and compared for the case of oxidized Si V-grooves to cross sectional TEM images, which has been reported in [MHS00].

Having predicted the surface shape after ion irradiation, it is possible to estimate the Ge profile in the oxide layer covering the Si V-groove. Surprisingly, it reveals a strong Ge enrichment in the V-groove bottom, which has also been proven by STEM-EDX measurements presented in the last chapter, (figure 2.5). As the simulation shows this enrichment is mainly caused by the redeposition of Ge rich material into the V-groove bottom. Thus, it is absolutely necessary to understand the enrichment process to further optimize the nanowire growth conditions. The side effects of ion implantation, i.e. sputtering strongly promotes the nanowire growth in the present case.

3.1 Sputtering Yield

Sputtering is the removal of atoms from the surface by the impact of energetic particles. It is a widespread experimental technique and used as a basic tool in a large number of sophisticated applications, e.g. in surface science, depth profiling, sputter cleaning, sputter deposition, and micromachining. On the other hand, sputtering is always present as side effect during high fluence implantation of heavy ions and is, therefore, not negligible for the nanowire synthesis.

Sputtering of a flat surface is phenomenologically described by the sputtering yield Y, which is the average number of removed atoms per incident ion.

$$Y = \frac{\text{\# of removed atoms}}{\text{\# of incident ions}} \tag{3.1}$$

The sputtering yield Y has been extensively examined in the past for amorphous targets [Beh81], [Eck91], reviews can be found in [NMH96] and [Mal94]. It will depend on the ion energy, the ion-target combination, the angle of incidence φ of the ion beam, and the surface roughness of the target. Neglecting all other influences, the dependence on the angle of incidence φ can be expressed according

$$Y(\varphi) = \begin{cases} Y_0 \cos^{-n}\varphi & \text{Sigmund, [Sig69]} \\ Y_0 \cos^{-f_s}\varphi \times \exp\left[-b\left(\cos^{-1}\varphi - 1\right)\right] & \text{Yamamura, [YII83].} \end{cases} \tag{3.2}$$

In both cases, Y_0 is the sputtering yield for normal ion incidence. The fit parameter n of Sigmund's formula is about 2 and depends weakly on the mass ratio between incident ions and target atoms. Despite the good fit to experimental data for small angles [EGRRO93], it shows an unrealistic singularity for glancing angles, i.e. this formula is restricted to $\varphi \leq 60 \ldots 70\,°$. Accounting for ion reflection, Yamamura [YII83] proposed an alternative formula for light-ion sputtering, which can be also used as an approximation for heavy ions. The main difference is, that the sputtering yield approaches zero for glancing angles. Here the parameter should be estimated from experiments and the sputtering yield exhibits a maximum for the angle $\theta_{opt} = \cos^{-1}(b/f_s)$. Both formulas were used for figure 3.4 to fit the experimental values of Y for Ge^+ implantation into SiO_2.

3.1.1 Simulating the Sputtering Yield with SRIM

Ion implantation is essentially a stochastic process of multiple scattering events of the primary ion in the target matrix. Thus, a Monte Carlo (MC) approach should be able to describe more accurately the slowing down and the scattering of energetic ions in solids than an analytical calculation based on transport theory. The MC method relies on the binary collision approximation. Each collision cascade is regarded a sequential series of binary scattering events of the energetic particle with host atoms plus a continuous slowing down in the electron gas. Subsequently, scattered host atoms with sufficient energy can create secondary scattering cascades. A commonly used MC code for ion ranges and damage distributions in amorphous materials is TRIM (transport of ions in matter) [BH80], where the modern version

Angle $\boldsymbol{\varphi}$ (°)	0	10	20	30	40	50	54.7	60	70	80	85	87
$\mathbf{Y}(\varphi)$	2.5	2.5	3.0	4.2	6.1	9.2	11.4	14.9	26.7	44.4	45.8	40.7
$\mathbf{R_p}$ (nm)	49	48	46	42	37	31	28	25	18	13	11	11
$\triangle\mathbf{R_p}$ (nm)	14.8	14.7	14.5	14.1	13.5	12.7	12.2	11.7	10.3	8.5	7.7	7.5
$\boldsymbol{\sigma}$ (nm)	11	14	20	27	34	40	42	45	48	50	50	51

Table 3.1: Projected range R_p, longitudinal straggling $\triangle R_p$, lateral straggling σ, and the sputtering yield Y in dependence on the angle of ion incidence for 70 keV Ge^+ implantation into SiO_2 using Ziegler's SRIM 98.4 code [ZBL85].

SRIM 98.4 [ZBL85] was used for the presented simulations of 70 keV Ge^+ implantation into SiO_2, shown in table 3.1 and figure 3.4.
The following parameter were used in the simulation

$$\rho_{\mathrm{SiO_2}} = 2.32\ \mathrm{gcm^{-3}} = 6.9 \times 10^{22}\ \mathrm{cm^{-3}} \quad \text{target density} \tag{3.3}$$
$$E_B = 2.0\ \mathrm{eV} \quad \text{binding energy} \tag{3.4}$$
$$E_D = 0\ \mathrm{eV} \quad \text{displacement energy} \tag{3.5}$$
$$E_{SBE} = 4.7\ \mathrm{eV} \quad \text{surface binding energy (SBE).} \tag{3.6}$$

The displacement energy E_B was set to zero to since defect generation and recombination does not affect the sputtering yield. For the SiO_2 density the preset value was used, which is too high. In general, the density depends on the synthesis of the SiO_2 and lies in a range of 2.24 . . . 2.28 g/cm^3. Nevertheless, the overestimated density affects the result only to a very small extent.
The greatest influence has the SBE on the sputtering yield $Y(\varphi)$, which is the energy barrier recoil atoms have to overcome to leave the solid. The SBE can be approximated by the sublimation energy of SiO_2, which is almost impossible to determine. Thus the SBE of silicon was used instead leading to comparably good results[1]. Following the suggestion of SRIM, a relative error in the order of 10% has to be considered.

3.1.2 Sputtering Induced Stationary Surface Concentration

During high fluence ion implantation the concentration of implanted atoms saturates at a maximum near the surface[2], which is caused by sputtering. Consider the implantation of Ge^+ into SiO_2 and the sputtering of the target surface. Thereby, the surface is assumed to be perfectly flat and, further, ions are implanted under normal incidence.
The particles currents entering or leaving the target are shown in figure 3.1. Hereby, J_{Ge} and $J_{\mathrm{SiO_2}}$ denotes the current densities of Germanium and SiO_2 leaving the target and the current density of incoming ions is given by J_i. The near surface concentrations of Ge and SiO_2 is denoted by N_{Ge} and $N_{\mathrm{SiO_2}}$. During the erosion the

---

[1] The heat of fusion for $Si + 2O \rightarrow \mathrm{SiO_2}$ could be used instead leading to an SBE of 4.8 eV.

[2] The near surface concentration is regarded to be the atomic concentration of one species within the bulk close to the surface (< 1 nm).

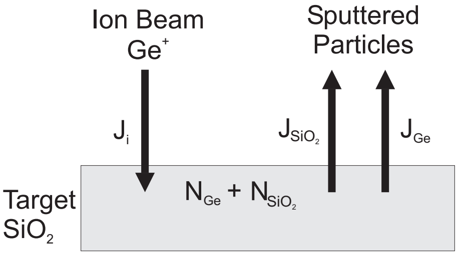

Figure 3.1: Current densities and concentrations during Germanium implantation into SiO_2

influence of preferential sputtering is neglected. Hence, the ion beam does not alter the target stoichiometry by sputtering. Only implantation changes the composition of the target. Under this assumption one can treat SiO_2 jointly, which means that the ration between sputtered silicon and oxygen is 1:2. Then, the connection between the ingoing and outgoing current density is given by the sputtering yield Y

$$J_i\,Y = J_{Ge} + J_{\mathrm{SiO}_2}. \tag{3.7}$$

In the first approximation the concentration of implanted Ge N_{Ge} can be regarded as a box-shape like profile extending up to the projected range R_p. Particle conservation then gives $N_0 = N_{Ge} + N_{\mathrm{SiO}_2} = \text{const.}$ and

$$R_p\,\frac{dN_{Ge}}{dt} = J_i - J_{Ge}. \tag{3.8}$$

Introducing the ratio $N_{Ge}/N_0 = c_{Ge}$ as a new variable simplifies the current densities to

$$J_{Ge} = c_{Ge}\,Y\,J_i \qquad\qquad J_{\mathrm{SiO}_2} = (1 - c_{Ge})\,Y\,J_i. \tag{3.9}$$

So equation (3.8) is rewritten as

$$R_p\,N_0\,\frac{dc_{Ge}}{dt} = J_i(1 - Y\,c_{Ge}) \tag{3.10}$$

as long as $c_{Ge} \ll 1$ with the solution of

$$c_{Ge} = Y^{-1}\left(1 - \exp\left(-\frac{d_{sp}}{R_p}\right)\right) \qquad \text{and} \qquad d_{sp} = \frac{D}{N_0}\,Y, \tag{3.11}$$

if Y remains constant independent of c_{Ge}. Thereby, d_{sp} denotes the thickness of the eroded surface layer and D is the total fluence of implanted Ge^+ ions. In the long time limit the Ge concentration near the surface saturates.

$$\lim_{d_{sp}\to\infty} c_{Ge} = 1/Y \tag{3.12}$$

This value is roughly reached after the erosion of a layer three times as large as the projected range, which corresponds to a fluence of $D = N_0 d_{sp}/Y$.

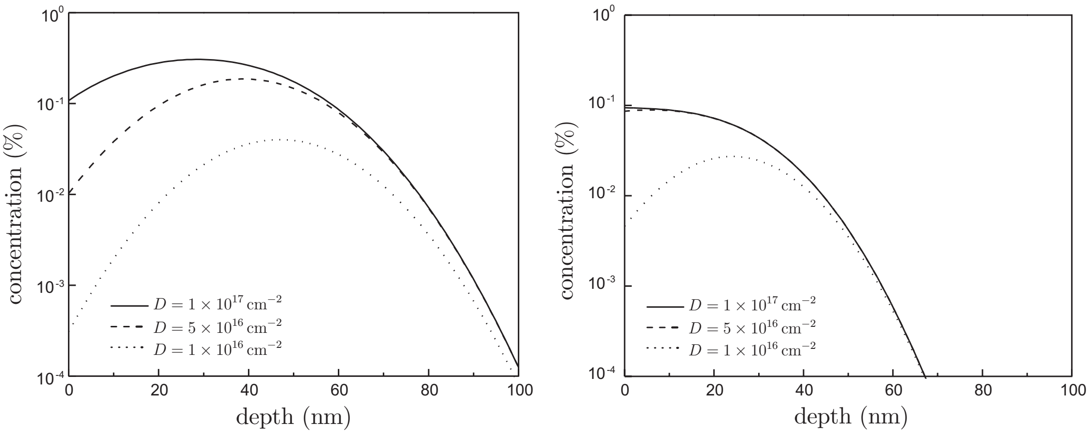

(a) normal ion incidence

(b) oblique ion incidence (54.5 °)

Figure 3.2: Estimated Ge profile according equation (3.13) for 70 keV Ge^+ implantation into SiO_2 (a) at normal ion incidence and (b) incidence under (54.5 °).

As an example, suppose the implantation of 70 keV Ge^+ into SiO_2 with a sputtering yield Y equal to $Y = 2.7$, see therefore next section. The atomic density of SiO_2 is $N_0 = 6.6 \times 10^{22}$ cm^{-3} and the projected range $R_p = 49$ nm (table 3.1). According equation (3.12), the stationary Ge concentration will be $c_{Ge} = 1/2.7 = 37\%$, which is reached after sputtering a layer $d_{sp} = 3 \times R_p = 147$ nm thick with a total fluence of $D = 3.6 \times 10^{17}$ cm^{-2}.
The simple model discussed here can be further advanced as described in [KP73]

$$c(x) = \frac{N_0}{2Y}\left[\operatorname{erf}\left(\frac{x - R_p - \frac{DY}{N_0}}{\sqrt(2)\triangle R_p}\right) - \operatorname{erf}\left(\frac{x - R_p}{\sqrt(2)\triangle R_p}\right)\right]. \tag{3.13}$$

It then includes also the influence of the longitudinal straggling $\triangle R_p$ (table 3.1) and is suited to describe the Ge depth profile $c(x)$ achieved by ion implantation and sputtering which is shown in figure 3.2.
As visible, the Ge concentration has saturated at 10% for slanted ion incidence due to the high sputtering yield $Y(54.7\ ) \approx 10$ while at normal ion incidence the saturation has not been reached. Consequently, the Ge concentration achievable in the V-grooves sidewalls is low compared to the bottom which facilitates the wire growth there.
Given the steady state, for each implanted ion is in average one atom of the same species sputtered. This knowledge provides the possibility to measure the sputtering yield of the target material without conflicting with the ion beam material used in the next section.

3.1.3 Focused Ion Beam Sputtering

The focused ion beam (FIB) of the Research Center Rossendorf was used to measure experimentally the angular-dependent sputtering yield of 70 keV Ge^{++} ions

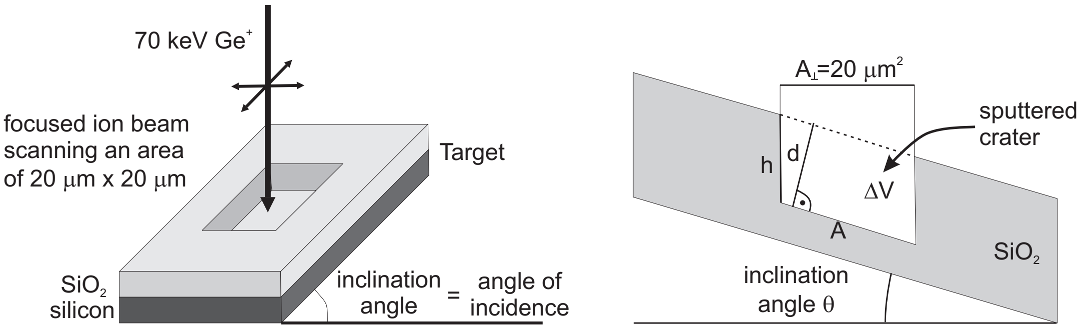

(a) sputtered crater on the slanted sample

(b) cross section of the crater

Figure 3.3: Scheme of sputtered crater created by focused ion beam sputtering of SiO_2 with 70 keV Ge^+.

implanted into SiO_2. Ge ions from a liquid metal ion source were accelerated by 35 kV forming a focused ion beam with a diameter of 300 nm. Seven holes were sputtered with decreasing fluence into a wet oxidized Si wafer, mounted on a slanted metal block. A schematic sketch of the experimental conditions is shown in figure 3.3. This procedure was repeated for different inclination angles up to 80 ° and the holes were profiled ex-situ with needle depth profiling (Dektak 8000). Thereby, the samples were scanned with a needle, pressed with a force of $F = 0.3$ N onto the surface. The measured depth d of the craters allows to calculate the loss of volume which is a direct measure of the sputtering yield. The used procedure is similar to ref. [BT98] and applies the steady state considerations from last section.

The volume of the removed SiO_2 is

$$V_{crater} = A_\perp\, h = A_\perp\, d\, cos\theta = A\, d \tag{3.14}$$

$$= Y \frac{D\, A_\perp}{N_0} = Y \frac{D}{N_0} cos\theta\, A. \tag{3.15}$$

Combining both equations and solving for Y gives

$$Y = \frac{d\, N_0}{D \cos\theta}. \tag{3.16}$$

The calculated sputtering yield Y accounts for the removal of the target material (SiO_2) and the implanted species (Ge) itself. Assuming that the surface is already in the steady state at the beginning of the implantation, one Ge atom is sputtered in average for each Ge^+ ion implanted[3]. Since this process does not result in a volume loss, the partial sputtering yield of SiO_2 $Y_{\mathrm{SiO_2}}$ is equal to Y

$$Y_{\mathrm{SiO_2}} = Y = \frac{d\, N_0}{D \cos\theta}. \tag{3.17}$$

---

[3] This assumption is satisfied since the average crater depth is large compared to the projected range $R_p = 49$ nm.

The fluence is here derived from the ion current I_{Ge} and the exposure time $t_{sp} = 1789$ s by

$$D = \frac{I_{Ge}\, t_{sp}}{A_{\perp}\, e}. \tag{3.18}$$

The average fluence has been $2.75 \times 10^{17}\,\mathrm{cm}^{-2}$ with an ion flux density of $1.54 \times 10^{14}\ \mathrm{cm}^{-2}\mathrm{s}^{-1}$, which is much higher than the usual flux density in the beam line implantation. The measured sputtering yield $Y(\varphi)$ is therefore not directly transferable to beam line conditions, but it is a first approximation neglecting a possible influence of the ion flux density on sputtering yield.

The measured values of the sputtering yield Y are shown in dependence on angles of incidence in figure 3.4 together with the simulated values using SRIM 98.4 (table 3.1). The experimental values were further used to fit Sigmund's and Yamamura's sputtering formula from equation (3.2). Both equations agree quite nicely with the experiment up to an inclination angle of 60 °. Beyond this angle, the agreement between the formulae and the experiments is lost, mostly due to inadequate description of sputtering by Sigmund and Yamamura. In that region ion reflection and the heavy mass of the Ge^{+} ion itself has to be considered, which is not fully implemented in the analytical formulae. Additionally, the experimental technique for the measurement of the sputtering yield becomes erroneous for high angles. However, the highest inclination angle in the V-groove geometry is less than 60 ° and allows therefore a satisfying description of sputtering in this geometry.

The experimental quantities are in general uncertain and the sputtering is therefore connected with experimental error. A relative error of $\triangle d \cong 5$ nm is assumed for the depth profiling. Other sources of experimental errors are comparably unimportant ($\triangle\theta \cong 0.1\,°$). The time and current measurements are regarded as exact. The relative error of Y is then estimated by

$$\begin{aligned} \frac{\triangle Y}{Y} &\cong \frac{\triangle d}{d} + \frac{\sin\theta\ \triangle\theta}{\cos\theta} = \frac{\triangle d}{d} + \tan\theta\,\triangle\theta \qquad (3.19)\\ &\cong 5\% + 0.2\%\tan\theta. \qquad (3.20) \end{aligned}$$

In addition, the uncertainty within the model has to be considered. The steady state condition is not given for all fluences. Especially, for short times (low fluences) the Ge concentration has not yet reached the steady state and the sputtering yield is still changing. In this regime, the additive contribution in equation (3.17) is less than one.

Furthermore, a preferential sputtering was excluded from the consideration but could substantially affect the result. For SiO_2, oxygen may be sputtered more likely than silicon resulting in a silicon enrichment near the surface. This in turn will clearly determine the measured sputtering yield. So in summary, a relative error of approximately $\triangle Y/Y = 10\%$ has to be assumed and is shown as error bars in figure 3.4.

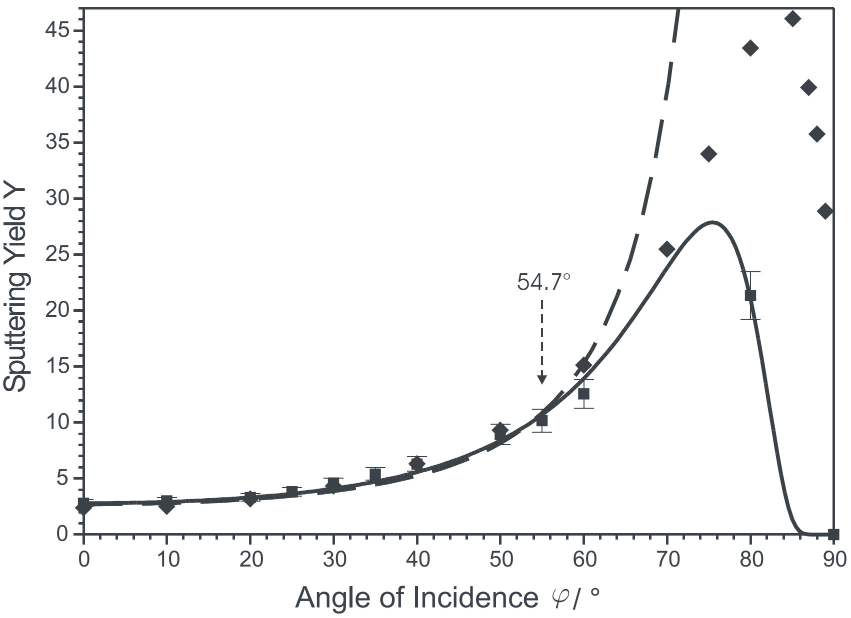

Figure 3.4: Sputtering yield of SiO_2 during 70 keV Ge^{++} ion irradiation. (■) Experimental values of the present work measured by focused ion beam irradiation according to a procedure described in [BT98], (♦) SRIM98.4 simulation [ZBL85]. Curves are fitted to the experimental data using Sigmund's (dashed line, $Y_0 = 2.7$, $n = 2.5$) and Yamamura's formula (solid line, $Y_0 = 2.7$, $f_s = 3.2$, $b = 0.74$), eq. (3.2) are presented.

3.2 The Continuum Model of Surface Evolution

A novel analytical model for the surface morphology evolution is introduced in this section. Sputtering and redeposition of sputtered atoms are treated in a continuum framework and relies on the experimental measured sputtering yield $Y(\varphi)$. The model aims to describe the short time surface evolution, where roughening effects are still negligible. For a comparison to other models of surface evolution see chapter 3.4.

The surface is described by a single valued, continuous function $h(x,t)$, which excludes artificial surface formations like overhangs[4] from the theoretical treatment. Further, an advantage of the V-groove geometry is exploited. Only an one-dimensional cross section perpendicular to the $< 110 >$ direction (the V-groove) has to be used to characterize the surface. This is reasonable as long as anisotropic effects can be neglected.

Following the usual experimental conditions, normal ion incidence with respect to the x-axis is assumed. Thus, the surface inclination angle φ is equal to the angle φ between the surface normal and the direction of the ion beam. Simplifying the complex target material, an equal atomic volume for all incorporated species is assumed. The leads directly to an average target description, which does not account

---

[4] Although redeposition may lead to overhang formation. But it is convenient to neglect this for the initial evolution.

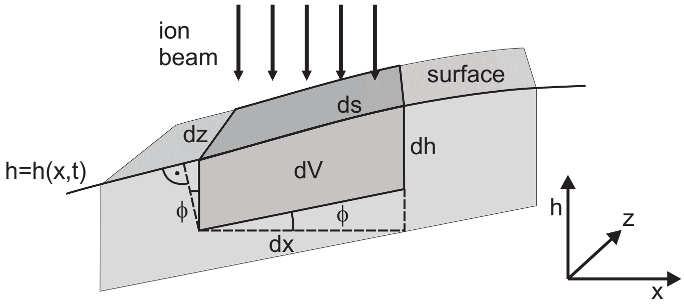

Figure 3.5: Relation between differential volume of sputtered material dV and recession height dh

for any chemical effect. Especially, there will be no discrimination between the target material and the ion species.
With the evaluation of this model one finally obtains the surface shape after ion irradiation which in turn is used to estimate the retained Ge concentration in the V-groove. Again, the discussion is based on the assumption of a local steady state between ion implantation and sputtering.

3.2.1 Sputtering and Swelling

At first the influence of sputtering has to be treated. Therefore, the volume loss by sputtering is calculated which is connected to the surface recession in time (figure 3.5)

$$dV = \frac{\Phi\,(Y(\varphi) - 1)}{\rho}\, dA\, dt = \frac{\Phi\,(Y(\varphi) - 1)}{\rho}\, ds\, dz\, dt. \tag{3.21}$$

Thereby, Φ denotes the ion flux density and ρ the atomic density of the target. Furthermore, the implanted atoms would require a finite volume. The resulting swelling of the target has already been included by the minus one in the equation (3.21), which uses the approximation that each atom requires an equal volume[5]. Substituting the volume element $dV = dh\, dx\, dz = dh\, ds\, dz \cos\varphi$, an equation for the surface recession in time can be given

$$\frac{\partial h(x,t)}{\partial t} = -\frac{\Phi}{\rho} \frac{Y\,(\varphi) - 1}{\cos\varphi}. \tag{3.22}$$

Further, the cosine of the inclination angle φ can be expressed by the first spatial derivative $h'(x)$

$$\frac{\partial s}{\partial x} \equiv \frac{1}{\cos\varphi} = \sqrt{1 + \left(\frac{\partial h}{\partial x}\right)^2}. \tag{3.23}$$

---

[5] For Ge^+ implantation into SiO_2 the Ge atoms may need less space, since the could occupy interstitial positions and are not incorporated in the SiO_2 network.

Using Sigmund's formula (equation (3.2)) and replacing $\cos\varphi$ in equation (3.22) a partial differential equation for the surface morphology evolution has been derived

$$\frac{\rho}{\Phi}\frac{\partial h(x,t)}{\partial t} = \underbrace{\frac{\partial s}{\partial x}}_{\text{swelling}} - \underbrace{Y_0\left(\frac{\partial s}{\partial x}\right)^{n+1}}_{\text{sputtering}} \tag{3.24}$$

$$= \sqrt{1+\left(\frac{\partial h}{\partial x}\right)^2} - Y_0\left(1+\left(\frac{\partial h}{\partial x}\right)^2\right)^{\frac{n+1}{2}} . \tag{3.25}$$

Consequently, a similar substitution can be carried out with Yamamura's formula, equation (3.2), leading to a slightly more complicated version. The validity of this equation is extended up to higher inclination angles of the surface

$$\frac{\rho}{\Phi}\frac{\partial h(x,t)}{\partial t} = \underbrace{\frac{\partial s}{\partial x}}_{\text{swelling}} - \underbrace{Y_0\left(\frac{\partial s}{\partial x}\right)^{f_s+1} \times \exp\left[-b\left(\frac{\partial s}{\partial x}-1\right)\right]}_{\text{sputtering}} \tag{3.26}$$

$$= \sqrt{1+\left(\frac{\partial h}{\partial x}\right)^2} - Y_0\left(1+\left(\frac{\partial h}{\partial x}\right)^2\right)^{\frac{f_s+1}{2}} \times \exp\left[-b\left(\sqrt{1+\left(\frac{\partial h}{\partial x}\right)^2}-1\right)\right] . \tag{3.27}$$

Both equations (3.25) and (3.27) describe the evolution of the surface due to sputtering and swelling in an average continuum picture. The first term in both equations represent the target swelling and is always positive, whereas the second term accounts for the sputtering and is negative. The parameter n in equation (3.25) and f_s, b in equation (3.27) can be determined by fitting Sigmund's or Yamamura's formulas (equations (3.2)) to the experimentally measured sputtering yield $Y(\varphi)$. This provides a reliable knowledge on Y for the evolution model.

The evolution equations are highly nonlinear and can not be solved in a closed analytical form for arbitrary initial conditions. A trivial solution is found for an initially flat surface. It remains unchanged in the shape and is being eroded during time according the sputtering yield $(Y(\varphi)-1)$ [6]. Both equations (3.25) and (3.27) are closely related to the deterministic Kardar-Parisi-Zhang (KPZ) equation [KPZ86], which will be shown in section 3.4 by an expansion for small surface gradients.

3.2.2 Redeposition of Sputtered Atoms

For a curved target surface a certain fraction of sputtered material will be redeposited onto other parts of the surface, which results in a reduction of the effective sputtering yield [KEDR98]. In general, redeposition of sputtered material is a nonlocal process, which complicates the mathematical description. Local equations like equation (3.25) can not correctly account for this effect and have to be generalized to an integro-differential equation over the whole sample surface.

---

[6] It has been assumed that the sputtering is stronger than the swelling, otherwise an effective deposition occurs.

In the literature, redeposition has been considered in the very beginning state of the surface evolution under ion irradiation [BW80, BW81], but a complete dynamic description is missing.

For the redeposition process, the parameter with the highest influence is the angular distribution $f(\theta, \varphi)$ of atoms ejected under ion bombardment of solid surfaces. It is one of the long-standing problems in sputtering theory which is yet to be solved even for elemental targets.

$$f(\theta, \varphi) = \frac{n+1}{2\pi} \cos^n \theta \qquad \begin{cases} n < 1 & \text{undercosine distribution} \\ n = 1 & \text{cosine distribution} \\ n > 1 & \text{overcosine distribution} \end{cases} \tag{3.28}$$

The conventional theoretical models predict a cosine distribution ($n = 1$) of ejected atoms corresponding to isotropic cascades in an infinite amorphous medium [Sig69]. Measurements, on the other hand, exhibit many examples of undercosine ($n < 1$, [TKH$^+$98]) or overcosine ($n > 1$, [CTO96, TUO99]) angular distributions. Even at large incident energies the angular distribution function is described by an universal target-independent function closely matched $\cos^2 \theta$, [Shu00]. This is also confirmed by calculations including the influence of the target topography on the angular distribution [ZWCW96].

Moreover, the three dimensional distribution function $f(\theta, \varphi)$ has to be adapted to the one dimensional description of the V-groove, which is achieved by a projection of $f(\theta, \varphi)$ onto the xh-plane. In other words, for the topology evolution it is unimportant onto which position along the groove the particles are deposited. Moreover, the height and the distance from the bottom are important and captured by the projected distribution $f_{2D}(\theta_{2D})$, which determines the probability $f_{2D}(\theta_{2D})\, d\theta_{2D}$ that a sputtered particle is ejected into the angular element $d\theta_{2D}$. The full derivation of the projection is given in appendix A.1 and in the following the angle $f_{2D}(\theta_{2D})$ is shortened to $f(\theta)$ keeping in mind that only the one-dimensional description is used

$$f_{2D}(\theta_{2D}) = \frac{n+1}{2\pi} B\left(\frac{1}{2}, \frac{n+1}{2}\right) \cos^n \theta \qquad n > 0. \tag{3.29}$$

The Beta function can be defined by the use of the Gamma function $B(c, d) = \Gamma(c)\Gamma(d)/\Gamma(c+d)$. Additionally, the ejected atoms can obey a preferential direction. This is accounted for by a tilted emission distribution

$$f_{2D}(\theta_{2D}) = \frac{n+1}{2\pi} B\left(\frac{1}{2}, \frac{n+1}{2}\right) \cos^n(\theta - \tau). \tag{3.30}$$

The angle τ is the ejection angle with the highest probability density and expresses the forward sputtering.

In the further derivation shadowing of selected surface areas is neglected, this directly implies a convex surface shape. The reasons for are basically the complications arising from an analytical discussion of shadowing. It might be more fruitful to implement shadowing directly into a numerical solution, which was chosen as practical compromise. In general, shadowing introduces a second instability during erosion.

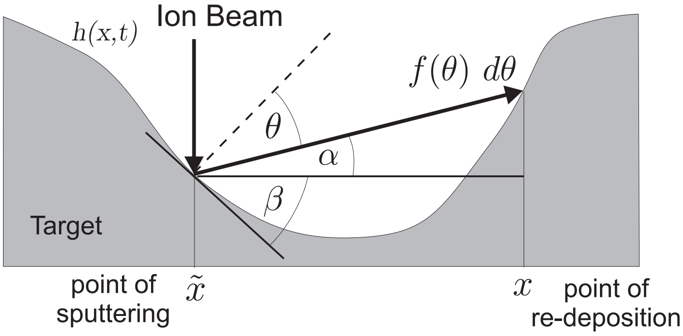

Figure 3.6: Redeposition geometry in one dimension. Atoms are sputtered at the point $\tilde{x}$ and arrive at x with the probability $f(\theta)\,d\theta$.

Surface asperities have a higher likelihood of growing since eroded material is collected. This process has been studied for deposition and growth [KBR89, RG91]. On the other hand, shadowing could be neglected at all if one restricts to the main part of the V-groove. This surface is convex and also stays convex during the evolution. In that case, the point of ejection of a particle by sputtering $\tilde{x}$ and the point of attachment to the surface x is then given by

$$\left.\frac{\partial h(x,t)}{\partial t}\right|_{redeposition} dx = -\left.\frac{\partial h(\tilde{x},t)}{\partial t}\right|_{sputtering} d\tilde{x} \times f(\theta)\left(\frac{\partial \theta}{\partial x}\right) dx. \tag{3.31}$$

A sticking coefficient of one expresses here that each arriving atom actually sticks to the surface and is only removed by a second sputtering event. For redeposition only those atoms sputtered from $\tilde{x}$ reaching the surface $h(x)$ at any point x are of interest. According figure 3.6, θ is related to $\tilde{x}$ and x by

$$\theta = \theta\left(x, \tilde{x}\right) = \underbrace{\arctan\left(\frac{h\left(\tilde{x}\right) - h\left(x\right)}{\tilde{x} - x}\right)}_{\alpha} - \underbrace{\arctan\left(\left.\frac{\partial h}{\partial x}\right|_{x=\tilde{x}}\right)}_{\beta} + \frac{\pi}{2}. \tag{3.32}$$

Using equations (3.31) and (3.32) an integro-differential equation for the redeposition has been found

$$\left.\frac{\partial h(x,t)}{\partial t}\right|_{\text{redeposition}} = -\int \left.\frac{\partial h(\tilde{x},t)}{\partial t}\right|_{\text{sputtering}} f(\theta)\left(\frac{\partial \theta}{\partial x}\right) d\tilde{x}. \tag{3.33}$$

Adding equation (3.33) to equation (3.27) leads to the final equation including sputtering, swelling and redeposition

$$\begin{aligned}\frac{\rho}{\Phi}\frac{\partial h(x,t)}{\partial t} = {} & \underbrace{\frac{\partial s}{\partial x}}_{\text{swelling}} - \underbrace{Y_0\left(\frac{\partial s}{\partial x}\right)^{f_s+1} \times \exp\left[-b\left(\frac{\partial s}{\partial x} - 1\right)\right]}_{\text{sputtering}} \\ & + \underbrace{\int Y_0\left(\frac{\partial s}{\partial \tilde{x}}\right)^{f_s+1} \times \exp\left[-b\left(\frac{\partial s}{\partial \tilde{x}} - 1\right)\right] f\left(\theta[\tilde{x}, x]\right)\left(\frac{\partial \theta[\tilde{x}, x]}{\partial x}\right) d\tilde{x}}_{\text{redeposition}}. \end{aligned} \tag{3.34}$$

The evolution equation uses Yamamura's description of the sputtering yield, equation (3.2). With Sigmund's formula this could be slightly simplified but is less valid for high inclination angles.

3.2.3 Approximations

The model for the surface topology evolution, derived above, is bound to certain approximations, which has to be noted to avoid pitfalls.

Continuum picture: Only the surface of the material is treated and the specific composition at the surface is averaged. Thus, a change in the sputtering yield Y or in the emission distribution function $f(\theta, \varphi)$ of the sputtered atoms can not be accounted for. Ion implantation of heavy ions into a light matrix is such a case. The compositions changes dramatically during the implantation and as a result the sputtering yield is affected. Moreover, crystalline materials exhibit non-cosine emission distributions with large ejection probabilities for the most open crystal directions [NRZN00].

Analytical surface representation: The surface can only be approximated by a smooth function on a mesoscopic scale. It makes no sense to transfer this description to the atomic level. The sputtering yield, measured for macroscopic flat surfaces, will lose its validity and the sputtering yields becomes curvature dependent [BH88]. In addition, redeposition of sputtered atoms could lead to overhang formation, which is a pronounced limit of the model. The surface is no longer describable by an analytical function, which has been a major assumption used here.

Asymptotics: Simulations of asymptotic behavior always require special care. In our case, the measured sputtering yield is associated with experimental error and the model includes some approximations. Both could lead in the long time limit to a growing prediction error. Consequently, simulation results requires a cross check to experimental observations for a careful verification. Despite the model immanent approximations also the numerical algorithm applied for the solution can be a source of errors. The problem of the stability of such an algorithm is discussed more deeply in appendix A.2.

Smoothing effects and curvature dependent sputtering yield: No diffusion or averaging mechanism is up to now included in the model, since the starting point has been Sigmund's and Yamamura's formulas for the sputtering yield. This lack can partially by justified. Ion implantation is carried out at room temperature and thus thermal diffusion is unimportant. Moreover, diffusion induced by the ion beam [DS99, MB97] itself can also neglected, which is an approximation for the early stage of surface morphology evolution. In later times the surface may become rough [BML97, CV96] and the ion-induced diffusion will be an important counterpart to this roughening tendency. Additionally to the smoothing mechanisms, the sputtering yield Y could directly depend on the local surface curvature, [BH88]. Crests and valleys obey different sputtering yields for ion irradiation at low energies. For higher energies, as used here,

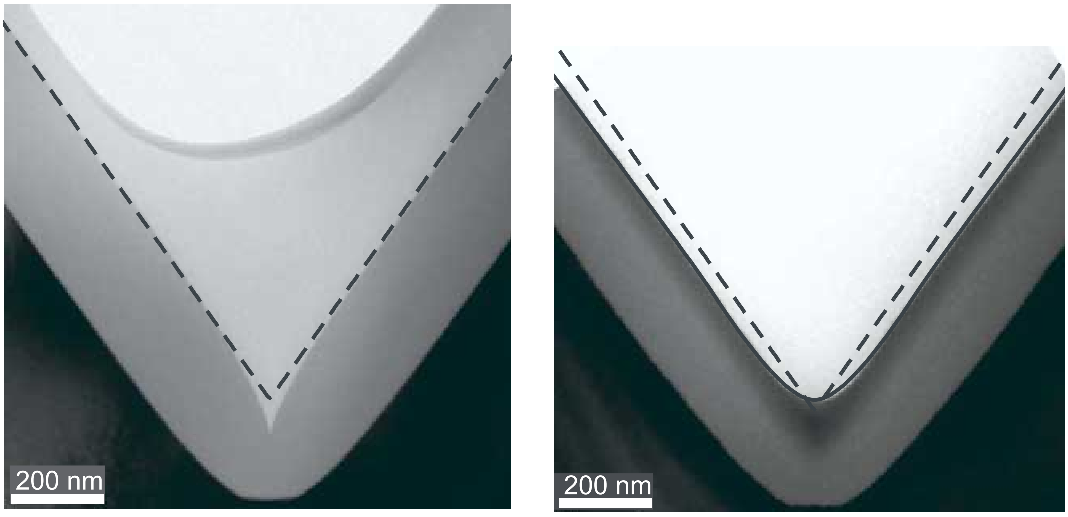

(a) as-oxidized V-groove

(b) as-implanted V-groove

Figure 3.7: Comparison of XTEM images of oxidized V-grooves before a) and after b) implantation with 1×10^{17} $\mathrm{Ge^{+}cm^{-2}}$ of 70 keV energy to the numerical solution of the surface topology evolution model. The dashed line denotes the as-oxidized SiO_2 surface, plotted in a) + b). In b) the difference between the dashed line and the SiO_2 surface is the material removed (sputtered) or added (re-deposited) by Ge^+ implantation. The solid line is the result of the numerical solution of surface evolution equation (3.34). The Si/SiO_2 interface is unaffected by the Ge^+ irradiation.

it is assumed that the ion energy is deposited sufficiently far away from the target surface to permit a direct influence of the surface curvature. Only the inclination angle remains as an important parameter for the sputtering yield Y.

Ion-induced viscous flow: Recent experiments have shown deformations on amorphous targets under ion irradiation. Especially SiO_2 reacts as if the ion beam would induce viscous relaxations, the surface seems to flow under the ion beam [MCH94, BKT98]. The origin of this plasticity is still under controversial discussions, one explanation is provided by Trinkaus [TT95]. Without going to much into the details, the plastic flow is related to electronic energy deposition of the incoming ions. This contribution is negligible for the presented case of 70 keV Ge^+ implantation into SiO_2. Consequently viscous flow under ion irradiation has not been considered here.

3.3 Shape evolution of oxidized silicon V-grooves

With the derived formalism, topology changes of V-grooves by ion implantation can be considered. Especially, the experimentally relevant implantation of 70 keV Ge^+ into oxide covered Si V-grooves was simulated here. Therefore, the measured values of the sputtering yield from chapter 3.1 were used to fit Yamamura's and Sigmund's formula for the angular dependence of the sputtering yield, shown in 3.4. Additionally, the sputtering yields are compared with simulated values using the SRIM 98.4 code [ZBL85], also shown in figure 3.4. Both results agree reasonably well for small inclination angles. For angles $\gtrsim 60$ °, which are not important in the present study of sputtering of V-grooves, some discrepancies appear. Thus, both formulas could be used for the numerical simulation of the surface evolution in the V-groove according equation (3.34) and give identical results, since angles above 54.7 ° don't occur.

Further, the angular distribution of the sputtered atoms ejected from the SiO_2 has to be specified. As a limiting case a squared cosine distribution ($f(\theta) = 1/2\ \cos^2(\theta - \tau)$) is assumed [Shu00], which is approached for high ion energies. It has to be noted that a simple cosine distribution would not lead to a correct prediction of the surface shape after ion irradiation. An overcosine distribution is indeed required to achieve the correct shape, which is also supported by a numerical simulation with the Sputter-TRIM code [EM99].

The distribution function has already been projected onto the xh-plane giving an one-dimensional description. For mathematical details of the projection see appendix A.1. Further at slanted surfaces the emission distribution is tilted downwards by an angle τ, which is considered to increase linear with the slope of the surface $\partial h/\partial x$.

$$f(\theta) = \frac{1}{2}\cos^2(\theta - \tau) \qquad \text{and} \qquad \tau = \frac{\tau_0}{\sqrt{2}}\left(\frac{\partial h}{\partial x}\right), \tag{3.35}$$

Thereby, the angle τ_0 expresses the tilt of the distribution at the slanted sidewalls of the V-groove with an slope of $\partial h/\partial x = \sqrt{2}$. As shown below, τ_0 was chosen in order to adjust the calculated V-groove shape to the shape found in XTEM images of as-implanted samples, it is in the order of 10 °. Worth noting is that τ_0 is the only free parameter remaining.

The model was solved numerically, since the equation for the derived evolution model is highly nonlinear. The predicted surface shape for a V-groove of a width of 4 μm after ion irradiation is shown in figure 3.7, and is compared to the shape of the SiO_2 surface observed by the XTEM. A nice agreement has been obtained, although an idealized initial SiO_2 surface shape without depression was assumed for the simulation. The correct simulation of a V-groove with depression is hardly possible. The inclination reaches almost 90 °, which leads to an instability in the numerical algorithm. The higher the slope the longer is the simulation time to prevent the instability. For a discussion of the stability of the algorithm see appendix A.2. Nevertheless, the depression seems the be negligible during the irradiation.

As obvious from figure 3.7, redeposition of sputtered material plays an important role during the implantation. The V-groove bottom is refilled by material sputtered from the V-groove sidewalls.

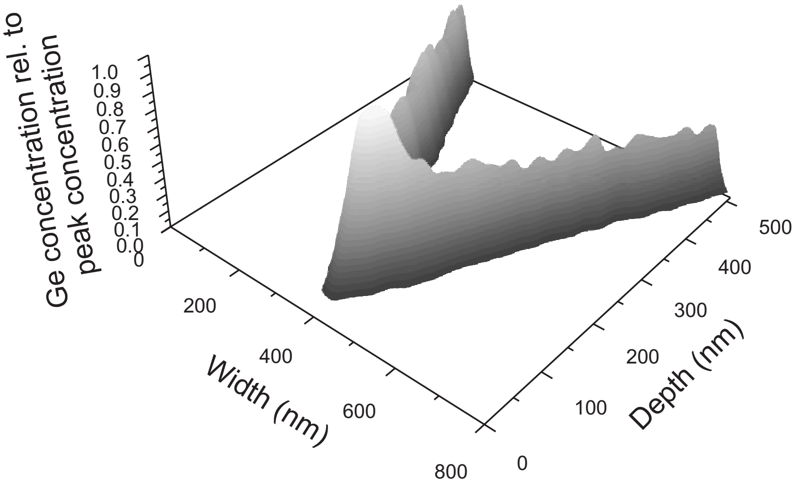

Figure 3.8: STEM-EDX Ge mapping on a cross-section of an as-implanted sample. The Ge concentration is displayed three-dimensionally relative to the peak concentration (33%) of Ge in the V-groove bottom. The Ge is higly enriched there by sputtering and the subsequent redeposition of sputtered Ge atoms.

3.3.1 Ge Enrichment in the V-groove Bottom

With the result of the refilled V-groove bottom one can also motivate Ge accumulation in the bottom. It is possible to estimate the Ge depth distribution with the knowledge of the final surface shape after Ge$^+$ irradiation.

Sputtering had a large impact on the V-groove sidewalls. Almost 61 nm of the SiO$_2$ has been eroded measured in vertical direction, which is a layer of 35 nm thickness. The eroded material corresponds to an effective sputtering yield of $Y_{eff} = 7$ according equation (3.16), which is reduced compared to the experimentally measured value of $Y_{\mathrm{SiO}_2} = 10$ in chapter 3.1.3 (figure 3.4). Nevertheless, it is assumed that the Ge concentration near the surface has reached the steady state. According to equation (3.12) the concentration is the inverse of the sputtering yield, $c_{Ge} = 1/Y = 14\%$. On the other hand, the V-groove bottom is almost unaffected by ion sputtering. Redeposition plays the major role and leads to the refilling of the V-groove bottom. Thus, the Ge concentration has not reached the sputter induced steady state.

The maximum Ge concentration for a regular implantation into an even target without sputtering is then approximately $c_{Ge} = 37\%$, which was obtained by SRIM 98.4 simulation. Additionally, redeposition adds material (Si, O, Ge) sputtered from the V-groove sidewalls, which leads to an upward shift of the surface. Thus, the implanted ions are spread out over a larger range and the Ge peak concentration is lowered. Further, not only SiO$_2$ is deposited into the V-groove bottom but also Ge. It its justified to assume that the composition of the deposited material is approximately the same as the composition of the V-groove sidewalls. Any preferential sputtering is neglected. Thus, the deposited material contains roughly 14% Ge, which leads to a further Ge accumulation in the V-groove bottom.

In summary, this estimation predicts a maximum Ge concentration of 14% in the V-groove sidewalls and a little less than 40% in the V-groove bottom. Moreover, the absolute Ge content is increased further in the bottom, since the profile is spread out during the redeposition of Ge rich SiO_2. These findings fit nicely to the experimentally verified distribution measured by STEM-EDX, see therefore figure 2.5 in chapter 2.5 and figure 3.8. The peak concentration in the V-groove bottom was measured with $c_{Ge} = 30\%$, which is twice of the Ge concentration in the V-groove sidewalls.

3.4 Relation to Other Continuum Models

Recent theoretical studies focusing on the characterization of various surface morphologies and their time evolution have used a continuum framework. The full strength of these theories arises from the prediction of the asymptotic behavior valid in the long time and large length scale limit. Nevertheless, sputter erosion is a remarkable exception, where both the short time ripple development and the asymptotic kinetic roughening have been observed experimentally. Consequently theories predicting both processes will be shortly mentioned in the following.

3.4.1 Ripple Formation and Kinetic Roughening

A rather successful theoretical model capturing many features of ripple formation was developed by Bradley and Harper [BH88] (BH). They used Sigmund's theory of sputtering [Sig69] to relate the amount of surface erosion to the energy deposited onto the surface by incoming ions. The surface becomes instable under ion irradiation, because of different erosion rates for troughs and crests, the former being eroded faster than the later. Due to this erosion mechanism they proposed a continuum equation for the surface morphology evolution in two dimensions

$$\frac{\partial h}{\partial t} = v_0(\varphi) + \nu_x(\varphi)\partial_x^2 h + +\nu_y(\varphi)\partial_y^2 h - K\nabla^4 h. \tag{3.36}$$

Here $\nu_x(\varphi)$, $\nu_y(\varphi)$ are the effective surface tensions generated by the erosion process dependent on the angle of incidence φ of the ions, K is the relaxation rate due to thermally activated surface diffusion. The sputter instability leads to negative signs of ν_x, ν_y. Equation (3.36) is linearly unstable, with a fourier mode k_c whose amplitude exponentially dominates all the others. This mode is observed as a periodic ripple structure with a wavelength $l_c = 2\pi/k_c = 2\pi\sqrt{2K/|\nu|}$, where ν is the largest in absolute value of the two surface tension coefficients. The BH model also predicts the ripple orientation as a function of the angle of incidence φ: for small φ the ripples are parallel to the ion direction, while for large φ they are perpendicular to it. Despite a good prediction of experimentally observed ripple wavelength and orientation, the BH equation (3.36) is linear and gives an unbounded growth of the ripple amplitude. It can not account for ripple stabilization and for kinetic roughening, which are both strongly supported by experiments [VDC96, EBR91]. In the long time limit nonlinear contributions become important, which can cause kinetic roughening. The time evolution of a nonequilibrium interface under nonlinear influences can be described by the Kardar-Parisi-Zhang (KPZ) equation [KPZ86]

$$\frac{\partial h}{\partial t} = \nu\nabla^2 h + \frac{\lambda}{2}(\nabla h)^2 + \eta. \tag{3.37}$$

The first term describes the relaxation of the interface due to the surface tension (ν is here a positive constant) and the second is a generic nonlinear term incorporating lateral erosion[7]. The noise $\eta(x, y, t)$ reflects the random fluctuations in the erosion process and is a set uncorrelated random numbers with zero configurational average. An initially flat surface evolves during time to a rough self-affine surface without any preferred wavelength. Moreover, any prominent surface feature vanishes during the erosion. Both equations can be combined to the Kuramoto-Sivashinsky (KS) equation, originally proposed to describe chemical waves and flame fronts [KT76].

$$\frac{\partial h}{\partial t} = -|\nu|\nabla^2 h - K\nabla^4 h + \frac{h}{2} \tag{3.38}$$

While it is deterministic, its unstable and highly nonlinear character gives rise to chaotic solutions. The short time scale solution of the KS equation shows an unstable pattern-forming behavior, with a morphology reminiscent of ripples [RK95]. The BH theory appears to be the short time solution of the KS equation. On the other hand, the long time behavior is somewhat contradictory, providing evidence for different scaling regimes. But, a formed ripple topography clearly vanishes after a transition time and a rough self-affine surface develops. A comprehensive review of the surface morphology under ion erosion including ripple development and scaling behavior is given in ref [MCB00], treating also anisotropic effects.

Nevertheless, the theoretical picture of surface evolution under ion erosion is still not completely coherent. The linear (BH) and nonlinear (KPZ, KS) models mostly treat flat surfaces with small variations like ripples. More prominent features can not adequately be described. On the other hand, a detailed and careful description for the short time evolution of the specific V-groove geometry is essential. A model has to be adjustable to experimental parameter, e.g. the sputtering yield for SiO_2 Y. Additionally, in the V-groove geometry redeposition of eroded material from one side onto the other is also a subject. Both considerations has led to the development of the sketched sputtering model in chapter 3.2.

3.4.2 Small Angle Expansion

A direct comparison of the derived equation for the surface morphology evolution under ion irradiation to the KPZ or KS model is possible for a nearly flat surface[8]. Allowing only small fluctuations, e.g. ripples with small aspect ratio, one can consider an expansion of equation (3.27) for small inclination angles, which corresponds to a small gradient $|\partial h/\partial x| \approx 0$.

$$\frac{\rho}{\Phi}\frac{\partial h(x,t)}{\partial t} = \sqrt{1+\left(\frac{\partial h}{\partial x}\right)^2} - Y_0\left(1+\left(\frac{\partial h}{\partial x}\right)^2\right)^{\frac{f_s+1}{2}} \times \exp\left[-b\left(\sqrt{1+\left(\frac{\partial h}{\partial x}\right)^2}-1\right)\right]$$

---

[7] A constant contribution ν_0 was renormalized to zero by the introduction of a moving reference frame.

[8] For the sake of simplicity not only a nearly flat but also an even surface is considered.

The surface erosion is treated according Yamamura's sputtering formula, equation (3.2) [YII83], swelling is also included. The expansion leads to

$$\frac{\rho}{\Phi}\frac{\partial h(x,t)}{\partial t} \approx (1-Y_0) + \frac{1}{2}\underbrace{\big(1+Y_0(b-f-1)\big)}_{\lambda}\left(\frac{\partial h}{\partial x}\right)^2 + \ldots . \tag{3.39}$$

The linear term in the expansion vanishes due to the symmetry of the surface erosion against the transformation $x \rightarrow -x$. The first nonlinear term corresponds to the nonlinear contribution in the KPZ equation (3.37) and the coefficient is labeled by λ. In summary, the full surface evolution equation (3.39) converges for small surface gradients to the deterministic KPZ equation. Any terms proportional to the surface curvature or higher derivatives are not captured in the model. Consequently, effects like ripple formation and surface smoothing by diffusion (thermally or ion induced) can not be accounted for.

On the other hand, the approximation of a vanishing curvature is justified if the projected range of the incident ions is large compared the height fluctuation of the surface.

3.5 Summary

The evolution of the surface shape of oxidized V-grooves on (001) Si wafer under high-fluence Ge^+ irradiation was studied experimentally and theoretically. The 4 µm wide SiO_2 covered V-grooves with a sharp apex at the bottom evolve towards a groove with rounded bottom refilled by sputtered material form the V-groove sidewalls. This leads to an Ge accumulation there, which was predicted by a novel mesoscopic model of surface evolution under ion irradiation includes the effects of sputtering, swelling and redeposition. Numerical solutions shows a very good agreement with the surface shape change found by XTEM experiments. Other effects like ion-beam induced surface diffusion or viscous flow seem to be unimportant.

Within the context of the synthesis of a nanowire at the V-groove bottom this work has clarified the role of sputtering and redeposition. The formation of a nanowire under such conditions appears strongly favored, which has not been expected.

Chapter 4

Wire Growth

The initial state for the nanowire growth is an inhomogeneous distribution of Ge atoms dispensed in the SiO_2 layer covering the surface of the Si V-groove. This highly supersaturated solid solution was achieved by the ion implantation as a nonequilibrium process. At room temperature the resulting state is kinetically inhibited and subsequent annealing is needed to initiate relaxation towards the thermodynamical equilibrium. Since Ge is almost immiscible in SiO_2 the system exhibits a phase separation of Ge and SiO_2 which is a first order phase transition. Ge will precipitate and, at high enough concentrations, coalescence occurs of Ge precipitates during the annealing step.

The focus in this section will be laid on the dynamical description of the phase separation. The tool of the Kinetic 3D Lattice Monte Carlo (KLMC) simulation is introduced to predict the evolution from a supersaturated solid solution towards the second-phase nanowire.

4.1 Basic Processes during IBS

Classical IBS usually consists of two steps, the implantation to create the solid solution of impurity atoms and the subsequent annealing to actually grow the desired nanostructures from the supersaturation of implanted impurity atoms. Thus, in a discussion of the nanowire growth one can focus on the first-order phase transition and consider the initial distribution of impurity atoms as given[1]. Then the growth of the second-phase precipitates (here Ge) during the annealing can be roughly dived into three stages

homogeneous nucleation: The precipitation of second phase nuclei is initiated by thermal fluctuations which may become stable if a critical concentration is exceeded, the nucleation threshold.

growth and coarsening: All nuclei grow as long as the concentration of dissolved impurity atoms is higher than the equilibrium monomer concentration of these precipitates[2]. A competitive coarsening process (OSTWALD ripening) starts after the concentration of dissolved impurity atoms has decreased. Large nanoclusters grow on the expense on the smaller one, which may finally dissolve.

---

[1] At high enough temperature the phase separation occurs already during the ion implantation which is not considered here.

[2] Which is usually much higher than the equilibrium concentration of monomers at a flat interface (solidus concentration).

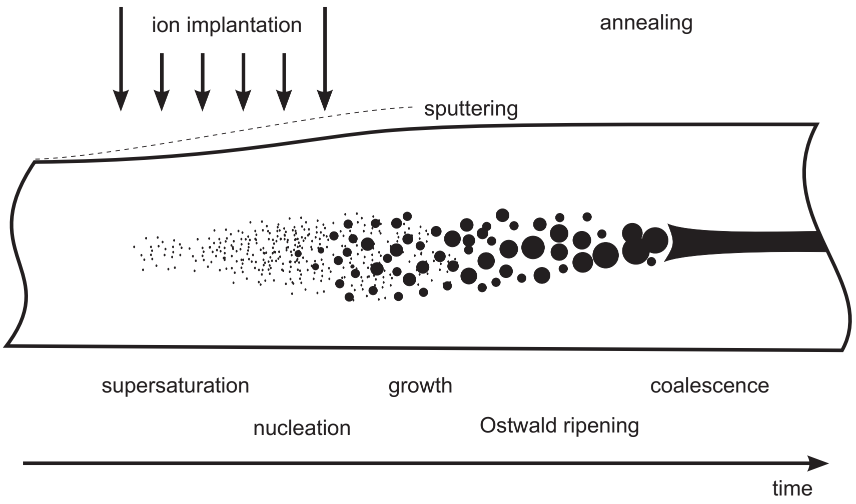

Figure 4.1: Major stages during IBS of precipitates from an initial supersaturation for a system where swelling exceeds sputtering.

coalescence: At very high fluences, neighboring nanoclusters can touch each other and start to merge. Large structures are achieved by the coalescence of many nanoclusters if the nanocluster density exceeds the percolation threshold.

Despite this clear classification a distinct onset of the different stages is usually not defined. Moreover, the boundaries are floating and depend on the specific ion-substrate system and the implantation parameters. Especially at very high ion fluences the coarsening process could be of second-order and the coalescence may dominate the evolution. Moreover, phase separation can then be given by spinodal decomposition instead of nucleation.

4.1.1 Nucleation

Here, the discussion follows the classical nucleation theory (CNT) developed by Becker, Doering, Zeldovich, Frenkel, Volmer, and Weber, which provides a good understanding of the homogeneous nucleation of nanocrystals formed by IBS. A comprehensive discussion and review is given in [IK97]. The authors also mention internal contradictions of the CNT and presents further developments exceeding the limitations of the CNT.

The initial supersaturation of Ge atoms dispensed in the SiO_2 matrix is metastable and thermal fluctuations may lead to the precipitation of second-phase nanocrystals. In general, the nucleation rate I can be written as

$$I = A \exp\left\{-\frac{W}{k_B T}\right\}, \tag{4.1}$$

where W is the reversible energy needed for the formation of a nucleus from several monomers. The dynamical parameter A describes the rate of nucleation and is proportional to the monomer concentration. Nevertheless, not all nuclei are stable. The Gibbs free energy is increased for small nuclei due to the unfavorable phase

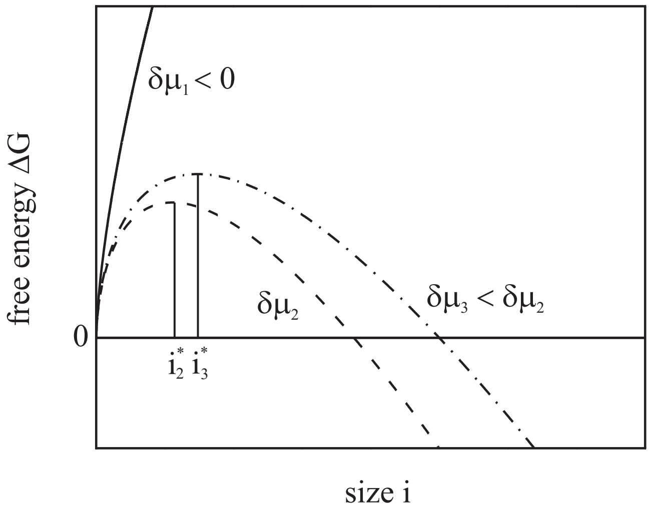

Figure 4.2: The Gibbs free energy is plotted for three different cases ($\delta\mu_1 < 0$, $0 < \delta\mu_3 < \delta\mu_2$) according equation (4.2). For a supersaturated system $\delta\mu > 0$, a nucleation barrier exists and depends on the degree of supersaturation. In the absence of supersaturation $\delta\mu < 0$, precipitates of any size are unstable.

boundary and reduced for large precipitates due to the gained binding energy. The difference in the Gibbs free energy between dissolved atoms and condensed nuclei is given by

$$\triangle G(i) = -\underbrace{(\delta\mu)i}_{\text{bulk}} + \underbrace{\gamma i^{2/3}}_{\text{surface}}, \tag{4.2}$$

where i denotes the number of atoms in a nucleus, see figure 4.2. The parameter γ is proportional to the surface tension σ. The chemical potential of an ideal solution is given by $\mu = k_B T \ln c + \phi$ with a remaining ϕ independent of c. Thus the supersaturation is

$$\delta\mu = \mu - \mu_{eq} = k_B T \ln\left(\frac{c}{c_{eq}}\right), \tag{4.3}$$

with the equilibrium concentration $c_{eq} = c_{eq}(T)$ at a flat phase boundary (solidus concentration). The difference in the Gibbs free energy splits into two contributions. The first part contains the gained binding energy as a result of the nucleation from unbound monomers, which is labeled as bulk contribution in equation (4.2). Please note the negative sign. The second contribution is a surface effect. Atoms on the surface of the precipitate are not fully coordinated and thus are less bound than atoms in the volume of a nuclei.

For $\delta\mu > 0$ the change in the Gibbs free energy $\triangle G(i^*)$ exhibits a maximum for a critical cluster size i^*, which corresponds to a critical radius for spherical nuclei.

$$i^* = \left(\frac{2\gamma}{3\,\delta\mu}\right)^3 \qquad \Longrightarrow \qquad r^* = \frac{\gamma}{\delta\mu}\sqrt[3]{\frac{2V_A}{9\pi}} \tag{4.4}$$

The atomic volume is here denoted by V_A.

Precipitates with $i > i^*$ can lower their Gibbs free energy by an attachment of monomers and are dynamically stable $\left(\frac{d\triangle G}{di} < 0 \text{ but } \triangle G > 0\right)$. During the further monomer attachment they become also energetically stable $\left(\frac{d\triangle G}{di} < 0 \text{ and } \triangle G < 0\right)$. Consequently, the nucleation energy barrier W in equation (4.1) could be identified with $W = \triangle G(i^*)$ for homogenous nucleation. This barrier decreases with increasing supersaturation and temperature. Finally, for a vanishing nucleation threshold one can no longer speak about nucleation as the dominating mechanism of phase separation. The spinodal decomposition has to be considered instead. Nevertheless, it is assumed here that nucleation happens even for very high ion fluences.

Additionally to homogeneous nucleation, the pase separation can be triggered by inhomogeneities. Defects, grain boundaries, or impurities can stabilize small nuclei and therefore lower locally the nucleation barrier.

Nevertheless, the nucleation behavior of a localized supersaturation remains a complex problem even under homogenous nucleation. The nucleation rate depends in a nonlinear manner on the local supersaturation and only qualitative results can be summarized.

- The homogeneous nucleation is thermally activated, a nucleation barrier W exists.
- A threshold size i^* for stable cluster exists and is temperature dependent. The threshold size i^* decreases with increasing supersaturation and with increasing temperature.

Applied to the nanowire growth this reveals that nucleation will start at the location of the center of the later nanowire. The supersaturation has its highest value there and, thus, the critical nuclei size is very small. This also assures a very even material distribution along the later wire center since the precipitate density has to be very high if their size is small. On the other hand, the nucleation probability is lower on the outskirts of the forming wire due to a lower supersaturation. Rather, the monomers may condense onto the formed nuclei in the center.

4.1.2 Growth and Coarsening

A single second-phase precipitate nucleated from an initial supersaturation interacts with the initial phase by monomer exchange. Thereby, the equilibrium concentration of monomers near the phase boundary is reached if the attachment and detachment rates are balanced, which is also a function of the local curvature of the phase boundary. For spherical precipitates this relation is given for the diffusion controlled case by the Gibbs-Thomson (GT) relation [LL79, GR81], which is also known as Kelvin relation

$$c^{GT}(R) = c_\infty \exp\left(\frac{R_c}{R}\right), \qquad R_c = \frac{2\sigma V_a}{k_B T}. \tag{4.5}$$

Here, c_∞ denotes the impurity equilibrium concentration at a flat phase boundary (i.e. the solidus concentration), and the capillary length R_c is given by the material parameters surface tension σ and atomic volume V_a. The precipitate will grow if

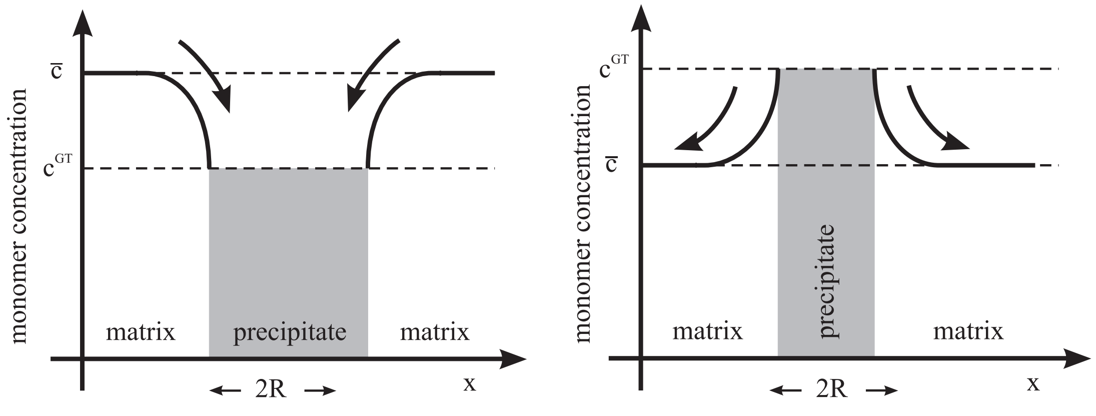

(a) growing precipitate, $\bar{c} > c^{GT}$

(b) shrinking precipitate, $\bar{c} < c^{GT}$

Figure 4.3: Sketch of the concentration profile of dissolved monomers near a precipitate. The equilibrium concentration c^{GT} is given by the GIBBS-THOMSON relation, equation (4.5). Depending on the average monomer concentration $\bar{c}$ the cluster grows (a) or shrinks (b).

the average surrounding concentration is higher than c^{GT}, the cluster acts as a sink for the diffusing monomers leading to cluster growth. On the opposite, for a lower average concentration of surrounding monomers compared to c^{GT} the cluster emits monomers and therefore acts as a source and will shrink, see figure 4.3.

In an early growth stage after nucleation all clusters will grow feeded from the reservoir of dissolved monomers. At that stage the average monomer concentration is still large compared to the equilibrium concentration c_{GT} of the individual clusters. The clusters do not interact directly with each others and the total volume of the precipitated second-phase increases in time at a constant rate.

However, when supersaturation becomes insufficient to dominate the system evolution, the system tends to diminish its free energy via a decrease of the total interfacial area. This minimization occurs by diffusional mass transfer from smaller (dissolving) to larger (growing) precipitates, which results in an increasing average precipitate size but decreasing total surface area. This stage of the first-order phase transition is also known as OSTWALD ripening [Ost97] or coarsening.

The theory of OSTWALD ripening in spatially uniform infinite and diluted systems was developed by Lifschitz, Slyozov [LS61] and Wagner [Wag61] (LSW-Theory). Although it has been continually improved, it is a mean field theory and lacks the applicability to realistic systems without uniformity. Especially, the coarsening of finite-size or layered systems as achieved by IBS could lead to self-organization effects not encountered in the uniform case [BHR97].

Further, the restriction to a vanishing volume fraction of the second-phase precipitates could be released. Typical system in IBS have volume fraction of the impurity phase of several percent. In this case, nanoclusters are not embedded independently in an uniform background of dissolved monomers. Rather, the precipitates interact directly via monomer diffusion and the local monomer concentration is a function of

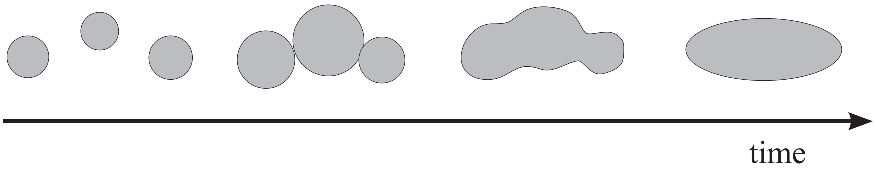

Figure 4.4: Sketch of the coalescence of neighboring nanoclusters during their growth.

the cluster size and their spatial distribution. A local mean-field approach integrates the diffusional interaction [Rei96, RH96, Str99] and gives also access to a description of coarsening in finite-size systems.

4.1.3 Coalescence

In systems with very high precipitate density neighboring clusters may touch each other and start to merge. This process of coalescence becomes dominating if a critical nanocluster density is exceeded, the percolation threshold. This threshold can also be related to the initial supersaturation since the number of nuclei grows with increasing supersaturation. Isolated nanoclusters evolves to a connected structure with an infinite path trough the second phase subsystem. In general, coalescence can be regarded as a second-order phase transition from spatially isolated clusters to one infinite systems [PB99]. The transition takes place at the percolation threshold. The shape of this infinite object is defined by the the morphology of the region, where the percolation threshold was exceeded. So if the Ge profile achieved by ion implantation exceeds in its center the percolation threshold a nanowire will be formed. Thus the main task is to obtain the suitable Ge concentration profile, where along a line the concentration is just above the unknown threshold.

However, this is only a static description of the coalescence taking place during the nanowire growth. Ostwald ripening may lead to an monomer current into the profile center and therefore increase the total Ge concentration in the wire center in time. The percolation threshold is not exceeded in the beginning of the growth but is overcome later and a continuous wire is formed (see figure 4.7). On the contrary, Ge monomers can be lost by diffusion into the matrix at very high temperatures. Although the threshold was exceeded in the beginning the wire may dissolve due to this loss of Ge in time.

Consequently, a combined dynamical treatment is necessary to access the complex interplay between all growth stages, nucleation, growth, coarsening, and coalescence. A unified analytical treatment is hardly possible and computational methods are more promising.

4.2 Kinetic 3D Lattice Monte Carlo Simulation

For a joint treatment of nucleation, growth and coalescence a more ingenious approach is needed to obtain a quantitative understanding for the complex phase separation. On an atomic scale two simulation methods are commonly used, Molecular

Dynamics and Monte Carlo (MC) techniques. However, for processes with many degrees of freedom as the aimed nanowire growth MC methods prove to be more efficient, since exact computations of physical observables are highly impractical. The tool of statistical mechanics provides a more adequate approach to such systems. Not the complete deterministic description of the time evolution of all microscopic variables is needed, but a probabilistic approach to find the most likely evolution of the system. To find a thorough discussion of Monte Carlo methods in statistical physics see [NB99, BH92].

In general, all macroscopic observables A are statistical averages and not the true value $A(\mathbf{x})$ for a particular state $\mathbf{x}$ is observed. This average can be computed in the classical canonical framework with the knowledge of the particular partition function Z and the hamiltonian $\mathcal{H}$

$$\langle A \rangle = \frac{1}{Z} \int d\mathbf{x} \exp[-\mathcal{H}(\mathbf{x})\beta]\, A(\mathbf{x}) \quad \text{with} \quad \beta = (k_B\, T)^{-1}\,. \tag{4.6}$$

The integration extends here over all possible states $\mathbf{x}$ of the system and the partition function is defined as

$$Z = \int d\mathbf{x} \exp[-\mathcal{H}(\mathbf{x})\,\beta], \tag{4.7}$$

which implies a volume V, constant number N and temperature T. The related thermodynamic potential is the free energy F given by

$$F = U - TS = -k_B T\, lnZ. \tag{4.8}$$

The probability to find the system in the state $\mathbf{x}$ is given by the normalized Boltzmann factor

$$p(\mathbf{x}) = \frac{1}{Z} \exp[-\mathcal{H}(\mathbf{x})\beta]. \tag{4.9}$$

Despite the accurate statistical description, the partition function Z is hardly obtainable this way, because of the high dimensionality of the involved integration. Instead, numerical models have to be used to approximate equation (4.6). In a Monte Carlo approach a sample is drawn at random from all possible microstates and the macroscopic variable $< A >$ is approximately computed by

$$\langle A \rangle = \frac{\sum_{l=1}^{M} e^{-\mathcal{H}(\mathbf{x}_l)\beta} A(\mathbf{x}_l)}{\sum_{l=1}^{M} e^{-\mathcal{H}(\mathbf{x}_l)\beta}}. \tag{4.10}$$

Unfortunately, there are much more unlikely state then likely ones. The likelihood of a state is expressed by the Boltmann factor $\exp[-\mathcal{H}(\mathbf{x})\beta]$ and thus the unlikely states contribute less to the average $< A >$. So a random sample over a finite set of microstates would only lead to very rough estimate of the true average $< A >$.

A more natural way of sampling is to choose a state with a probability of $P(x) \sim \exp[-\mathcal{H}(\mathbf{x})\beta]$, which is called importance sampling. Then the Boltzmann factor cancels out altogether, and equation (4.10) reduces to a simple arithmetic average

$$\langle A \rangle = \frac{1}{M} \sum_{l=1}^{M} A(\mathbf{x}_l). \tag{4.11}$$

Metropolis et. al. [MRR+53] advanced the idea not to choose the states $\mathbf{x}_l$ independently from each other, but to construct a Markov process where each state $\mathbf{x_{l+1}}$ is generated from its previous state $\mathbf{x}_l$ via a suitable transition probability $W(\mathbf{x}_l \rightarrow \mathbf{x}_{l+1})$. With the appropriate choice of this transition probability, the probability distribution of the generated states tends towards the equilibrium distribution, equation (4.9). A sufficient condition to achieve this is to impose the principle of detailed balance

$$P_{eq}(\mathbf{x}_l) W(\mathbf{x}_l \rightarrow \mathbf{x}'_l) = P_{eq}(\mathbf{x}'_l) W(\mathbf{x}'_l \rightarrow \mathbf{x}_l). \tag{4.12}$$

Equation (4.12) implies that the ratio of the transition probabilities depends only on the energy change $\delta\mathcal{H} = \mathcal{H}(\mathbf{x}'_l) - \mathcal{H}(\mathbf{x}_l)$,

$$\frac{W(\mathbf{x}_l \rightarrow \mathbf{x}'_l)}{W(\mathbf{x}'_l \rightarrow \mathbf{x}_l)} = \exp\left(-\delta\mathcal{H}\,\beta\right). \tag{4.13}$$

One possible choice is

$$W(\mathbf{x}_l \rightarrow \mathbf{x}'_l) = \begin{cases} \frac{1}{\tau}\exp(-\delta\mathcal{H}\,\beta) & \text{if } \delta\mathcal{H} > 0, \\ \frac{1}{\tau} & \text{else,} \end{cases} \tag{4.14}$$

whereas only the ratio between both transition probabilities has to be guaranteed. Thus, the arbitrary factor τ is free for the moment and can be adjusted to one.

4.2.1 Lattice Gas

Despite of the pure thermodynamical considerations the choice of the underlying simulation lattice determines the properties of the model. The given lattice allows a more convenient simulation as a true continuum picture. In the used lattice model the positions of all impurity atoms are restricted to a 3D periodic lattice. Further, the host matrix for second phase atoms is considered to be chemically inert, it is regarded as the simulation background.

The kinetics of atoms in the matrix is then simulated by jumps from occupied sites to empty ones. No atom is allowed to reside in a position between two lattice sites, even if the diffusion in an amorphous matrix is discussed. This restriction is satisfied as long as the lattice spacing is small and the diffusion remains isotropic, which is assured by the correct transition probabilities[3].

For a particular simulation the resulting crystallographic structure of the nanocrystals under investigation is determined by the specific type of lattice used within the Monte Carlo code. For the results presented in this work the face-centered cubic (fcc) lattice has been chosen for several, partially historical, reasons:

- the fcc structure is one of the most isotropic lattices and thus probably best suited to describe precipitation in amorphous host matrices (e.g. SiO_2);

---

[3] The actual physical background of the diffusional jump in an disordered material is not of interest here.

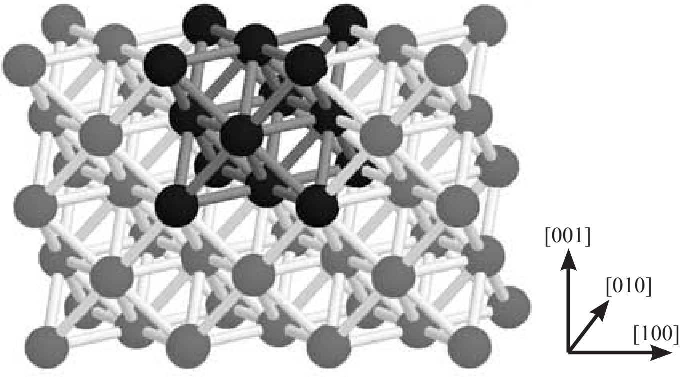

Figure 4.5: Face centered cubic (fcc) lattice. The unit cell is displayed colored (darker).

- the diamond lattice of Si or Ge is composed of two fcc sublattices shifted by $(\frac{1}{4}a, \frac{1}{4}a, \frac{1}{4}a)$;
- the basics of the used numerical code was first laid for the fcc Co subsystem in $CoSi_2$ and later extended to Ge or Si [Hei95].

Since the thermodynamical system is fully defined by the occupation of each site, the system reveals a strong analogy to a system of Ising spins. Only two states are possible at one lattice site, occupied and empty.
On the other hand, a given simulation lattice also determines the crystal orientation of the growing nanocrystals. Consequently, the obey the same orientation and lattice constant. The growth of competing grains with different orientations in a polycrystalline material is not treatable in this single-grid model. An approach to the simulation of the nanowire growth would always provide single crystalline nanowires, which is not realistic. Rather, polycrystalline wires are expected. This contradiction is lifted in section 4.3.2.

4.2.2 Energetics and Jump Probability

The hamiltonian $\mathcal{H}(\mathbf{x})$ within the Boltzmann factor (4.9) is note yet specified for our purpose. In a first approach the analogy to the Ising spin model can be stressed further. Only nearest neighbor interactions are included and the energy of all bonds is summed over the whole lattice. This implies the adiabatic limit where the electronic subsystem remains in the ground state and reacts instantaneously on the change of nuclei positions. Electronic excitations are excluded. Under these assumptions the Ising hamiltonian reads as

$$\mathcal{H}(\mathbf{x}) = -J \sum_{\langle ij \rangle_{nn}} C_i C_j. \tag{4.15}$$

Here, C_i denotes the occupation state of the site i (C_i=1 for an occupied or C_i=0 for an unoccupied site). The sum is taken over all nearest-neighbor pairs. The gain of energy obtained by a nearest-neighbor bond is given by J, which is related to the

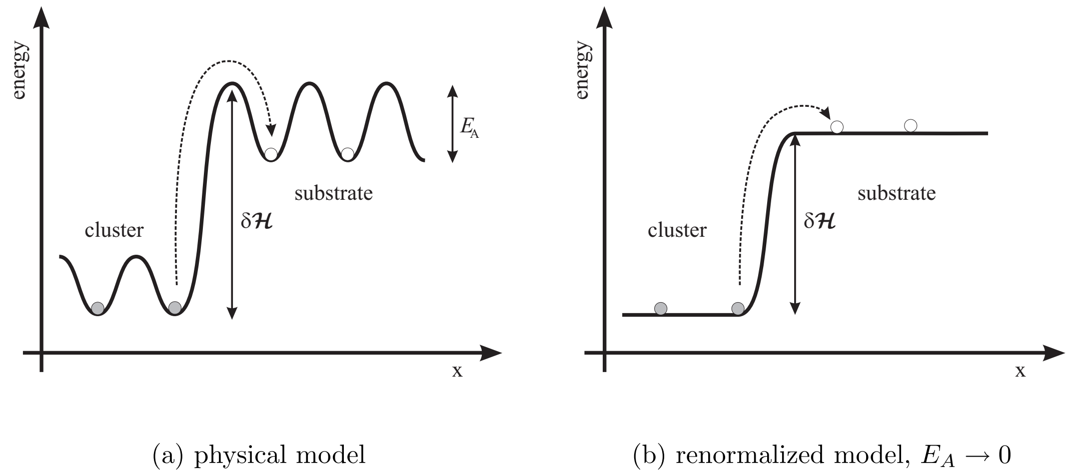

(a) physical model (b) renormalized model, $E_A \to 0$

Figure 4.6: Energetics of the simulation model. Averaged potential for an impurity atom, where the energy barrier E_A governs the diffusion and the energy $\delta\mathcal{H}$ the monomer detachment from a cluster in the schematic physical model (a). For the simulation the model is renormalized (b) to $E_A \to 0$.

sublimation energy $E_b = (12/2)J$ for the fcc lattice. Thus the energy gain $\delta\mathcal{H}$ for a jump from the initial site to the final site is determined within the Ising model by

$$\delta\mathcal{H} = -(n_f - n_i)J = \frac{1}{6}(n_i - n_f)E_b. \tag{4.16}$$

The coefficients n_i, n_f denote the number of nearest neighbors in the initial and final state, respectively. In figure 4.6 a schematic picture of the energy landscape for an impurity atom within the Ising model is shown.

Also the diffusion of monomers in the host matrix is thermally activated and the experimentally measured diffusion coefficient obeys the relation

$$D_{exp} = D_0 \exp\{-E_A\beta\}, \tag{4.17}$$

where E_A denotes the activation energy for diffusion. Thus, the hamiltonian contains an additional diffusion barrier E_A

$$\delta\mathcal{H} = -(n_f - n_i)J + E_A. \tag{4.18}$$

In difference to the reversible binding energy this contribution is irreversible and has to be paid for every nearest neighbor jump of an impurity atom within the matrix. Only one activation energy for the diffusion is assumed.

Having specified the hamiltonian one can write the transition probability for one atom from the initial i to the final site f as

$$W_{i\to f} = \begin{cases} \frac{1}{\tau}\exp(-\beta[E_A + (n_i - n_f)J]) & n_f < n_i, \\ \frac{1}{\tau}\exp(-\beta E_A) & n_f \geq n_i, \end{cases} \tag{4.19}$$

where τ^{-1} denotes the attempt frequency for atomic jumps, and $n_{i,f}$ is the number of nearest neighbors in the initial (final) position. The transition with the highest probability is the diffusional jump of an impurity atom, which gives rise to a diffusion coefficient of

$$D = \frac{a_l^2}{\xi}\frac{1}{\tau_0}\exp\{-E_A\beta\} \tag{4.20}$$

Here, ξ denotes the coordination number of the used lattice ($\xi = 12$ for the fcc lattice) and a_l is the lattice constant.

As already mentioned, it is convenient to allow every diffusion attempt, since only the ratio of the transition probabilities in equation (4.19) has to be maintained. Scaling the transition probability with $\tilde{W}_{i\to f} = W_{i\to f}/(\tau^{-1}\exp\{-E_A\beta\})$ renormalizes just the time scale of the model but enhances the simulation speed. Defining further a reduced energy $\epsilon = J\beta$ leads to

$$W_{i\to f} = \begin{cases} \exp\{-(n_i - n_f)\epsilon\} & n_f < n_i, \\ 1 & n_f \geq n_i, \end{cases} \tag{4.21}$$

The transition of an atom is allowed if the atom has more neighbors in its final position than in the initial one. In the opposite case the transition is still allowed at a small probability $W_{i\to f} = \exp\{-(n_i - n_f)\epsilon\}$.

4.2.3 Metropolis Algorithm and Dynamic Importance Sampling

The fundamental difficulty which makes out-of-equilibrium simulations harder than the equilibrium counterparts is that the correct dynamics has to be chosen. It is no longer sufficient that the chosen dynamics leads in their implementation to the equilibrium distribution. Also the way towards the thermodynamical equilibrium is important. Therefore, the METROPOLIS algorithm [MRR+53] is introduced using the scaled transition probability $W_{i\to f}$ from equation (4.21). This implementation corresponds as far as possible to a realistic model of the evolution to the equilibrium by jumps of single atoms. Other equilibrium MC algorithms can not be applied.

Now the sequence of states generated by the METROPOLIS algorithm with the transition probability $W_{i\to f}$ is associated with a time scale. This scale has already been normalized such that each single diffusional jump is performed in unit time, which is called Monte Carlo step (MCS). To be more precise, during a MCS each atom in the simulation lattice either performes a diffusional jump or attempts to jump into an energetically unfavored position with the transition probability $W_{i\to f}$.

The algorithm itself consists of a simple loop which is repeated N times per MCS, where N is the number of atoms.

- Choose an impurity atom at random
- Choose a neighboring site at random (there are 12 neighbors in the fcc lattice)
- Stop if the neighbor site is occupied

- Calculate the transition probability $W_{i\to f}$ according to equation (4.21)
- Draw a random number uniformly distributed in $(0,1)$
- Jump if this number is smaller than $W_{i\to f}$

This choice of the algorithm ensures that [NB99]:

1. The ensemble of atoms relaxes to the thermodynamical equilibrium for an infinite number of MCS.
2. The system is ergodic as long as the interaction Hamiltonian $\mathcal{H}$ is finite[4]. Thus every atom can in principle reach every lattice site.
3. The dynamics are chosen close to the physical model of diffusion such that the way towards equilibrium is meaningful.

Since the transition probability has been renormalized, the physical time which corresponds to a MCS is temperature dependent. The diffusion coefficient D_{sim} in the scaled model is then given by

$$D_{sim} = \frac{D}{\tau^{-1}\exp\{-E_A\beta\}} = \frac{a_l^2}{\xi}. \tag{4.22}$$

Further, since the diffusion length should be equal

$$l_{diff} = \sqrt{2Dt_{MCS}} = \sqrt{2D_{sim}} \tag{4.23}$$

one can determine the time interval corresponding to a MCS

$$t_{MC} = \frac{D_{sim}}{D} = \frac{a_l^2}{\xi}\Big(D_0\exp\{-E_A\beta\}\Big)^{-1}. \tag{4.24}$$

Thus, the unit time in the simulation may vary by orders of magnitude at varying temperature.
The Metropolis algorithm has been implemented in Fortran. It was originally coded by Heinig [Hei95] and extended by Strobel on workstations [SHM98, Str99]. Nevertheless, all simulations performed for this thesis were carried out with an optimized code on modern personal computers. Typical simulation times range from 24 hours up to one week for large scale systems.

4.3 Simulation of the Nanowire Growth

KLMC simulations may provide a more solid understanding of phase separation phenomena since they can serve as a unique tool to check ideas in an clean environment without any conflicting side effects. Applied to the nanowire growth additional knowledge about influencing parameters is gained without immense experimental effort. Selected examples of KLMC simulations reveal a complex growth behavior of the nanowire from the initial Ge distribution. In order to keep simulation time below one week the size of the simulation system is smaller than the experimental system.

---

[4] The problem of ergodicity is not discussed here since it is of second order for the simulation of the nanowire.

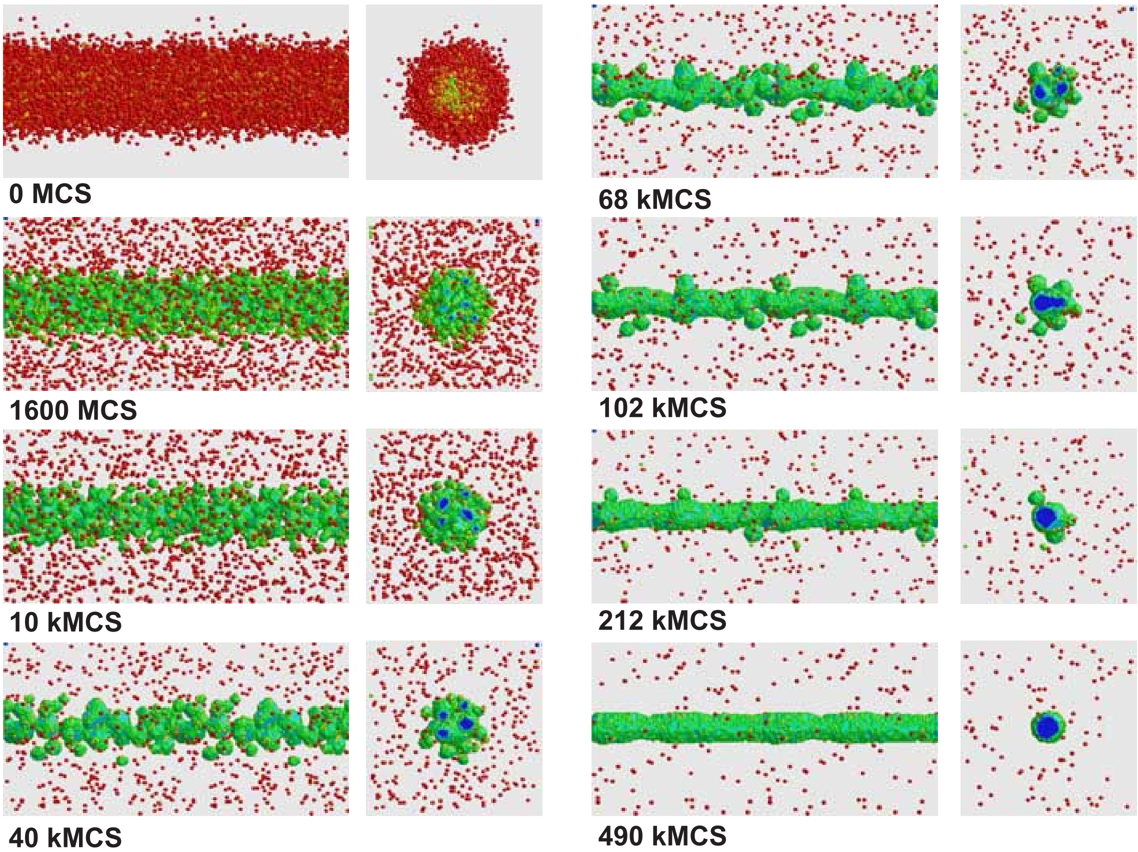

Figure 4.7: KLMC simulation of the nanowire formation from an initially cylindrical Gaussian profile (denoted by 0 MCS) with a peak concentration of 31% and a standard deviation of 3.5 nm. Shown are plane views and cross sections of intermediate stages during the simulation of the nanowire growth. After 490 kMCS a wire of 5.3 nm diameter has formed.

4.3.1 Cylindrical Gaussian Profile

Ge is implanted into oxidized Si V-grooves and comes to rest within the oxide layer close to the surface. Additionally SiO_2 and Ge is sputtered by energetic incident ions and subsequently redeposited onto the opposite V-groove sidewall. As pointed out in chapter 3.3, sputtering and redeposition leads to Ge enrichment in the V-groove bottom. The resulting spatial distribution of Ge atoms embedded in the SiO_2 is experimentally confirmed by STEM-EDX mapping on as-implanted samples, see figure 3.8.

Although the initial Ge distribution caused by ion implantation is known, it is reasonable to choose a simplified initial Ge distribution for the KLMC simulations. This allows to distinguish between inherent thermal effects and effects determined by external conditions, e.g. induced by the initial Ge distribution. Hence, consider a cylindrical Gaussian distribution of Ge atoms in the V-groove bottom, which exhibits the highest possible symmetry. Consequently, this initial distribution could serve as a model distribution to identify a lower boundary of the wire diameter achievable

by this growth method.
This simplification neglects the Ge implanted in the V-groove sidewalls. Only Ge in the V-groove bottom contribute to the wire growth, which is reasonable due to the low Ge content in the V-groove sidewalls and the long distance to the wire center. Ge atoms far away from the V-groove bottom contribute less to the nanowire growth.
Figures 4.7, 4.8, and 4.9 show a sequence of independent KLMC simulations of the nanowire synthesis from an initially cylindrical Gaussian profile. According to this distribution 18000 Ge atoms were placed in the simulation lattice of $(L \times L \times L = 128 \times 128 \times 128)$ lattice points with a grid spacing of $(a_l/2)$. This corresponds to a box of 36 nm length[5]. The distribution was aligned to the [100] direction (the x-axis) of the fcc lattice, which determines the wire orientation. A possible compact nanowire will then have approximately a diameter given by

$$d_{wire} = a_l \sqrt{\frac{2N}{L\pi}} = 0.565\ \text{nm} \times \sqrt{\frac{36000}{128\pi}} = 5.3\ \text{nm}, \tag{4.25}$$

if no material is lost. Thereby a_l denotes the Ge lattice constant.
During the KLMC simulation, periodic boundary conditions were applied in all three spatial directions. This periodicity was used for the visualization and the simulation cell is displayed doubled in the x-direction in figure 4.7, 4.8, and 4.9. The color scale was chosen to show the coordination state of each Ge atoms (from fully coordinated (blue) to isolated (red) atoms). The simulation temperature was chosen to be comparably high $\epsilon = \beta J = 1.6$.
The only difference between the above KLMC simulations is the selected standard deviation σ_0 of the initial Ge distribution. At constant particle number $(N = 18000)$ this also determines the maximum Ge concentration (peak concentration) in the distribution.

Simulation	$\boldsymbol{\sigma_0}$	**Peak concentration**	**Wire formed?**
figure 4.7	3.5 nm	31%	Yes
figure 4.8	4.3 nm	20%	No
figure 4.9	5.7 nm	11%	No

A continuous wire was achieved only for the KLMC simulation with the narrowest initial Ge distribution ($\sigma_0 = 3.5$ nm), shown in figure 4.7. Due to the high Ge concentration (31%) in the center of the Ge profile the Ge nanoclusters have coalesced early and formed a thin continuous wire. Then Ge literally condenses onto this seed leading to the an continuous Ge nanowire with uniform diameter, which is also expressed by a fast reduction of Ge profile width in time. This width is measured again by the standard deviation σ from the wire axis

$$\sigma = \sqrt{\frac{1}{2N} \sum \left((y_i - \bar{y})^2 + (z_i - \bar{z})^2 \right)}, \tag{4.26}$$

---

[5] Only the half of the vertices have a physical meaning in the fcc lattice. Hence, a site belongs to the fcc lattice if the sum of the coordinates $(x + y + z)$ is even. The total number of accessible site is then $\frac{1}{2}(128 \times 128 \times 128)$.

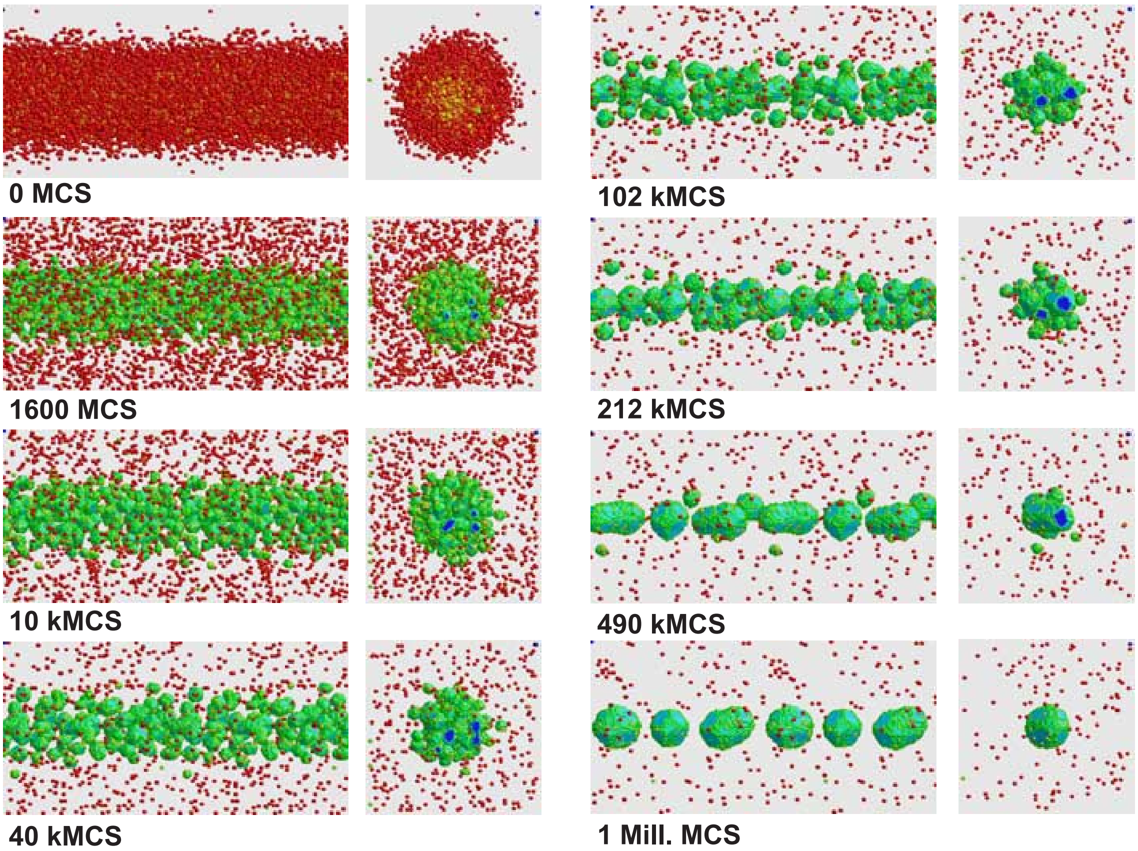

Figure 4.8: KLMC simulation of the nanowire formation from an initially cylindrical Gaussian profile (denoted by 0 MCS) with a peak concentration of 20% and a standard deviation of 4.27 nm. Shown are plane views and cross sections of intermediate stages during the simulation of the nanowire growth.

which is plotted in figure 4.10 as a function of time. The broadness measured by σ decreases quickly for the lower curve ($\sigma_0 = 3.45$ nm) in figure 4.10 compared to the other. Ge condenses quickly onto the wire center and the standard deviation σ approaches a constant value for large times ($\sigma \to \sigma_{min}$) given by σ_{wire}, shown as dashed line. This value is determined by the moment of inertia of a solid cylinder (wire) with radius r_{wire}.

$$J = \frac{1}{2} M r_{wire}^2 = 2 M \sigma_{min}^2 \qquad \Longrightarrow \qquad \sigma_{min} = \frac{r_{wire}}{2} = \frac{d_{wire}}{4} = 1.4\,\text{nm} \tag{4.27}$$

Hence, it is essential for the synthesis of a continuous wire that the dispensed Ge condenses radially as fast as possible onto the wire center. At the same time any significant material transport along the wire axis has to be prohibited. Otherwise a set of large cluster is formed instead of a continuous wire, see as an example figure 4.8 and 4.9.

The critical stage is the competitive growth (Ostwald ripening) of neighboring clusters after nucleation and initial growth. In general, one can distinguish between two branches. First the radial Ostwald ripening, where larger clusters in the

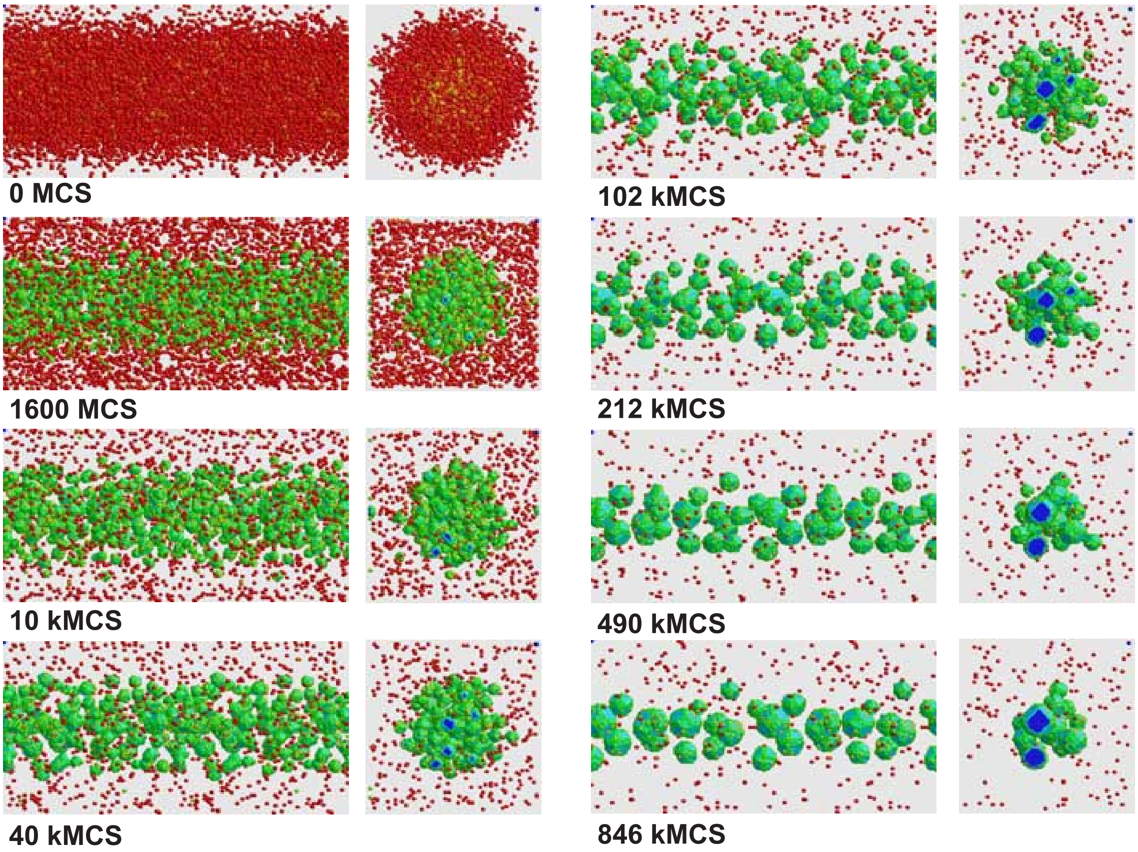

Figure 4.9: KLMC simulation of the nanowire formation from an initially cylindrical Gaussian profile (denoted by 0 MCS) with a peak concentration of 11% and a standard deviation of 5.7 nm. Shown are plane views and cross sections of intermediate stages during the simulation of the nanowire growth.

center of the later wire compete with smaller ones on the outskirts, which finally get dissolved. This desirable evolution leads to the coalescence of nanoclusters in the wire center which form the continuous nanowire. On the other hand, Ostwald ripening can also occur laterally along the wire axis. Small fluctuations in the lateral Ge density are amplified and the coalescence to a continuous nanowire with even diameter is hindered as it happened for the simulations shown in figure 4.8, and 4.9. In general, Ostwald ripening takes place in all directions (radially and laterally). In order to get a continuous nanowire it is important to reduce the lateral Ostwald ripening while maintaining the radial one. This was achieved for the narrowest initial Ge distribution shown in the first KLMC simulation (4.7). There hasn't been sufficient time in that case for a lateral Ge redistribution along the wire axis.

Additionally, coalescence plays an important role for the nanowire growth although it hasn't been systematically investigated here. The growth mechanisms are expected to change drastically if the initial Ge concentration exceeds the percolation threshold. Ostwald ripening is no longer the dominating growth mechanism but it is necessary to achieve a smooth nanowire without surrounding precipitates. Nevertheless coalescence, the direct fusion of neighboring nanoclusters, will dominate

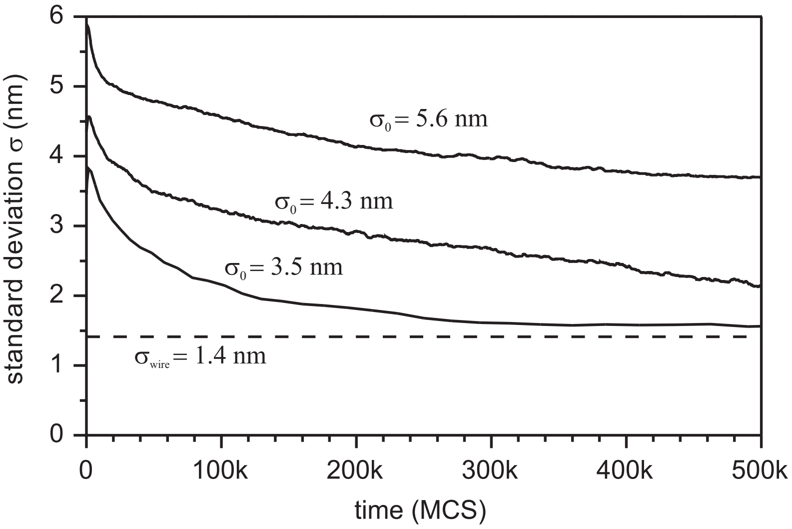

Figure 4.10: Standard deviation of the Ge distribution from the wire axis for different initial values of σ. Thereby, $\sigma_{wire} = 1.4$ nm indicates the lowest possible value of σ which is assumed for a continuous wire of 5.3 nm diameter.

the evolution the cluster ensemble. Unfortunately, the percolation threshold as a characteristic material parameter is unknown for the present system.

Only the cylindrically symmetrical initial distributions of Ge atoms have been looked at. However, the experiments show an asymmetric Ge distribution in the V-groove bottom, which has to be integrated into further KLMC simulations. Closely related is also the choice of appropriate boundary conditions for the simulation. One has to account for the curved SiO_2 surface at the V-groove bottom, which acts as a reflecting boundary for diffusing Ge atoms within the oxide[6]. On the contrary the SiO_2/Si interface absorbs Ge and therefore acts as a sink, since Ge is miscible in Si.

4.3.2 Polycrystalline vs. Single Crystalline Nanowires

The KLMC simulation of the nanowire growth involves always a predefined lattice (here the fcc). Hence, the precipitation of impurity atoms leads to equally oriented nanoclusters. A competitive growth of grains with different orientations in the coalescence stage is not covered in the present simulation approach. Multi-grid models or grids with much finer spacing should be used instead, but haven't been available yet. Consequently , the growing nanowire will be single crystalline as a result of the given fcc simulation lattice, see therefore figure 4.7.

Nevertheless, a nanowire experimentally synthesized in an amorphous matrix should rather be polycrystalline instead of single crystalline. The wire coalesces from many isolated nanoclusters with random orientation. Thus different grains may compete in their growth within the nanowire, but will not lead to a complete single crystalline wire.

---

[6] Excluding material loss by Ge diffusion trough the SiO_2 surface

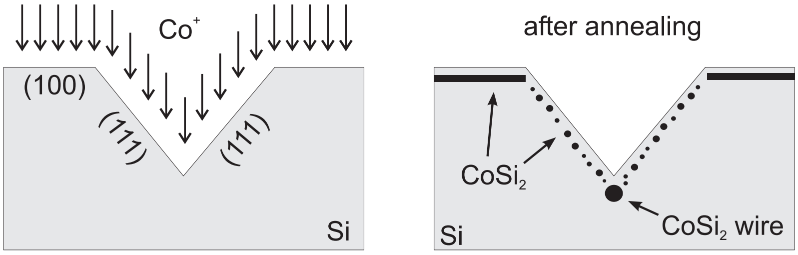

Figure 4.11: Sketch of the synthesis of a single crystalline $CoSi_2$ nanowire by Co implantation in Si V-grooves.

The situation becomes different if the matrix itself is crystalline. As an example, consider Co implantation directly into Si V-grooves. See the sketch in figure 4.11. During subsequent annealing, Co will precipitate coherently in the Si matrix as $CoSi_2$ which means that the $CoSi_2$ clusters obey exactly the same crystallographic orientation as the Si lattice. Consequently, a nanowire synthesized by Co implantation in Si should by single crystalline.

Chapter 5

Wire Stability

In the last chapter, the growth of nanowires from a supersaturated solid solution was discussed by means of kinetic Monte Carlo simulations. As it was pointed out, wires can be formed if the appropriate parameters are chosen for the maximum impurity concentration and the standard deviation of the impurity distribution. Nevertheless, a wire is energetically metastable and can be fragmented into isolated droplets under a gain of free energy. In this context, two questions will be addressed in this chapter. First, does a nanowire tolerate small fluctuations of its diameter? In other words, is the wire instable against surface depressions or does it relax into its original form? The second point to discuss is the final state of a fragmented wire. Assuming a chain of droplets a relation for their minimal size and spacing will be derived from energy considerations.

5.1 Stability Against Thickness Fluctuations

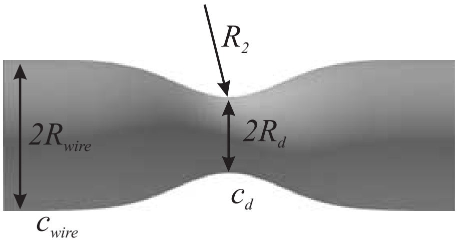

Figure 5.1: Fluctuation in the nanowire radius. The radius of curvature of the unperturbed wire surface is R_{wire}, where at the fluctuation the wire surface has two radii of curvature R_d and R_2

Having synthesized a nanowire of several nanometers width a prominent question concerns the stability of the wire against subsequent thermal treatment. This also includes the question if a wire survives a complete wafer processing as needed for the integration into modern electronic devices. Especially at high temperatures spontaneous thermal fluctuations could become critical. They lead to depressions or bumps at a small scale on the wire surface. An important task is to determine the reaction of a continuous nanowire to such perturbations. Would an external influence lead to a damping or self-amplification with a fragmentation of the wire into several isolated droplets. This discussion of stability focusses here on the dynamical stability, not on the energetic stability, of a wire. From the view of energetics a wire is always metastable.

For the sake of simplicity only a local decrease (fluctuation) in the wire radius is considered, the minimal radius is denoted by R_d and the unperturbed wire radius by R_{wire}. As shown in figure 5.1 this directly leads to a second radius of curvature

(-R_2). Combining both, the surface curvature κ_d at the point of the smallest radius is given by

$$\kappa_d = \frac{1}{R_d} - \frac{1}{R_2}. \tag{5.1}$$

Please note the minus sign in the equation (5.1). In the following the equilibrium concentrations of monomers at the surface of the wire are compared. In the diffusion limited case this concentration is given by the GIBBS-THOMSON (4.5) relation. Further the notion of curvature is introduced in the GIBBS-THOMSON relation. Originally, this equation has been derived for spherical precipitates with a surface curvature of $\kappa_{sphere} = 2/R$ but can be generalized to an arbitrary curvature κ.

$$c = c_\infty \exp\left(\frac{R_c}{R}\right) = c_\infty \exp\left(\frac{R_c}{2}\kappa\right). \tag{5.2}$$

This allows then the calculation of the impurity equilibrium concentration (c_{wire}, c_d) at the phase boundary of the wire, at first for the unperturbed wire and secondly at the point of the smallest wire diameter. The criterion for the stability of the wire against thickness fluctuations is

$$\triangle c = c_{wire} - c_d > 0. \tag{5.3}$$

In this case the depression of the wire surface will be compensated by a monomer flux towards the depression from other areas of the wire. This could happen by detachment of monomers from the wire, 3D diffusion, and attachment to the wire, which is discussed here. But also adatom diffusion on the wire surface and vacancy diffusion within the wire can contribute. The later mechanisms are neglected here in a first approximation treating only the 3D-diffusion with monomer detachment and attachment from and to the wire.[1]

The wire becomes instable if $\triangle c$ gets negative, since then the concentration gradient drives atoms out of the depression. This leads to a self-amplification of the radius fluctuation with fragmentation into separated droplets.

To simplify the following calculation the relative difference of the concentrations is used.

$$\frac{\triangle c}{c_{wire}} = \frac{c_{wire} - c_d}{c_{wire}} = 1 - \frac{c_d}{c_{wire}} \overset{(5.2)}{=} 1 - \frac{c_\infty \exp\left(\frac{R_c}{2}\kappa_d\right)}{c_\infty \exp\left(\frac{R_c}{2}\kappa_{wire}\right)} \tag{5.4}$$

$$= 1 - \exp\left(\frac{R_c}{2}\left(\kappa_d - \kappa_{wire}\right)\right) = 1 - \exp\left(\frac{R_c}{2}\triangle\kappa\right) \tag{5.5}$$

The equation can be written in a linearized form for small values of $\triangle\kappa$ compared to $2/R_c$.

$$\frac{\triangle c}{c_{wire}} = -\frac{R_c}{2}\triangle\kappa = \frac{R_c}{2}(\kappa_{wire} - \kappa_d) > 0. \tag{5.6}$$

Thus, the wire is stable if the curvature of the unperturbed wire κ_{wire} is larger than the curvature at the depression κ_d. A positive capillary length $R_c > 0$ has been

---

[1] In principle the adatom concentration on the wire surface should also obey a GIBBS-THOMSON relation with another capillary length.

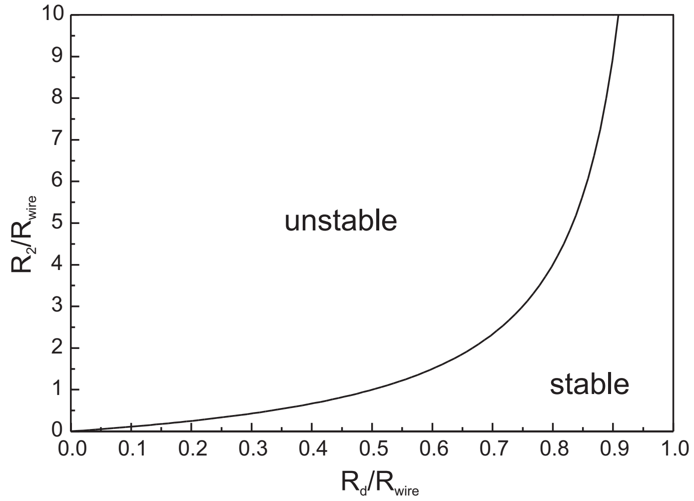

Figure 5.2: Stability of a nanowire with radius R_{wire} against a thickness fluctuation with the two independent radii of curvature R_d, and $(-R_2)$ as shown in figure 5.1. R_d denotes the thinner radius of the wire at the point of the fluctuation and R_2 corresponds to the wire length affected by the fluctuation. Please note the minus sign for R_2.

assumed for this implication, which holds for thermal annealing. Thus, equation (5.6 yields

$$\frac{1}{R_d} - \frac{1}{R_2} = \kappa_d < \kappa_{wire} = \frac{1}{R_{wire}} \tag{5.7}$$

$$\frac{R_{wire}}{R_d} - \frac{R_{wire}}{R_2} < 1. \tag{5.8}$$

The resulting phase diagram for the stability of the nanowire against thickness fluctuations is shown in figure 5.2. The coexistence line between the stable and instable region is determined by the equality in equation (5.8),

$$\frac{R_2}{R_{wire}} = \frac{R_d/R_{wire}}{1 - R_d/R_{wire}}. \tag{5.9}$$

The wire is stable against fluctuations below this curve and instable above. E.g. for a fixed value of R_2 the wire first tolerates its smaller diameter and relaxes to the original shape. On the contrary, the wire becomes instable if the fluctuation has reached a critical amplitude and the wire radius got lower than a critical value. The diffusion will then further increase the depression by an effective material transport outwards. Beyond this point further thermal processing leads directly to a fragmentation of the wire into isolated droplets.

This threshold behavior corresponds to the existence of a fragmentation barrier. A certain amount of energy has to be paid to achieve a fluctuation of a critical size. Beyond this point the system gains energy by fragmentation and, therefore, evolves towards isolated clusters. This also explains the relative instability of very small wires. For them the critical fluctuations have a comparably low energy barrier, which could already be overcome by thermal fluctuations with a great probability. Thus, the wire remains only continuous if thermal fluctuations are reduced due to a lower temperature.

On the contrary to the standard annealing procedure, the annealing can be carried out during a subsequent ion implantation. This ion assisted annealing introduces a new force determining the evolution of the system. The attachment and detachment of monomers is no longer fully determined by thermal processes, but also the ion mixing plays an important role. Other influences of the ion beam can be neglected if the projected range of the implanted ions is large against the depth of the wire buried in the SiO_2. In ion cascades host atoms are randomly displaced over a certain length without any preferential direction. This effect is known as isotropic ion mixing and would lead at zero temperature to a perfect dissolution of the nanowire. At elevated temperatures the situation gets more complex. Attachment mediated by thermal diffusion can level out the effective detachment of monomers by ion recoil cascades. Under such conditions a stationary concentration of impurity atoms at a phase boundary can be reached. It has a form similar to the Gibbs-Thomson relation, equation (4.5), with modified capillary length R_c and monomer concentration at a flat phase boundary c_∞. The complete derivation is described elsewhere [Hei00] introducing the inverse Ostwald ripening. The most prominent difference to the usual Gibbs-Thomson relation is the sign of the capillary length R_c. For a certain ratio of ion flux density to temperature the capillary length becomes negative, $R_c < 0$.

In turn a negative capillary length has dramatic consequences on the stability of the wire during the ion assisted annealing. A negative R_c in equation (5.6) leads to a reversal of the stable and instable regions shown in figure 5.2. The wire is instable even at small fluctuations and will always be fragmented into isolated droplets. This driven instability could be used as a precise tool for wire fragmentation. A remaining open questions is, whether a mode selection takes place during the initial growth of fluctuation on the nanowire surface during ion irradiation. There are some indications that a fastest growing mode exists. As a consequence of such a scenario, fluctuations with a preferred wavelength grow fastest and, finally, after fragmentation a chain of equally spaced droplets with more or less identical diameter could be achieved.

5.2 Fragmentation of a Continuous Wire

As it was pointed out in the last section, a wire can be fragmented under certain conditions into a set of isolated droplets. Nevertheless, the final state is not fully determined. Even under mass conservation, the radius of these droplets remains a free parameter. Generally, the kinetics of the fragmentation process will lead to a certain spacing between these droplets, which in turn determines their radius. Due to the complex nature of the process fragmentation it is not easily describable and the radius of the resulting droplets can not be determined analytically.

On the other side, the wire will decay into a state which is energetically favored compared to the continuous wire. This offers at least the possibility to calculate a

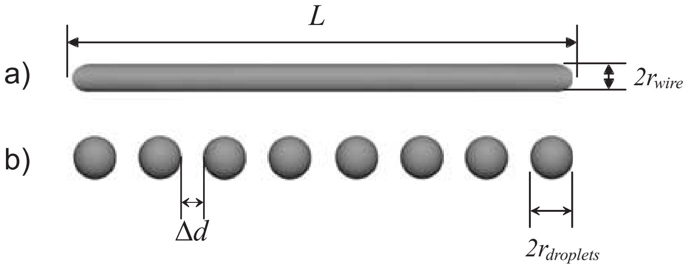

Figure 5.3: Fragmentation of (a) a nanowire with the length L and radius r_{wire} into (b) isolated droplets with equal radius $r_{droplets}$. The spacing between them is $\triangle d$.

threshold for the droplet radius. The main assumption used here is a equal spacing between the droplets $\triangle d$ and an equal diameter of these droplets r_c.

In the further discussion the wire is treated as an open system embedded in a constant volume at a constant temperature. Heat exchange is allowed but particles are confined within the volume. This system is described by the thermodynamical potential, the free energy

$$F = F(V,T) = E - TS. \tag{5.10}$$

During the evolution the free energy F approaches a minimum. Thus, to consider the energetic stability of a nanowire, one has to compare the free energies. A final state is energetically favored if the free energy is lower than the free energy of the initial state. This comparison involves the computation of the internal energy of the system and the entropy in both states.

$$\triangle F = F_{final} - F_{initial} = \triangle E - T\,\triangle S \approx \triangle E \tag{5.11}$$

In the following, the entropy will be neglected and only the internal energy is calculated, which is satisfied for a small change in the entropy ($\triangle S \approx 0$). This also exclude the influence of the temperature on the free energy of the system. Nevertheless, the temperature will always determine the kinetics of the system.

To estimate the internal energy the liquid drop model[2] will be used. Each energy can be written as the sum of a volume contribution E^V and a surface contribution E^S.

$$E = E^V + E^S \qquad \text{with} \quad E^V = -a_V\,N \quad \text{and} \quad E^S = \sigma \oint dS \tag{5.12}$$

Thereby, the volume energy E^V is proportional to the number of bound atoms N in the system. In the limit of an infinite system ($N \rightarrow \infty$) the binding energy is equal to $-a_V$. The surface contribution E^S to the internal energy E of the system is given by the surface area and the surface tension σ.

This allows the calculation of the energy difference between the final state (droplets) and the initial state (wire).

$$\begin{aligned} \triangle E &= E_{droplets} - E_{wire} = \triangle E^V + \triangle E^S && (5.13)\\ &= (E^V_{droplets} - E^V_{wire}) + (E^S_{droplets} - E^S_{wire}). && (5.14) \end{aligned}$$

---

[2] The liquid drop model accounts for the simplest many-body effects in a continuum picture. It has been successfully used in nuclear physics and has led to the famous Bethge formula.

Due to mass conservation $\triangle E^V$ is zero, which simplifies the energy difference

$$\triangle E = \triangle E^S = E^S_{droplets} - E^S_{wire}. \tag{5.15}$$

The initial state is a continuous wire with length L and radius r_{wire}. It will be fragmented and the final state is a chain of $n_{droplets}$ isolated droplets with equal radius $r_{droplets}$ and spacing $\triangle d$. The total volume and the surface area are given by

$$V_{wire} = \pi r^2_{wire} L \qquad A_{wire} = 2\pi r_{wire} L \tag{5.16}$$

$$V_{droplets} = n_{droplets} \frac{4}{3} \pi r^3_{droplets} \qquad A_{droplets} = n_{droplets} 4\pi r^2_{droplets}.$$

Since the volume is conserved during the fragmentation ($V_{wire} = V_{droplets}$) the number of droplets is determined by

$$n_{droplets} = \frac{3}{4} \frac{L r_{wire}}{r^3_{droplets}}. \tag{5.17}$$

Using equation (5.15), (5.16), and (5.17) the internal energy difference per unit length is

$$\frac{\triangle E}{L} = \frac{\sigma}{L} \left(A_{droplets} - A_{wire}\right) \tag{5.18}$$

$$= 2\pi\, \sigma\, r_{wire} \left(\frac{3}{2} \frac{r_{wire}}{r_{droplets}} - 1 \right). \tag{5.19}$$

Normalizing further gives

$$\frac{\triangle E}{L\, \sigma\, r_{wire}} = 2\pi \left(\frac{3}{2} \frac{r_{wire}}{r_{droplets}} - 1 \right), \tag{5.20}$$

which is plotted in figure 5.4. The wire fragmentation into isolated droplets is energetically favored if the r.h.s of equation (5.20) is negative and, thus, the system can lower its free energy by fragmentation. This criterion is fulfilled for a ratio $r_{droplets}/r_{wire} > r_c/r_{wire}$. The critical droplet radius r_c is here given by the energetic equivalence of the initial and final state

$$\triangle E = 0 \qquad \Longrightarrow \qquad r_c = \frac{3}{2} r_{wire}. \tag{5.21}$$

The smallest droplets, which can be formed by fragmentation have a diameter 1.5 times larger than the diameter of the nanowire. Their spacing is a priori equal and the distance $\triangle d$ between them is equal to their diameter

$$\triangle d = \frac{2}{n}(L - 2 n_{droplets} r_c) = 3 r_{wire} = 2 r_c. \tag{5.22}$$

This prediction can also be supported by KLMC simulations. As an example a fragmentation of a nanowire is shown in figure 5.5. The wire forms during annealing from an initially cylindrical Gaussian profile of impurity atoms as described in chapter 4.3. Nevertheless, under further annealing the wire is disrupted due to thermal fluctuations. Additionally, being aligned to the [100] direction the simulated wire

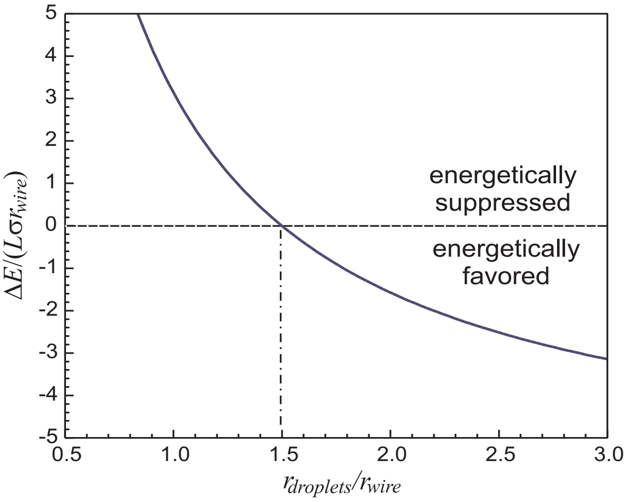

Figure 5.4: Nanowire fragmentation according equation (5.20). The fragmentation is energetically favored for negative values of $\triangle E$. The y-axis is the normalized internal energy difference between the chain of droplets and a continuous wire and the x-axis represents the droplet radius relative to the wire radius $r_{droplets}/r_{wire}$.

has (100) surfaces, which have a higher surface energy than (111) surfaces. The evolution of energetically favored (111) facets on the wire surface may act as a knife and directly lead to the fragmentation of the wire into droplets. As obtainable from figure 5.5, the diameter of the clusters is 1.6 times larger than the wire diameter and the spacing between the clusters is roughly equal to their size, which directly corresponds to the prediction of a cluster system with equal energy.
Although experimental evidence for the fragmentation is still missing, this could be a realistic way to synthesize chains of nanoclusters with roughly equal size and spacing. These linear chains of nanoparticles may provide extremely interesting possibilities in the range of micro-optical applications. Electromagnetic energy can be transported below the diffraction limit by the near-field coupling of dipoles or surface plasmon modes which is called plasmonics [QLKA98, BHA00]. However, it is necessary to obtain very small and closely spaced clusters for this purpose. The controlled fragmentation of a continuous nanowire can provide one way for the synthesis.

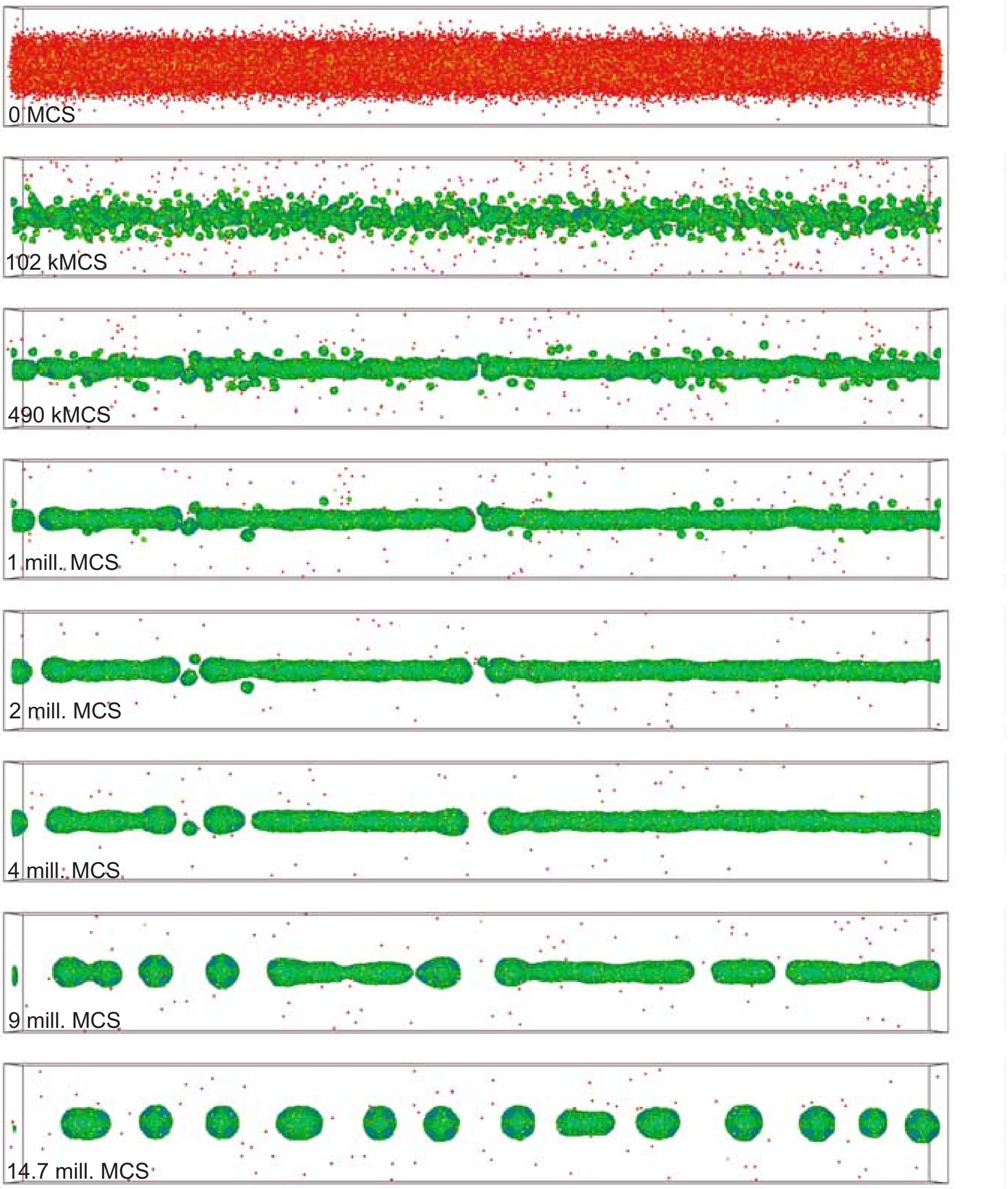

Figure 5.5: Kinetic Monte Carlo simulation of a nanowire formation and fragmentation from an initially cylindrical Gaussian profile with a peak concentration of 31% and a standard deviation of 4 nm. Shown is a sequence of states starting with the initial impurity atom distribution over some intermediate state up to 14.7 million MCS.

Chapter 6

Towards a Controlled Nanowire Growth - Conclusion

6.1 Controlled Nanowire Growth

The last chapters have dealt with the different topics of the IBS of Ge nanowires. The implantation and especially their side affects were subject of chapter 3. As shown, sputtering and redeposition of sputtered atoms has lead to Ge accumulation in the V-groove bottom, which is the initial condition for the subsequent thermal treatment. As pointed out in chapter 4, the dispensed Ge atoms precipitate to nanoclusters, grow in a competitive manner and finally coalesce if the Ge concentration is sufficiently high. KLMC simulations have revealed the critical influence of the broadness of the profile. And finally, the stability of continuous nanowires have been considered in chapter 5.

These topics have lead to suggestions concerning the nanowire growth which are shortly addressed here.

6.1.1 Controlling the Initial Impurity Distribution

The key for the later wire growth is the specific distribution of Ge atoms embedded in the SiO_2 at the V-groove bottom. In order to optimize the nanowire growth one has first to consider this distribution. The point is, to accumulated as much material in the V-groove bottom in a very thin region extended along the V-groove. Additionally, the Ge concentration in the V-grooves sidewalls should be much lower to permit coalescence of nanocluster and, therefore, any connection between the V-groove bottom and the plane wafer. This is essential for an application in electronic devices based on nanowires.

Thus using the knowledge about sputtering and redeposition one can draw the following consequences.

- Choose ions with high sputtering yield. This leads to an increased redeposition of already implanted material into the V-groove bottom and therefore to a higher impurity accumulation at the bottom. Heavy elements might be better than lighter ones.

- Choose a low ion energy. This is somewhat contradictory to the first point but essential. The higher the ion energy the higher is also the ion straggling in target material. The implanted profile gets broader than for low energies. But a very narrow impurity distribution is important for the coalescence of a thin continuous wire during the annealing. Thus to keep the impurity atoms close together in the host it is necessary to use low ion energies which unfortunately decreases the sputtering yield.

6.1.2 The Influence of Moisture

The usage of chemically reactive ions as Ge or Si for the nanowire synthesis provides a major shortcoming. Oxidants could lead to oxidation of the few amount of implanted Ge during the thermal processing. Possible sources of such oxidants in the present synthesis have been listed in chapter 2. Due to the many sources it is not easily excluded them from the sample preparation.

Especially it is not sufficient to reduce the content moisture in the annealing atmosphere as possible be annealing in vacuum. Moisture present in the room air affects already the sample surface right after the implantation. The incorporated hydrogen has been detected by NRA analysis in the SiO_2 [SG00] damaged by the ion irradiation.

Consequently, only a continuous sample handling under vacuum conditions (cluster tool) between the steps of ion implantation and annealing could guarantee an oxidation free synthesis of the Ge nanowires. Moreover, these conditions would allow to choose a much lower ion fluence.

On the other hand, Ge oxidation could be helpful to some extent since only Ge close to the SiO_2 surface is affected. In the present study the nanowire is embedded deeper in the SiO_2 of the V-groove bottom than the Ge in the V-groove sidewalls. Hence, Ge is oxidized first at the V-groove sidewalls which suppresses Ge precipitation there, see figure 2.6(a). This could lead to a better isolation of the nanowire from the plane wafer surface and therefore could be advantageous for electronic devices.

6.1.3 Controlled Ripening and Coalescence

Starting with the initial distribution of Ge atoms dispensed in the SiO_2 at the V-groove bottom an intelligent choice of annealing conditions is fruitful. There are indications for a further growth control beyond the scope of the here given unsystematic KLMC simulations. A temperature variation during the phase separation can lead to a more uniform coalescence as demonstrated for the growth of quantum dots arrays from focused ion beam implanted spots [Str99, chapter 6], [ZBD+99].

The critical stage is the competitive growth (OSTWALD-ripening) of neighboring clusters after nucleation and initial growth. One way out is to choose a very high temperature in the very beginning of the annealing which permits nucleation on the outskirts of the Ge profile. This happens raises the nucleation threshold and Ge nucleates only in the wire center at the point of the highest Ge concentration. Competitive growth is diminished and solved Ge will then condense onto the few precipitates in the center of the later wire, which then coalesce to a continuous wire. Unfortunately the wire will loose quickly Ge by diffusion into the surrounding matrix at that temperatures. Hence, it is necessary to reduce the temperature after the initial nucleation. Moreover, high thermal fluctuations could destabilize thin wires in the late stage of the growth, see chapter 5.

In summary, the following rules can enhance the growth of thin nanowires

- Choose a very narrow initial distribution of impurity atoms (Ge).
- Adjust the maximum impurity concentration above the percolation threshold. It is expected to lay in the range of 30 atomic percent for a standard constant-temperature anneal[1].
- Use a time-depending annealing procedure. Start with high temperatures to guide the nucleation and then lower it in later times.
- Implant directly into a single crystalline matrix, e.g. silicon, to synthesize single crystalline nanowires during subsequent annealing. They will be more stable against fragmentation since internal grain boundaries are missing.

On the other hand, for certain applications a set of well separated droplets is more favorable than a continuous wire. Especially, plasmonics [BHA00] would benefit from such nanocluster chains. As shown in chapter 5 they can be achieved by a controlled disintegration of a continuous nanowire under subsequent ion irradiation. The wire becomes instable against thermal fluctuations under ion irradiation and is fragmented. Further simulations as well as experimental studies concerning the wire disintegration under ion irradiation are certainly needed.

6.2 Conclusion

The formation of Ge nanowires by ion beam synthesis has been studied experimentally as well as theoretically. Ge were implanted into oxidized Si V-grooves formed by anisotropic etching and subsequent oxidation of their surface.

A novel model of surface topology evolution has been developed to study the Ge redistribution in the V-groove during ion irradiation. In a continuum framework the sputtering and redeposition of sputtered Ge is described analytically by means of an integro-differential equation. The contribution of sputtering has been calibrated by experimental measurements of the SiO_2 sputtering yield for Ge^+ irradiation at 70 keV. As a result, the surface shape change of the V-groove was predicted by the numerical solution for the experimentally used condition. It reveals a strong accumulation of Ge in the V-groove bottom caused by sputtering and redeposition which agrees nicely with XTEM images.

The proven Ge enrichment in the V-groove bottom has been the preliminary condition for the subsequent growth of the nanowire during thermal processing. XTEM images of annealed samples have revealed thereby the precipitation and coalescence of dispensed Ge to a nanowire embedded in the SiO_2 at the V-groove bottom. A wire diameter of 35 nm has been found.

---

[1] Be aware that this is only a static description of percolation. A wire may be formed even if the initial Ge concentration has been below the percolation threshold.

Complementary, the growth were studied by means of kinetic 3D lattice Monte Carlo simulations which were used to first estimate a lower boundary of the wire diameter (5..10 nm). Additionally, simulations revealed the metastability of nanowires against a disintegration motivated by thermal fluctuations. As expected, especially thin wires are instable during thermal treatment which was also confirmed by analytical considerations. The discussion of the wire stability has further revealed a lower limit for the diameter of the resulting droplets which agree nicely with Monte Carlo simulations.

Thus, the joint treatment using experimental as well as theoretical tools have led to fruitful insights into the complex phenomena during the nanowire growth in oxidized Si V-grooves. It is my belief that the general usage of pre-structured samples together with an ingenious annealing regime partially under ion irradiation offers rich possibilities for ion beam synthesis of versatile nanostructures.

Appendix A

Mathematical Details of the Surface Evolution Model

A.1 Projection of the Emission Distribution

The angular distribution $f(\theta, \phi)$ of sputtered atoms ejected from the bombarded target surface is essential for a correct description of the redeposition in the surface evolution model presented in in chapter 3.2.2. This angular distribution is given as a two-dimensional function defined in spherical coordinates specifying the probability density for sputtering one atom into the solid angle $d\Omega = \sin\theta \, d\theta \, d\phi$.

$$f(\theta, \phi) = \frac{n+1}{2\pi} \cos^n \theta \tag{A.1}$$

$$1 = \int_0^{2\pi} d\phi \int_0^{\pi/2} d\theta \, \sin\theta \, f(\theta, \phi) \qquad \text{Normalization} \tag{A.2}$$

Nevertheless, an one-dimensional distribution function $f_{2D}(\theta_{2D})$ is needed for the description in an one-dimensional model. Here, $f_{2D}(\theta_{2D})$ denotes the probability density for the emission of one atom into a angular element $d\theta_{2D}$.

This section will provide a link between both distributions functions. In general, the one-dimensional distribution $f_{2D}(\theta_{2D})$ is given by the projection of the two dimensional function $f(\theta, \phi)$ onto the xh-plane, since the y-coordinate of the deposition point is unimportant in the V-groove geometry. As long as the height relative to the V-groove bottom is maintained it doesn't matter where the atoms are deposited along the groove.

This projection can not be carried out in spherical coordinates, thus a new coordinate system, the reduced euler coordinates, are introduced. The relation between both systems is shown in figure A.1. To describe a direction in the new system the z-axis is turned towards the x-axis for an angle θ_{2D}. Further, the obtained axis is turned sidewards counterclockwise towards the y-axis for α. The transformation rules between spherical coordinates and the new coordinates are given by

$$\cos\theta = \cos\alpha \, \cos\theta_{2D} \tag{A.3}$$

$$\sin\theta \, \cos\phi = \sin\theta_{2D} \, \cos\alpha, . \tag{A.4}$$

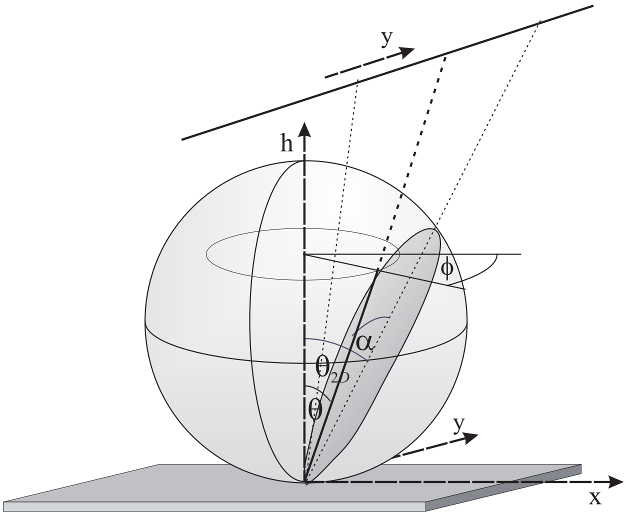

Figure A.1: Relation between spherical coordinates and angles used for projection

which are simplified by introducing new variables ξ, ζ and η

$$\cos\theta = \xi \qquad \cos\theta_{2D} = \zeta \qquad \cos\alpha = \eta \tag{A.5}$$

$$\sin\theta = \sqrt{1-\xi^2} \qquad \sin\theta_{2D} = \sqrt{1-\zeta^2} \qquad \sin\alpha = \sqrt{1-\eta^2} \tag{A.6}$$

$$-\sin\theta\, d\theta = d\xi \qquad -\sin\theta_{2D}\, d\theta = d\zeta \qquad -\sin\alpha\, d\alpha = d\eta \tag{A.7}$$

The transformation equations (A.3) and (A.4) reads then as

$$\xi = \zeta\,\eta \qquad \phi = \arccos\left(\eta\sqrt{\frac{1-\zeta^2}{1-\zeta^2\eta^2}}\right). \tag{A.8}$$

Similarly, the normalization integral in equation (A.2) can be rewritten as

$$1 = \int\limits_{-\pi/2}^{\pi/2} \underbrace{\int\limits_{-\pi/2}^{\pi/2} f(\theta,\alpha)\left|\frac{\partial\,\theta\,\phi}{\partial\,\theta_{2D}\,\alpha}\right| d\alpha}_{f_{2D}(\theta_{2D})}\, d\theta_{2D} = 4\int\limits_0^1\int\limits_0^1 f(\zeta,\eta)\left|\frac{\partial\,\xi\,\phi}{\partial\,\zeta\,\eta}\right| d\zeta\, d\eta. \tag{A.9}$$

The functional determinant is here given by

$$\left|\frac{\partial\,\xi\,\phi}{\partial\,\zeta\,\eta}\right| = \begin{vmatrix} \frac{\partial\xi}{\partial\zeta} & \frac{\partial\xi}{\partial\eta} \\ \frac{\partial\phi}{\partial\zeta} & \frac{\partial\phi}{\partial\eta} \end{vmatrix} = -\frac{\eta}{\sqrt{1-\eta^2}\sqrt{1-\zeta^2}}. \tag{A.10}$$

Carrying out the η-integration in equation (A.9) gives

$$1 = -\frac{4}{\pi} \int_0^1 \int_0^1 f(\zeta, \eta) \, \frac{\eta}{\sqrt{1-\eta^2}\sqrt{1-\zeta^2}} \, d\zeta \, d\eta \tag{A.11}$$

$$= -4 \frac{n+1}{2\pi} \int_0^1 \int_0^1 (\zeta\eta)^n \, \frac{\eta}{\sqrt{1-\eta^2}\sqrt{1-\zeta^2}} \, d\zeta \, d\eta \tag{A.12}$$

$$= -2 \int_0^1 \frac{n+1}{2\pi} \, B\left(\frac{1}{2}, \frac{n+1}{2}\right) \frac{\zeta^n}{2\sqrt{1-\zeta^2}} \, d\zeta, \tag{A.13}$$

with the Beta function $B(c,d) = \Gamma(c)\Gamma(d)/\Gamma(c+d)$. Then, the re-substitution of ζ by θ_{2D} in equation (A.13) gives the one dimensional angular distribution function $f_{2D}(\theta_{2D})$

$$1 = -2 \frac{n+1}{2\pi} \, B\left(\frac{1}{2}, \frac{n+1}{2}\right) \int_0^{\pi/2} \frac{\cos^n \theta_{2D}}{\sin \theta_{2D}} \, d(\cos \theta_{2D}) \tag{A.14}$$

$$= \frac{n+1}{2\pi} \, B\left(\frac{1}{2}, \frac{n+1}{2}\right) \int_{-\pi/2}^{\pi/2} \cos^n \theta_{2D} \, d\theta_{2D} \tag{A.15}$$

$$= \int_{-\pi/2}^{\pi/2} f(\theta_{2D}) \, d\theta_{2D}. \tag{A.16}$$

In summary, the in chapter 3.2.2 used one-dimensional angular distribution function $f_{2D}(\theta_{2D})$ of sputtered atoms is given as the projection of the two-dimensional distribution $f(\theta, \phi)$ onto the xh-plane.

$$f_{2D}(\theta_{2D}) = \frac{n+1}{2\pi} \, B\left(\frac{1}{2}, \frac{n+1}{2}\right) \cos^n \theta. \tag{A.17}$$

As special cases the projection are explicitly given for $n = 1, 2$.

$$n = 1: \qquad f(\theta, \phi) = \frac{1}{\pi} \cos \theta \qquad \Longrightarrow \qquad f_{2D}(\theta_{2D}) = \frac{1}{2} \cos \theta_{2D} \tag{A.18}$$

$$n = 2: \qquad f(\theta, \phi) = \frac{3}{2\pi} \cos^2 \theta \qquad \Longrightarrow \qquad f_{2D}(\theta_{2D}) = \frac{2}{\pi} \cos^2 \theta_{2D}. \tag{A.19}$$

A.2 Stability of the Numerical Solution

Due to the nonlinearity the surface evolution model developed in chapter 3 can only be solved numerically. The partial differential equation (3.25) or (3.27) governing the surface evolution in time without redeposition has been transformed into the corresponding difference equation. Derivatives were approximated by differences

$$\frac{\partial h(x,t)}{\partial t} \approx \frac{h(x,t+\triangle t) - h(x,t)}{\triangle t} \tag{A.20}$$

$$\frac{\partial h(x,t)}{\partial x} \approx \frac{h(x+\triangle x,t) - h(x-\triangle x,t)}{2\triangle x}. \tag{A.21}$$

This allows the introduction of an discrete grid in the time and space domain with the incremental step size $\triangle t$ and $\triangle x$, respectively. On this grid, the evolution equation relates the surface at time t to $t + \triangle t$ and, thus, allows the iterative computation of the surface evolution in time.

The important question is, which step size is sufficient to solve the equation with an acceptable error in minimal time. Moreover, under which assumptions is the stability of the numerical algorithm assured.

Sigmund's formulation of the sputtering yield $Y(\varphi)$ from equation (3.2) will be used for the discussion of the stability. The corresponding evolution equation is then equation (3.25) or

$$\frac{\rho}{\Phi}\frac{\partial h(x,t)}{\partial t} = \sqrt{1+\left(\frac{\partial h}{\partial x}\right)^2} - Y_0\left(1+\left(\frac{\partial h}{\partial x}\right)^2\right)^{\frac{n+1}{2}}. \tag{A.22}$$

For the sake of simplicity the first term describing the swelling will be neglected and the parameter n in the second term was set to one. This simplifies equation (A.22) to

$$\frac{\partial h(x,t)}{\partial t} = -\lambda\left(1+\left(\frac{\partial h}{\partial x}\right)^2\right) \qquad \text{with} \qquad \lambda = \frac{\Phi}{\rho}Y_0, \tag{A.23}$$

which is the most simplified form for the surface evolution equation and contains the nonlinear KPZ term [KPZ86], see chapter 3.4. Consecutively, the equation (A.23) is transformed into a difference equation. However, a relation for the overall stability of such a difference equation can not be given due to the highly nonlinear character. Nevertheless, at least point wise stability is discussed, which is a necessary condition for the complete stability of the numerical algorithm. Therefore, the first derivative of equation (A.23) is considered

$$\frac{\partial^2 h(x,t)}{\partial x\,\partial t} = -2\lambda\left(\frac{\partial h}{\partial x}\right)\left(\frac{\partial^2 h}{\partial x^2}\right). \tag{A.24}$$

This relates the time evolution of the surface gradient to the gradient itself and the local curvature of the surface. Substituting the gradient $\partial h/\partial x = u$ gives

$$\frac{\partial u}{\partial t} + 2\lambda u\underbrace{\left(\frac{\partial u}{\partial x}\right)}_{\text{const.}} = 0 = \frac{\partial u}{\partial t} + f(u,t), \tag{A.25}$$

whereas the derivative $\frac{\partial u}{\partial x}$ is treated as a constant parameter. Hence, equation (A.25) has become an ordinary differential equation, whose stability under numerical

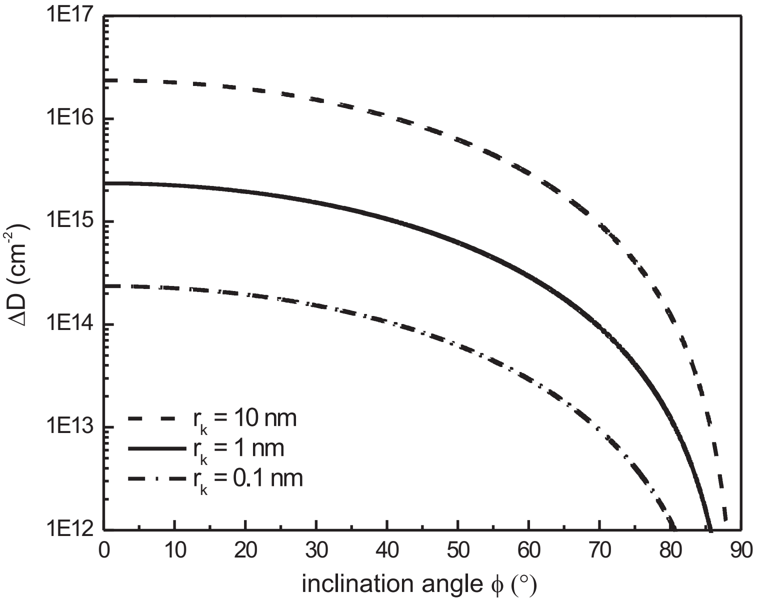

Figure A.2: Upper bound for the incremental fluence, which is the product of the incremental time step and the flux density. The numerical algorithm is only stable if the value of the incremental fluence is less than the depicted value, which was obtained for the numerical solution of the evolution of a SiO_2 ($\rho = 6.6 \times 10^{22}$ g cm^{-3}) surface under 70 keV Ge^+ irradiation ($Y_0 = 2.8$). The stability also depends on the local radius of curvature. As an example three different values ($r_k = 0.1$, 1, 10 nm) were chosen.

solution can be judged. An incremental time step should obey the following relation according ref. [Pot73, chapt. 2.6]

$$\triangle t \leq \frac{2}{\left.\frac{\partial f}{\partial u}\right|_u} = \left(\lambda \frac{\partial u}{\partial x}\right)^{-1} = \frac{\rho}{Y_0\,\Phi}\left(\frac{\partial^2 h}{\partial x^2}\right)^{-1}. \tag{A.26}$$

Using the local radius of curvature r_k this equation is slightly rewritten to

$$r_k = \frac{(1+u^2)^{3/2}}{\frac{\partial u}{\partial x}} \qquad \Longrightarrow \qquad \triangle t \leq \frac{r_k\,\rho}{Y_0\,\Phi}\left(1+\left(\frac{\partial h}{\partial x}\right)^2\right)^{-3/2}. \tag{A.27}$$

Further, the gradient $\partial h/\partial x$ is expressed by the inclination angle φ according equation (3.23)

$$\frac{1}{\cos\varphi} = \sqrt{1+\left(\frac{\partial h}{\partial x}\right)}. \tag{A.28}$$

The ion flux density Φ can be combined with the incremental time step $\triangle t$ to an incremental fluence $\triangle D$. Here the fluence acts as a time-variable and releases the unknown flux density from the equation.

$$\triangle D \leq \Phi\,\triangle t \leq \frac{r_k\,\rho}{Y_0}\cos^3\varphi \tag{A.29}$$

The numerical solution of the evolution equation (A.23) is only stable, if the product of the flux density Φ and the incremental time step $\triangle t$ is less than the right hand side of equation (A.29). The value is depicted in figure A.2, whereas the material parameters have been chosen according the V-groove example in chapter 3.3. The stability of the numerical solution depends on the local radius of curvature r_k and the inclination angle of the surface φ. The algorithm becomes unstable for small radii of curvature and large inclination angles. Moreover, this stability condition must be fulfilled for each point on the lateral axis and it represents only a necessary condition, not a sufficient one, for the final stability of the numerical algorithm.

This effectively limits the range of applicability of the numerical algorithm. In the case of the V-groove the highest inclination angle is 54.7 ° and at least in the V-groove bottom the local radius of curvature is in the order of less than a nanometer. Further, if one intends to have a stable model up to 70 ° the incremental fluence has to be less than $\triangle D = 1 \times 10^{12}$ cm^{-2}. This gives a total number of 1×10^5 iterative steps to calculate for one point on the lateral x-axis. Assuming a lateral grid of roughly 1000 points this leads to 1×10^8 steps to compute, which is almost at the limit of modern personal computers.

This is also the reason, why the initial surface of the V-groove has been simplified. The as-oxidized SiO_2 surface shows a sharp depression at the V-groove bottom with inclination angles higher than 60 degree. Having used this profile would directly lead to an unstable numerical algorithm and a wrong solution.

List of Figures

Bibliography

[Avo93] P. Avouris, editor. *Atomic and Nanometer-Scale Modification of Materials: Fundamentals and Applications.* Kluwer, Dordrecht, 1993.

[Beh81] R. Behrisch, editor. *Sputtering by Particle Bombardment*, volume I, II. Springer-Verlag, Heidelberg, 1981.

[BH80] J. P. Biersack and L. G. Haggmark. A monte carlo program for the transport of energetic ions in amorphous targets. *Nuclear Instruments and Methods in Physics Research B*, 174:257–269, 1980.

[BH88] R. M. Bradley and J. M. E. Harper. Theory of ripple topography induced by ion bombardment. *Journal of vacuum science and technology A*, 6(4):2390, 1988.

[BH92] K. Binder and D. W. Heerman. *Monte Carlo Simulation in Statistical Physics*, volume 80 of *Springer Series in Solid-State Sciences.* Springer-Verlag, Berlin Heidelberg, 2 edition, 1992.

[BHA00] M. L. Brongersma, J. W. Hartman, and H. A. Atwater. Electromagnetic energy transfer and switching in nanoparticle chain-arrays below the diffration limit. *Submitted to Physical Review Letters*, 2000.

[BHR97] V. A. Borodin, K. H. Heinig, and S. Reiß. Self-organization kinetics in finite precipitate ensembles during coarsening. *Physical Review B*, 56(9), September 1997.

[BHSO00] V. A. Borodin, K. H. Heinig, B. Schmidt, and S. Oswald. Oxidation of Ge implanted into SiO_2 layers: modeling and XPS. *to be published in Nuclear Instruments and Methods in Physics Research B*, 2000. presented at E-MRS 2000, Strasbourg, Symposium R.

[BKT98] A. Benyagoub, S. Klaumünzer, and M. Toulemonde. Radiation-induced compaction and plastic flow of vitreous silica. *Nuclear Intstruments and Methods in Physics Research B*, 146:449–454, 1998.

[BML97] A.-L. Barabási, M. A. Makeev, and C. S. Lee. Roughening of ion-eroded surfaces. *pre-print condensed matter arXiv:cond-mat*, 9703243, 27 March 1997.

[BRGK97] G. Biasiol, F. Reinhardt, A. Gustafsson, and E. Kapon. Self-limiting growth of GaAs surfaces on nonplanar substrates. *Applied Physics Letters*, 71(13):1831–1833, September 1997.

[BT98] L. Bischoff and J. Teichert. Focused ion beam sputtering of silicon and related materials. Technical Report FZR-217, Forschungszentrum Rossendorf, Institut für Ionenstrahlphysik und Materialforschung, March 1998.

[BW80] J. Belson and I. H. Wilson. Flux density equations for topographical evolution of features on ion bombarded surfaces. *Radiation Effects*, 51:27–34, 1980.

[BW81] J. Belson and I. H. Wilson. Theory of redeposition of sputtered flux on to surface asperities. *Nuclear Intstruments and Methods*, 182/183:275–281, 1981.

[COMR$^+$00] Y. Chen, D. A. A. Ohlberg, G. Medeiros-Ribeiro, Y. A. Chang, and R. S. Williams. Self-assembled growth of epitaxial erbium disilicide nanowires on silicon (001). *Applied Physics Letters*, 76(26):4004–4006, 2000.

[CTO96] T. K. Chini, M. Tanemura, and F. Okuyama. Angular distribution of sputtered Ge atoms by low keV Ar^+ and Ne^+ ion bombardment. *Nuclear Intstruments and Methods in Physics Research B*, 119:387–391, 1996.

[CV96] G. Carter and V. Vishnyakov. Roughening and ripple instabilities on ion-bombarded Si. *Physical Review B*, 54(24):17647–17653, 1996.

[Dav98] J. H. Davies. *The Physics of Low-Dimensional Semiconductors*. Cambridge University Press, 1998.

[DS99] R. Ditchfield and E. G. Seebauer. Direct measurement of ion-induced surface diffusion. *Physical Review Letters*, 82(6):1185–1188, February 1999.

[EBR91] E. A. Eklund, R. Bruinsma, and J. Rudnick. Submicron-scale surface roughening induced by ion bombardment. *Physical Review Letters*, 67:1759–1762, 1991.

[Eck91] W. Eckstein. *Computer Simulation of Ion-Solid Interactions*. Springer-Verlag, Heidelberg, 1991.

[EGRRO93] W. Eckstein, C. Garcia-Rosales, J. Roth, and W. Ottenberger. Sputtering data. IPP-Report 9/82, Max-Planck-Institut für Plasmaphysik, February 1993.

[EM99] W. Eckstein and T. Müller. Simulation of the angular distribution of sputtered atoms from an inclined SiO_2 target. private communication, 1999.

[Fey60] R. P. Feynman. *Engineering and Science.* 1960. page 22.

[GDC$^+$00] Q. Gu, H. Dang, J. Cao, J. Zhao, and S. Fan. Silicon nanowires grown on iron-patterned silicon substrates. *Applied Physics Letters*, 76(21):3020–3021, 2000.

[GR81] F. C. Goodrich and A. I. Rusanov, editors. *The Modern Theory of Capillarity.* Akademie-Verlag, Berlin, 1981.

[GRBK95] A. Gustafsson, F. Reinhardt, G. Biasiol, and E. Kapon. Low-pressure organometallic chemical vapor deposition of quantum wires on v-grooved substrates. *Applied Physics Letters*, 67(25):3673–3675, 1995.

[GSRW00] J. L. Gole, J. D. Stout, W. L. Rauch, and Z. L. Wang. Direct synthesis of silicon nanowires, silica nanospheres, and wire-like nanosphere agglomerates. *Applied Physics Letters*, 76(17):2346–2348, 2000.

[HDL$^+$95] A. Hartmann, C. Dieker, R. Loo, L. Vescan, H. Lüth, and U. Bangert. Photoluminescence and microstructure of self-ordered grown SiGe/Si quantum wires. *Applied Physics Letters*, 67(13):1888–1890, September 1995.

[Hei95] K.-H. Heinig. unpublished, 1995.

[Hei00] K.-H. Heinig. Inverse ostwald ripening. *to be published in Nuclear Instruments and Methods in Physics Research*, 2000. presented at EMRS 2000, Strasbourg, Symposium R.

[HSM$^+$99] K.-H. Heinig, B. Schmidt, A. Markwitz, R. Grötzschel, M. Strobel, and S. Oswald. Precipitation, ripening and chemical effects during annealing of Ge^+ implanted SiO_2 layers. *Nuclear Instruments and Methods in Physics Research B*, 148:969–974, 1999.

[HVDL95] A. Hartmann, L. Vescan, C. Dieker, and H. Lüth. Growth of SiGe quantum wires and dots on patterned si substrates. *Journal of Applied Physics*, 77(5):1959–1963, March 1995.

[HZO$^+$87] J. Heath, Q. Zhang, S. O'Brien, R. Curl, H. Kroto, and R. Smalley. The formation of long carbon chain molecules during laser vaporization of graphite. *Journal of the American Chemical Society*, 109:359, 1987.

[IK97] A. L. Itkin and E. G. Kolesnichenko. *Microscopic Theory of Condensation in Gases and Plasma.* Series on Advances in Mathematics for Applied Sciences - Vol. 44. World Scientific, 1997.

[ISF98] Y. Ishikawa, N. Shibata, and S. Fukatsu. Creation of [110]-aligned si quantum wires encompassed by SiO_2 using low-energy separation-by-implanted-oxygen on a v-groove patterned substrate. *Applied Physics Letters*, 72(20):2592–2594, 1998.

[ISF99] Y. Ishikawa, N. Shibata, and S. Fukatsu. Fabrication of [110]-aligned si quantum wires embedded in SiO_2 by low-energy oxygen implantation. *Nuclear Instruments and Methods in Physics Research B*, 147:304–309, 1999.

[KBA99] J. Kedzierski, J. Bokor, and E. Anderson. Novel method for silicon quantum wire transistor fabrication. *Journal of vacuum science and technology B - Microelectronics and Nanometer Structures*, 17(6):3244–3247, November 1999.

[KBR89] R. P. U. Karunasiri, R. Briunsma, and J. Rudnick. Thin-film growth and the shadow instability. *Physical Review Letters*, 62(7):788–791, 1989.

[KEDR98] M. Küstner, W. Eckstein, V. Dose, and J. Roth. The influence of surface roughness on the angular dependence of the sputter yield. *Nuclear Intstruments and Methods in Physics Research B*, 145:320–331, 1998.

[KLK$^+$97] E. K. Kim, M.-S. Lee, S.-I. Kim, Y. J. Park, S.-K. Min, and J. Y. Lee. InGaAs layer effect on the growth of AlGaAs/GaAs quantum wires on v-grooved GaAs substrates. *Applied Surface Sience*, 117/118:690–694, 1997.

[KP73] E. F. Krimmel and H. Pfleiderer. Implantation profiles modified by sputtering. *Radiation Effects*, 19:23, 1973.

[KPZ86] M. Kardar, G. Parisi, and Y.-C. Zhang. Dynamic scaling of growing interfaces. *Physical Review Letters*, 56:889–892, 1986.

[KT76] Y. Kuramoto and T. Tsuzuki. Persistent propagation of concentration waves in dissipative media far from thermal equilibrium. *Progress in Theoretical Physics*, 55(2):356–369, February 1976.

[LL79] L. D. Landau and E. M. Lifschitz. *Statistische Physik*, volume 5 of *Lehrbuch der theoretischen Physik*. Akademie-Verlag, Berlin, 5 edition, 1979.

[LS61] I. M. Lifschitz and V. V. Slyozov. The kinetics of precipitation from supersaturated solid solutions. *Journal of the Physical Chemistry of Solid*, 19:35, 1961.

[LSW$^+$95] J. L. Liu, Y. Shi, F. Wang, R. Zhang, P. Han, B. H. Mao, and Y. D. Zheng. Fabrication of silicon quantum wires by anisotropic wet chemical etching and thermal oxidation. *Journal of vacuum science and technology B - Microelectronics and Nanometer Structures*, 13(5):2137–2138, 1995.

[Mal94] J. B. Malherbe. Sputtering of compound semiconductor surfaces. I. ion-solid interactions and sputtering yields. *Critical Reviews in Solid State and Materials Sciences*, 19(2):55–127, 1994.

[MB97] M. A. Makeev and A.-L. Barabási. Ion-induced effective surface diffusion in ion sputtering. *Applied Physics Letters*, 71(19):2800–2802, November 1997.

[MCB00] M. Makeev, R. Cuerno, and A.-L. Barabási. Morphology of ion-sputtered surfaces. *to be published*, 2000.

[MCH94] T. M. Mayer, E. Chason, and A. J. Howard. Roughening instability and ion-induced viscous relaxation of SiO_2 surfaces. *Journal of Applied Physics*, 76(3):1633–1643, 1994.

[MHS00] T. Müller, K.-H. Heinig, and B. Schmidt. Shape evolution of oxidized silicon V-grooves during high dose ion implantation. *accepted for publication in Nuclear Instruments and Methods in Physics Research B*, 2000. presented at the EMRS conference 2000, Strasbourg, Symposium R.

[MRR+53] N. Metropolis, A. Rosenbluth, M. Rosenbluth, A. Teller, and E. Teller. Equation of state calculations by fast computing machines. *Journal of Chemical Physics*, 21(6):1087–1092, June 1953.

[NB99] M. Newman and G. T. Barkema. *Monte Carlo Methods in Statistical Physics.* Oxford University Press, Oxford New York, 1999.

[NMH96] M. Nastasi, J. W. Mayer, and J. K. Hirvonen. *Ion-Solid Interactions: Fundamentals and Applications.* Cambrige Solid State Series. Cambridge University Press, 1996.

[NNK+95] H. Namatsu, M. Nagase, K. Kurihara, K. Iwadate, T. Furuta, and K. Murase. Fabrication of sub-10-nm silicon lines with minimum fluctuation. *Journal of vacuum science and technology B - Microelectronics and Nanometer Structures*, 13(4):1473–1476, 1995.

[NRZN00] T. Nuver, H. Rudolph, P. Zeijlmans van Emmichoven, and A. Niehaus. Preferential ejection of high-energy sputtered Cu atoms in keV atom - Cu(110) collisions. *Nuclear Intstruments and Methods in Physics Research B*, 164-165:785–794, 2000.

[OSH00] S. Oswald, B. Schmidt, and K.-H. Heinig. XPS investigation with factor analysis for the study of Ge clustering in SiO_2. *Surface and Interface Analysis*, 29:249–254, 2000.

[Ost97] W. Ostwald. Studien über die Bildung und Umwandlung fester Körper. *Zeitschrift für Physikalische Chemie*, 22:289, 1897.

[PB99] M. Plischke and B. Bergersen. *Equilibrium Statistical Physics.* World Scientific, Singapore, 2 edition, 1999.

[Pot73] D. Potter. *Computational Physics.* John Wiley & Sons, 1973.

[QLKA98] M. Quinten, A. Leitner, J. R. Krenn, and F. R. Aussenegg. Electromagnetic energy transport via linear chains of silver nanoparticles. *Optical Letters*, 23(17):1331–1333, 1998.

[Rei96] S. Reiß. *Theorie und Computersimulation der Ostwald-Reifung bei der Ionenstrahlsynthese*. PhD thesis, Technische Universität Dresden, Forschungszentrum Rossendorf, August 1996.

[RG91] C. Roland and H. Guo. Interface growth with a shadow instability. *Physical Review Letters*, 66(16):2104–2107, 1991.

[RH96] S. Reiß and K.-H. Heinig. Self-structuring of buried SiO_2 precipitates layers during ibs: A computer simulation. *Nuclear Instruments and Methods in Physics Research B*, 112:223–227, 1996.

[RK95] M. Rost and J. Krug. Anisotropic Kuramoto-Sivashinsky equation for surface growth and erosion. *Physical Review Letters*, 75(21):3894–3897, November 1995.

[RSD$^+$00] B. Rout, B. Sundaravel, A. K. Das, S. K. Ghose, K. Sekar, D. P. Mahapatra, and B. N. Dev. Self-assembled gold silicide wires on bromide-passivated si(110) surfaces. *Journal of vacuum science and technology B - Microelectronics and Nanometer Structures*, 18(4):1847–1852, 2000.

[SBW$^+$99] T. Schrimpf, P. Bönsch, D. Wüllner, H.-H. Wehmann, A. Schlachetzki, F. Bertram, T. Riemann, and J. Christen. InGaAs quantum wires and wells on v-groove InP substrates. *Journal of Applied Physics*, 86(9):5207–5214, November 1999.

[SG00] B. Schmidt and R. Grötzschel. Hydrogen excess in as-implanted SiO_2 layers after handling at room atmosphere. private comunications, August 2000.

[SHM98] M. Strobel, K. H. Heinig, and W. Möller. A combination of atomic and continuum models describing the evolution of nanoclusters. *Computational Materials Science*, 10:457–462, 1998.

[Shu00] V. I. Shulga. Angular distribution of atoms sputtered from amorphous and polycrystalline targets. *Nuclear Intstruments and Methods in Physics Research B*, 164-165:733–747, 2000.

[Sig69] P. Sigmund. Theory of sputtering. I. Sputtering yield of amorphous and polycrystalline targets. *Physical Review*, 184(2):383–416, August 1969.

[Str99] M. Strobel. *Modeling and Computer Simulation of Ion Beam Synthesis of Nanostructures*. PhD thesis, Technische Universität Dresden, Forschungszentrum Rossendorf, November 1999. Wissenschaftlich-Technische Berichte FZR-277.

[THS$^+$98] M. Terrones, W. K. Hsu, A. Schilder, H. Terrones, N. Grobert, J. P. Hare, Y. Q. Zhu, M. Schwoerer, K. Prassides, H. W. Kroto, and D. R. M. Walton. Novel nanotubes and encapsulated nanowires. *Applied Physics A: Materials Science & Processing*, 66:307–317, 1998.

[TKH$^+$98] N. Toyoda, H. Kitani, N. Hagiwara, T. Aoki, J. Matsuo, and I. Yamada. Angular distribution of the particles sputtered with ar cluster ions. *Materials Cemistry and Physics*, 54:262–265, 1998.

[TNA$^+$98] D. Tsouklalas, P. Normand, C. Aidinis, E. Kapetanakis, and P. Argitis. Fabrication of si nanodevices by optical lithography and anisotropic etching. *Microelectronic Engineering*, 41/42:523–526, 1998.

[TT95] H. Trinkaus and A. I. Tyazanov. Viscoelastic model for the plastic flow of amorphous solids under energetic ion bombardment. *Physical Review Letters*, 74(25):5072–5075, June 1995.

[TUO99] M. Tanemura, M. Ukita, and F. Okuyama. Angular distribution of particles sputtered from III-V compound semiconductors by Ar^+-ion bombardment. *Surface Science*, 426:141–146, 1999.

[VDC96] J. J. Vajo, R. E. Doty, and E.-H. Cirlin. Influence of O_2^+ energy, flux, and fluence on the formation and growth of sputtering-induced ripple topography on silicon. *Journal of vacuum science and technology A*, 15(5):2709–2721, 1996.

[Wag61] C. Wagner. Theorie zur Alterung von Niederschlägen durch Umlösen. *Zeitschrift für Elektrochemie*, 65:581, 1961.

[WBW$^+$97] C. W. White, J. D. Budai, S. P. Withrow, J. G. Zhu, S. J. Pennycook, R. A. Zuhr, D. M. Hembree Jr, D. O. Henderson, R. H. Magruder, M. J. Yacaman, G. Mondragon, and S. Prawer. Encapsulated nanocrystals and quantum dots formed by ion beam synthesis. *Nuclear Instruments and Methods in Physics Research B*, 127/128:545–552, 1997.

[YII83] Y. Yamamura, Y. Itakawa, and N. Itoh. Sputtering yield. In *IPPJ - AM -26, Nagoya*, chapter 4, pages 59–97. 1983.

[YKF$^+$97] S.-I. Yanagiya, S. Kamimura, M. Fijii, M. Ishida, Y. Moriyasu, M. Matsui, M. Yoshimoto, T. Ohnishi, K. Yoshida, K. Sasaki, and H. Koinuma. Self-formed silicon quantum wires on ultrasmooth sapphire substrates. *Applied Physics Letters*, 71(10):1409–1411, September 1997.

[ZBD$^+$99] R. A. Zuhr, J. D. Budai, P. G. Datskos, A. Meldrum, K. A. Thomas, R. J. Warmack, C. W. White, L. C. Feldmann, M. Strobel, and K.-H. Heinig. Nanostructured arrays formed by finely focused ion beams. *preprint*, 1999.

[ZBL85] J. F. Ziegler, J. P. Biersack, and U. Littmark. *The Stopping and Range of Ions in Solids*. Pergamon Press, New York, 1985. SRIM 98.4 code available at http:/www.research.ibm.com/ionbeams/.

[ZTW$^+$00] Y. F. Zhang, Y. H. Tang, N. Wang, C. S. Lee, I. Bello, and S. T. Lee. Germanium nanowires sheathed with an oxide layer. *Physical Review B*, 61(7):4518–4521, February 2000.

[ZWCW96] W. Zhenxia, L. Wenyun, W. Chuanshan, and W. Wenmin. Modeling of the angular distribution of sputtered particles from roughened elemental and alloy targets. *Vacuum*, 47(12):1465–1472, 1996.

Acknowledgement

I gratefully acknowledge the help of numerous people during the work on my thesis. Especially, I'd like to thank my supervisors from Rossendorf, Karl-Heinz Heinig and Bernd Schmidt, which had the initial idea of the V-groove principle and awakened my interest on the ion beam synthesis of nanostructures. Both encouraged me during many fruitful and critical discussions and allowed me to participate on their rich experience of ion beam synthesis. Due to them, I had the unique chance to study the subject from both sides, experimentally and theoretically.

Moreover, I want to thank Prof. Möller for his steady encouragement, his willingness to referee my thesis and his careful and critical review. He also mediated the contact to Wolfgang Eckstein, who helped me with a valuable Sputter-TRIM simulation. The Institute has further allowed me to attend the annual conference of the European Materials Research Society (E-MRS) in Strasbourg, June 2000, I'd like to thank for. In addition, I have used the implantation and preparation facilities given in Rossendorf and always had a strong support by the technical staff. Their precise and experienced work contributed to a very large amount to the success of the experiments. Even more I've found in Arndt Mücklich a TEM expert, who helped me with many specific topics.

From the view of the computer simulations I have thank Matthias Strobel, who introduced me in his kinetic Monte Carlo code. Due to him I only had to customize the code for my purposes instead of writing it from the scratch.

Before I started my thesis in Rossendorf, I had the chance to spent three months in the lab of Harry Atwater at Caltech. And although the done AFM investigations on buried nanoclusters are not presented here I would like to thank Harry Atwater and Mark Brongersma for the stimulating discussions, since those sharpened my view on the subject. Due to them I decided to write the thesis in English and I've found in Harry Atwater a respected referee.

To all of them and all I've forgotten to list I'd like to say: *Dankeschön*

Ehrenwörtliche Erklärung

Hiermit versichere ich, daß ich die vorliegende Arbeit selbständig ohne Benutzung anderer als der angegebenen Hilfsmittel angefertigt habe. Die aus fremden Quellen direkt oder indirekt übernommenen Gedanken sind als solche kenntlich gemacht. Diese Arbeit wurde bisher weder im Inland noch im Ausland in gleicher oder ähnlicher Form einer Prüfungsbehörde vorgelegt.

Dresden, den 30. 11. 2000